UNIVERSITY OF SOUTHAMPTON

FACULTY OF ENGINEERING, SCIENCE AND MATHEMATICS
School of Engineering Sciences

An Investigation of the Feasibility of a Spacecraft Multifunctional Structure using Commercial Electrochemical Cells

by

Samuel Charles Roberts MEng

Thesis for the degree of Doctor of Philosophy

April 2009

UNIVERSITY OF SOUTHAMPTON

ABSTRACT

FACULTY OF ENGINEERING, SCIENCE & MATHEMATICS

SCHOOL OF ENGINEERING SCIENCES

Doctor of Philosophy

AN INVESTIGATION OF THE FEASIBILITY OF A SPACECRAFT MULTIFUNCTIONAL STRUCTURE USING COMMERCIAL ELECTROCHEMICAL CELLS

by Samuel Charles Roberts

Multifunctional structures offer the potential for large savings in the mass and cost of spacecraft missions. By combining the functions of one or more subsystems with the primary structure, mass is reduced and internal volume freed up for additional payload, or removed to reduce structural mass. Lithium batteries, increasingly preferred to other power storage solutions, can be employed to produce such structures by incorporating prismatic batteries into structural sandwich panels. Such "powerstructures" can reduce the mass and volume of the power storage subsystem.

After reviewing the current work in the field of multifunctional structures, this thesis describes the objective of the research, to examine the usefulness and feasibility of a multifunctional structure based on commercial lithium cells and sandwich structures. The next section presents a study that quantifies the benefits of this technology, showing maximum savings of up to 2% of total mass, and 0.5-1% for common spacecraft designs.

The next section describes experimental investigations into the mechanical suitability of commercial PLI cells for use in the multifunctional structure. Firstly, the effect of launch vibration was considered: 15 and 25 g_{rms} tests showed no measurable loss in electrical performance. Then, the structural attributes of the cells were measured using a dynamic shear test. The shear modulus of the cells was found to be rather lower than that of an aluminium honeycomb core material.

Consideration is then given to the practical implications of a multifunctional structure. The feasibility of manufacturing is assessed through the construction of a trial panel, showing that the cells lose some capacity and suffer an increase in internal resistance in a high-temperature adhesive cure and that a cold-bonding process may thus be preferable. The resultant panel was then vibrated on an electrodynamic shaker to both assess the resilience of the cells and test the reliability of finite element models. These finite element models are then used for a simple optimisation, showing that a well-designed powerstructure can have structural performance comparable to a conventional design.

The final section weighs the benefits of using a multifunctional structure against the potential disadvantages in terms of cost, design time and flexibility, as well as assessing the validity of assumptions made in the work. The conclusion is that a multifunctional structure of this type, whilst not worthwhile for all mission types, could potentially increase the feasibility of short-term spacecraft missions using small satellites (of the order of 100 kg) with large energy storage requirements.

Contents

List of Figures

List of Tables

Nomenclature

Abbreviations and Acronyms

Ag-Zn	silver-zinc
AIV	assembly, integration and verification
BOL	beginning of life
CAD	computer-aided design
CC-CV	constant current, constant voltage
CFRP	carbon fibre reinforced plastic
COTS	commercial off-the-shelf
DARPA	Defence Advanced Research Projects Agency
DOD	depth of discharge
EOL	end of life
ESA	European Space Agency
FE	finite element
FEA	finite element analysis
FIPP	Flexible Integrated Power Pack
FITS	Folded Integrated Thin-film Stiffener
GEO	geosynchronous equatorial orbit
GPS	Global Positioning System
ITNES	ITN Energy Systems, Inc.
JAXA	Japan Aerospace Exploration Agency
LEO	low Earth orbit
$LiCoO_2$	lithium cobalt dioxide
$LiFePO_4$	lithium iron phosphate
$LiNiO_2$	lithium nickel dioxide
LiPB	lithium-ion polymer battery
$LiPF_6$	lithium phosphorous hexafluoride

LiV_2O_5	lithium vanadium pentoxide
LPB	lithium polymer battery
MAV, µAV	micro air vehicle
MFS	multifunctional structure(s)
Na-S	sodium-sulphur
Ni-Cd	nickel-cadmium
Ni-H_2	nickel-hydrogen
Ni-MH	nickel-metal hydride
NRL	Naval Research Laboratory
OCV	open circuit voltage
PDA	personal digital assistant
PLI	plastic lithium ion
PMS	power management system
PROBA	Project for On-Board Autonomy
PSD	power spectral density
PV	photovoltaic
R_{INT}	internal resistance
RMS	root-mean-squared
SEC	specific energy capacity
SER	specific energy requirement
SMART	Small Missions for Advanced Research in Technology
SOC	state of charge
SSTL	Surrey Satellite Technology Ltd.
STENTOR	Satellite de Télécommunications pour Expériences de Nouvelles Technologies en Orbite
STRV	Space Technology Research Vehicle
TFB	thin-film battery
UAV	unmanned aerial vehicle
V_{EOD}	end of discharge voltage

Equation Parameters

A	area (m^2)
a	acceleration (ms^{-2})
C_{nom}	nominal Ah capacity (Ah)
E	bending modulus (Nm^{-2})
E_{bat}	energy stored by battery or multifunctional structure ($Whkg^{-1}$)
f	frequency (Hz)
G	shear modulus (Nm^{-2})
h	height (m)
I	second moment of area (m^4)
k	spring constant (Nm^{-1})
K_n	constant (dimensionless)
L	length (m)
m	mass (kg)
M_{batt}	total mass of battery (kg)
m_{cell}	mass of single cell (kg)
M_{cells}	mass of battery cells (kg)
M_{core}	mass of sandwich panel core (kg)
M_{facea}	mass of sandwich panel facesheets (kg)
M_{mfs}	mass of structure used for MFS panels (kg)
M_{panel}	mass of structural panel (kg)
M_{para}	parasitic mass (kg)
M_{sat}	mass of spacecraft (kg)
M_{stru}	mass of bus structure (kg)
Q	transmissibility at resonance (dimensionless)
SEC_{cell}	specific energy capacity of cell ($Whkg^{-1}$)
SEC_{mfs}	specific multifunctional energy capacity ($Whkg^{-1}$)
SER_{sat}	specific energy requirement of spacecraft ($Whkg^{-1}$)
V_{batt}	volume of battery (m^3)
V_{bus}	volume of bus (m^3)

V_{cells}	volume of cells (m^3)
V_{nom}	nominal voltage (V)
z	deformation (m)
α_{stru}	structural mass fraction (dimensionless)
ΔM_{para}	mass saving due to parasitic mass elimination (kg)
ΔM_{SEC}	mass saving due to change in cell type (kg)
ΔM_{vol}	mass saving due to change in volume (kg)
δ_{vol}	structural mass density (kgm^{-3})
η_{mfs}	multifunctional potential (dimensionless)
η_{pack}	cell packing efficiency (dimensionless)
η_{para}	parasitic mass fraction (dimensionless)
ξ	damping ratio (dimensionless)
ρ	mass density (kgm^{-3})
σ	direct stress (Nm^{-2})
Σ	combined stress (Nm^{-2})
τ	shear stress (Nm^{-2})

Acknowledgements

Thanks, first of all, to Dr. Guglielmo Aglietti for his supervision over the last 4 years. The sound technical advice he has given me has been of immeasurable assistance, and I doubt I would have gotten this far were it not for his remarkable ability to remain cheerful and good-humoured, regardless of how late I got into the office, how far behind my work was or how wrong my results were.

Next I'd like to thank my Mum (for checking this thesis for spelling errors) and my Dad (for the occasional bit of technical advice and emergency supplies of steel shim), and both them and my sister, Anna, for their emotional support during my studies (and for giving me somewhere to stay while I was writing up).

Many people have advised or assisted me over the course of my work at Southampton, and I wish to acknowledge the help following people in particular: Dr. Christoph Schwingshackl, whose work in this field laid the foundation for my own, and who gave me a lot of assistance to get me started on my PhD; Dr. John Owen and Dr. Dennis Doerffel, both of whom lent me their expertise on the subject of manufacturing and testing batteries; Mr. Erik Roszkowiak for his advice on composite manufacturing; and Ms. Nicola Beverage who assisted me with experimental work as part of her undergraduate project.

Lastly, I'd like to thank all of the friends who've made my time at Southampton so enjoyable with tea breaks, snooker, beer festivals, wargames, photography and other activities that distracted me from my research. I've met too many awesome people in the AFRG and elsewhere to list tem all here, but you all know who you are. Special thanks go to Nick and François (and their housemates) and to Phil who were kind enough to give me a place to sleep for a couple of days when I was living 200 miles away and had work to do down south.

Declaration of Authorship

I, **Samuel Charles Roberts**, declare that the thesis entitled **An Investigation of the Feasibility of a Spacecraft Multifunctional Structure using Commercial Electrochemical Cells** and the work presented in the thesis are both my own, and have been generated by me as the result of my own original research. I confirm that:

- This work was done wholly or mainly while in candidature for a research degree at this University;
- Where any part of this thesis has previously been submitted for a degree or any other qualification at this University or any other institution, this has been clearly stated;
- Where I have consulted the published work of others, this is always clearly attributed;
- Where I have quoted from the work of others, the source is always given. With the exception of such quotations, this thesis is entirely my own work;
- I have acknowledged all main sources of help;
- Where the thesis is based on work done by myself jointly with others, I have made clear exactly what was done by others and what I have contributed myself;
- Parts of this work have been published as listed in **Appendix I** (p200).

Signed: .....

Date: .....

1 Introduction

1.1 Spacecraft and Satellite Design

Earth orbiting satellites* play an increasingly important role in the economy and infrastructure of the planet. Communication satellites relay television and telephone signals between continents; constellations such as GPS allow accurate navigation for air, sea and road transportation. Remote sensing craft map and observe weather and terrain and provide military intelligence. Both around the Earth and beyond, scientific missions expand our knowledge of this planet, the Solar System and the rest of the Universe. Whilst the benefits of these technologies are great, the cost of space missions is also substantial, due to the difficulty of overcoming the Earth's gravity and the great reliability that is required of spacecraft, which cannot physically repaired once launched (except in exceptional circumstances, such as manned space stations or NASA's Hubble Space Telescope).

1.2 Mass Reduction as a Design Driver

Reduction of mass is one of the most important factors affecting spacecraft design. The mass of a spacecraft largely determines how much it will cost to launch, and the launching cost is amongst the largest contributions to the total mission cost, as much as 50% in some cases [1]. For an LEO (Low Earth Orbit) application, launch costs are typically US$5000 per kg of spacecraft mass; for GEO (Geosynchronous Equatorial Orbit) they can be expected to be around US$15-20000 per kg, and may be as much as $40000 [2]. Reduction in mass and size of one component also tends to favour larger overall mass reductions, as a lighter component requires less supporting structure,

* The term "satellite" shall be used to refer to spacecraft in orbit around the Earth from here onwards, whilst "spacecraft" may be taken to mean space-faring vessels in general.

and, in turn, the spacecraft requires less fuel to manoeuvre, thus requiring smaller, lighter fuel tanks, which in turn leads to a smaller structure, and so on. Thus, even a comparatively small reduction in the mass of one component of the spacecraft can potentially result in cascade reduction in the overall mass.

1.3 Origins of Parasitic Mass

Structural, inert elements may make up as much as 25% of the mass of a spacecraft, and many are often redundant – that is to say, many spacecraft subsystems have their own structure. This structure is intrinsic to the subsystem itself, and is in addition to the structure of the spacecraft bus (this being the primary structure of the spacecraft, upon which the other subsystems are mounted. The bus itself is that part of the craft that does not include the payload). For example, a typical electronics enclosure in a communications satellite completely encases the electronic components in a metallic box, which is attached to the structure of the satellite bus. The surface of the box that attaches to the spacecraft, however, is doubled with the panel it fastens to, adding parasitic mass. There are reasons why these extra masses are present, such as to facilitate handling on the ground or increase radiation protection. However, from a structural point of view, they are redundant elements.

Additional mass – for example, that occurring due to "doubled" structural members – may be reduced by using a more integrated design. Such an approach presents an engineering challenge, since it requires that two or more subsystems be designed concurrently and integrated into a single unit. However, considerable advantages can be gained by reducing parasitic mass and, in the case of subsystems that are mounted internally in the spacecraft, reducing the volume of the bus.

1.4 Multifunctionality for Mass Reduction

Structures are often designed or used to perform functions in addition to their fundamental purpose, mainly that of maintaining the spacecraft's configuration under

the loads to which its operation subjects it (for example, the mechanical environments encountered during launch, transport and thruster firings). Material selection decisions may be made to add functionality to the structure; under certain circumstances, for example, aluminium may be favoured over carbon fibre in spite of poorer structural performance, as it can also provide radiation shielding or be used as an electrical pathway. Such decisions are typically taken more with a mind to reducing the complexity or cost of a design, rather than specifically to save mass.

Such structures may be termed multifunctional structures (MFS), as they act as structural support for the spacecraft, whilst performing another function for one or more subsystems, thus effectively doing the task of several spacecraft elements. A common example of a multifunctional structure outside the field of spacecraft engineering is the semi-monocoque structure of a modern aircraft, where the metal skin of the wings and fuselage stiffens the primary structure, contains the pressurised atmosphere of the cabin, acts as an aerodynamic fairing and, in some cases, contains fuel. In comparison to this, the structure of a pre-1930s aircraft may be considered largely "monofunctional": the structure of such an aircraft was a wooden frame whose sole purpose was to carry structural loads, principally the mass of the aircraft, its payload and the lift and control forces developed by the flying surfaces. The aerodynamic fairing was provided by doped fabric, which transferred the aerodynamic forces to the primary structure, but provided little or no additional support to it. Fuel tanks were separate entities affixed to the primary structure, and whilst it is likely that their presence would have reinforced the structure in some cases, the level of structural integration was not great. (Pressurisation was not commonly used in aircraft during this era.) The technology of multifunctional structures has, however, yet to reach such a level of maturity in the space industry.

The aim of this project has been to investigate and develop means to produce multifunctional structures based on the power storage subsystem of a typical spacecraft. The power storage system, being composed of a battery of electrochemical

cells in the majority of satellites, is a good candidate for use as a multifunctional structure. As the cells are robust, numerous and identical, distributing them homogenously within a structure is quite a feasible proposition, compared to components such as circuit boards, each of which is usually unique and relatively fragile.

1.5 Range of MFS Applications

A detailed assessment of the overall field of multifunctional structures for spacecraft may be found in [3]. This section shall summarise the overall state of the art.

Various methods have been proposed to incorporate electronic components into the primary structure [4,5], one such system notably being flown on NASA's Deep Space One mission [6]. This generally involves placing electronic components directly into structural panels as multi-chip modules, thus eliminating the need for a separate electronics housing.

Thermal control is another such subsystem [5,7,8], where the core of a sandwich panel may be modified such that the structure itself becomes a passive thermal control component. One approach to this is to use a core consisting of a cellular lattice of heat pipes, rather than a conventional honeycomb.

Mechanical actuators may be made part of the spacecraft structure, mainly through the use of shape memory alloys [9-11]. Such alloys undergo a change in shape when heated to a certain threshold temperature, thus allowing a deployable structure (such as an antenna or solar array) to be constructed without the need for a separate deployment actuator and hinge, the function of both being performed by a connecting structure of shape memory alloy.

Another type of structure that may be considered, in some respects, to be multifunctional is a self-monitoring structure, which can detect whether it has suffered damage [12] or monitor the curing of composite materials [13]. In both cases,

various sensors are embedded into the composite structure prior to curing, and are subsequently used to supply data regarding its current state.

1.6 Power Structures

Several proposals have been made to incorporate the power subsystem into structures [4,14-27], and most of these focus on the power storage subsystem, specifically the electrical batteries. These technologies may be broadly split into those technologies that seek to produce electrochemical cells that have useful structural properties and those that aim to produce primary structural components incorporating cells in such a way that additional packaging is not required (i.e., using the primary structure to form the mechanical housing of the battery). The significant mass of the battery (as much as 5% of the total mass of the craft) means that correspondingly useful mass savings may be made through its modification.

One common feature that all proposed MFS technologies share is cost. Whilst their projected performance may be high, economies of scale mean that producing small runs of cells that differ greatly from mass-produced models will add significant financial cost to their application. This thesis describes how this cost may be offset by using commercially available cells to produce multifunctional structures. It will be shown how this approach allows advantage to be taken of the benefits of a multifunctional structure without incurring the costs of purpose built electrochemical components.

One of the main contributions of this work, at the system level, is a parametric study (Chapter 3), which allows the overall benefits of the spacecraft multifunctional approach to be quantified. Previous material published on this subject has only considered the effect on performance at the level of the battery or structure.

At the subsystem level, the remainder of the work is concerned with the feasibility of an MFS using commercial electrochemical cells. The major results may be split into

two parts. Firstly, these cells were tested under vibration from both a mechanical and electrical standpoint. The important original results in this section are the determination of the stiffness of commercial cells, in the particular loading case considered, and the assessment of the long-term effects of vibration on their mechanical properties. Secondly, it was seen that manufacturing such an MFS panel could be achieved whilst maintaining proper electrical and structural functions. Demonstrating the potential of this type of MFS is another important contribution to the state of the art.

1.7 Thesis Outline

Chapter 2 will describe the current work in the field of multifunctional power structures for spacecraft and other applications. In addition, the spacecraft power system shall be described in order to provide appropriate background.

Chapter 3 will show how the mass savings available from an MFS may be quantified. Whilst the performance benefits of using an MFS may be easily defined qualitatively, it is important to assess their magnitude. The mass savings available to spacecraft will be calculated according to various parameters, showing that they can be significant.

Chapter 4 considers the fitness of COTS lithium cells for the purpose of an MFS. It is shown that the cells continued to function after high intensity vibration tests, and the usefulness of the cells as structural components of a sandwich core is also tested.

Chapter 5 will address the practicalities of manufacturing a multifunctional panel of this type, showing that a conventionally produced powerstructure maintains both electrical and structural functionality. The ability of FEA (finite element analysis) software to predict the behaviour of this panel will also be assessed.

Chapter 6 applies the shear stiffness measured in Chapter 4 and the FE (finite element) modelling technique used in Chapter 5 to a design trade-off, showing that the structural performance of an MFS compares well to a conventional design.

Chapter 7 discusses the importance of qualitative factors on the potential usefulness of an MFS. The validity of assumptions made in the thesis and the significance of experimental results for future applications is also assessed.

Chapter 8 will summarise the major conclusions of the thesis.

Appendix I lists publications made as part of this work.

Appendix II describes the manufacturing process of the MFS panels in more detail than is covered in the main body of the work.

2 Review of Current Technologies

This chapter will describe the state of the art in the field of spacecraft multifunctional power structures. Technology in other relevant fields is also briefly described in order to provide the background required to set the work in context.

The review will begin by describing spacecraft in general, with a focus on their structural design, and the operation of the power subsystem and its components in more detail. This will show the requirements that the spacecraft battery is subject to and what technologies are commonly employed to satisfy these requirements. It will then go on to describe ongoing research that seeks to save mass by integrating the battery within the structure of the spacecraft.

2.1 Background

2.1.1 Spacecraft Components

A spacecraft's purpose is, essentially, to convey a payload (such as a sensor or a communications transceiver) to a specified orbit or trajectory in outer space and to ensure its operation while there. The payload must be provided with power and protected from radiation and extremes of heat and cold, and any antennae and instruments must point in the correct direction. Most of the spacecraft is made up of components to support the payload in this way. The most important subsystems on a typical spacecraft are briefly described here.

- **Propulsion:** Electrical or chemical thrusters (together with the fuel or propellant they require) are used to make substantial changes to the trajectory of the spacecraft. For most Earth-orbiting satellites, such large changes are not required for most of the mission's duration, the majority of the energy required to reach the initial orbit being performed by the launch vehicle, in combination with an apogee

boost motor for GEO satellites. For interplanetary spacecraft, however, a large proportion of the vehicle's mass will be propellant or fuel for the thrusters.

- **Attitude and orbit control:** Reaction wheels and smaller thrusters make minor adjustments to the orbit and control the orientation of the spacecraft to ensure that solar arrays, instruments and antennae have the correct field of view and thrusters are properly orientated.

- **Navigation:** Devices such as gyroscopes, accelerometers, sun sensors and star trackers are used by the spacecraft to establish its orientation.

- **Communications:** In addition to communications by the payload of communication satellites, all spacecraft need to be contacted by their ground stations to ensure correct operation, upload commands and download data.

- **On-board data handling:** Electronic computers are required to process and store information from the payload, ground controllers, sensors and so on.

- **Thermal control:** Many subsystems require a certain temperature range for proper operation. Both passive systems (such as insulation and reflective paint) and active devices (such as heat pipes) are used to ensure this is maintained.

The structure and power subsystems are of particular relevance to this work, and will be described in more detail.

2.1.2 Structure and Configuration

The main requirement of the spacecraft's primary structure is to interface with the launch vehicle and to maintain all of the other components in a specified arrangement (the configuration) under the mechanical loads to which it is subjected. This requirement may be further broken down as follows: the structure must provide for the mounting of all of these components, and must connect them to one another, transferring loads between them (and the launch vehicle interface, during launch)

without undergoing failure or subjecting the components to loads that would result in their own failure.

The mounting requirement is often fulfilled using flat panels, frequently sandwich panels of aluminium or composite materials, upon which smaller components are mounted. Commonly, these panels are connected using a frame of trusses and brackets, or the structure is built around a central tube and shear panels. Large components, such as fuel tanks, and those components from which loads originate, such as thrusters and the launch interface, will be fixed to the main structure by the shortest load path possible.

The principal loading condition the structure must face is typically the dynamic environment of launching the spacecraft, where it is subjected to mechanical vibrations from the launch vehicle's rocket engines and acoustic input from its motion through the atmosphere. Thrusters firing after launch, thermal stresses and deployment of solar arrays also place mechanical loads on the structure.

Individual subsystem components are likely to place other constraints on the configuration, and hence on the structure; a solar array or antenna, for example, needs to be mounted outside the spacecraft, and both of these (and other components, such as cameras and other directional sensors) have a requirement to point in a particular direction. The mass balance of the spacecraft must also be considered when siting fuel tanks, which will be drained as the mission progresses, thus potentially moving the centre of gravity, which could cause control issues. The thermal or radiation environment that a component requires can also affect configuration.

Reference [28] provides more information on the design of spacecraft structures.

2.1.3 The Spacecraft Power Subsystem

Before discussing how one may modify the power subsystem of a spacecraft, it is necessary to consider how this subsystem is composed and what devices comprise it.

The power subsystem of a typical spacecraft performs three distinct functions: power generation (the primary power subsystem), energy storage (the secondary power subsystem) and power management. Almost all spacecraft that operate around the Earth and the other inner planets employ a primary power subsystem consisting of arrays of solar photovoltaic (PV) cells, which produce power for the various electrical components of the craft whilst it is illuminated by the sun, along with a secondary power subsystem consisting of rechargeable batteries. These batteries are charged by the solar cells during the sunlit period, and then discharged to power the spacecraft when the sun is eclipsed or when power in excess of that provided by the primary system is required. This process is regulated by an electronic control system, referred to in this work as the Power Management System (PMS), though various other terms – power conditioning unit, power control and distribution module, power distribution system, etc. – are employed by other authors. This component is also responsible for routing the available power to the payloads or other subsystems that require it.

Other power subsystem configurations are used for certain missions (for example, radioisotope thermoelectric generators for spacecraft sent to the outer Solar System, or fuel cells on the Space Shuttle and Apollo missions). This review, however, shall concentrate on the solar cell and chemical battery-based power subsystem technology, as it is so widely used, and specifically the batteries used therein as they show most promise from the standpoint of multifunctional structures. Equally, the great maturity of this type of power system means that there is less scope for improvement by conventional means, rendering any advantages afforded through multifunctionality all the more valuable.

2.2 Battery Technologies

Various types of electrochemical cell are currently used to form the batteries of spacecraft. This section will describe the physical design of these cells, and the nature

of the electrochemical processes that operate within them, known generally as the cell chemistry.

2.2.1 Cell Configurations

The basic attributes of any electrochemical cell are the same: the cell must contain two electrodes, an anode and a cathode, held separate by some means, and a conductive electrolyte that allows a current to flow between them. The nature of the chemicals that form the two electrodes and the electrolyte causes a flow of ions to occur across the cell, resulting in a charge differential between the two electrodes. Forming an external electrical connection between them allows a current to flow, by which means the energy contained within the cell is harnessed, until the chemical reaction that causes it is exhausted. In the case of a rechargeable cell, applying a larger voltage across the electrodes at this point causes a current to flow in the opposite direction, and reverses the reaction [29].

A functioning electrochemical cell can be produced by simply placing two electrodes of different metals in an aqueous solution of an appropriate electrolyte, but, naturally, this will not produce a practical cell with useful performance. Certain approaches have been adopted to facilitate the manufacture of rugged electrochemical cells with the best possible electrical performance, in terms of their energy capacity, lifetime and power output.

The great majority of cells use a liquid electrolyte, and there are two configurations commonly used for such cells, cylindrical and prismatic. In both cases, the cell is contained within a metal canister, which contains the electrolyte and prevents the active components of the cell (which are usually quite reactive) from being oxidised by the atmosphere.

The **cylindrical cell**, as in Figure 2-1, is by far the more common, thanks to its ease of manufacture. In addition, the inherent efficiency of a cylindrical structure,

particularly when subjected to internal pressure (as is the case with electrochemical cells due to the processes that take place within them) makes the design relatively light. A cylindrical cell's active components may be arranged in one of two ways: either by winding the electrodes and a separator into a roll, which is then placed inside the cylindrical canister, or by using a cylinder and rod as the two electrodes. In either case, the electrolyte is then added as a liquid before the cell is sealed.

Figure 2-1 - Cylindrical nickel-metal hydride battery

The **prismatic cell** (Figure 2-2, battery assembly shown in Figure 2-4) consists of a stack of alternating cathodes and anodes that are encapsulated in a prismatic case and saturated with electrolyte. Such a cell is less easy to mass-produce and the canister is less structurally efficient, but is often preferred for spacecraft applications due to the volumetric efficiency of the design. In other respects, the cell is similar, with a liquid electrolyte being used.

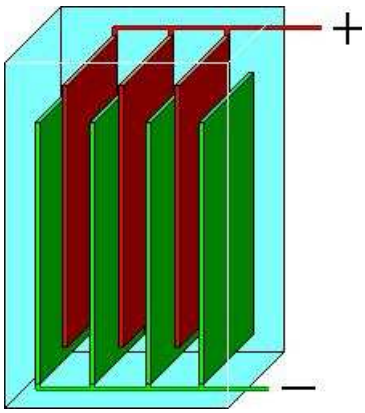

Figure 2-2 - Schematic of prismatic cell

Another configuration is the **bipolar cell** stack [30], where complete batteries of cells are fabricated without the need for stand-alone unit cells. Each cell is sealed between

two metal plates (with an insulator around the edges), and these plates then provide connections between cells (by simply stacking them together) as well as sealing them. Rather than several overlapping electrode plates forming a single cell, each pair of electrodes is a single cell, and the cells of the battery are assembled in series in a single module. This type of battery is lighter and can deliver higher currents than one based on conventional prismatic or cylindrical cells. A schematic of a bipolar battery is shown in Figure 2-3.

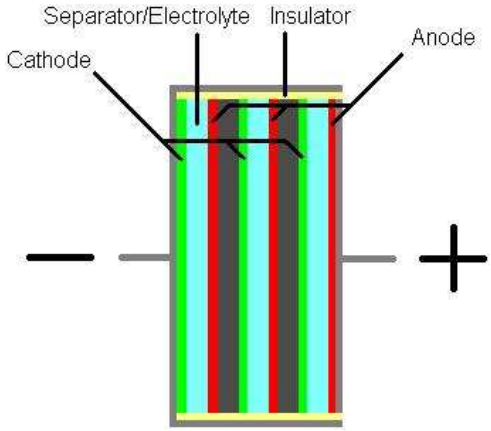

Figure 2-3 - Schematic of 3-cell bipolar battery

Similar to the bipolar battery, in some respects, is the **bicell**, being a single integrated battery that incorporates two electrochemical cells. The cells share one common electrode, either the anode or cathode, which is sandwiched between two of the other electrodes. This concept is not commonly employed, but has been proposed for use in certain multifunctional battery concepts, as will be described subsequently (Sections 2.3.2 and 2.3.3). An advantage of this design, from the perspective of using the battery as a structural element, is that the cell's internal components may be symmetric about three axes.

The internal configurations of nickel-hydrogen and lithium based cells are unique to their particular chemistry, and so will be described in the relevant section.

2.2.2 Batteries and Structure

In order to consider the removal of the inert, parasitic structure of the spacecraft battery, one must first establish the nature of this structure. It can be considered that the secondary power system's structure has two major elements. One is the structure of the individual cells, which contains any liquid components of the cell electrochemistry as well as maintaining the solid parts in the correct configuration. This is a metallic encapsulation in the case of liquid-state cells (see Figure 2-1), a pressure vessel for nickel-hydrogen cells (Figure 2-5) and a polymeric material blended with the active cell materials, combined with a thin laminated encapsulation of plastic and aluminium, for solid cells. If the active materials are sufficiently stable, the former may be omitted in some or all parts of the latter type.

The other principal element of the battery structure is a crate or other assembly that incorporates the necessary number of cells to form a battery of the requisite nominal voltage and capacity, an example of which is shown in Figure 2-4. This structure secures the individual cells in place and allows the battery to interface with the primary bus structure.

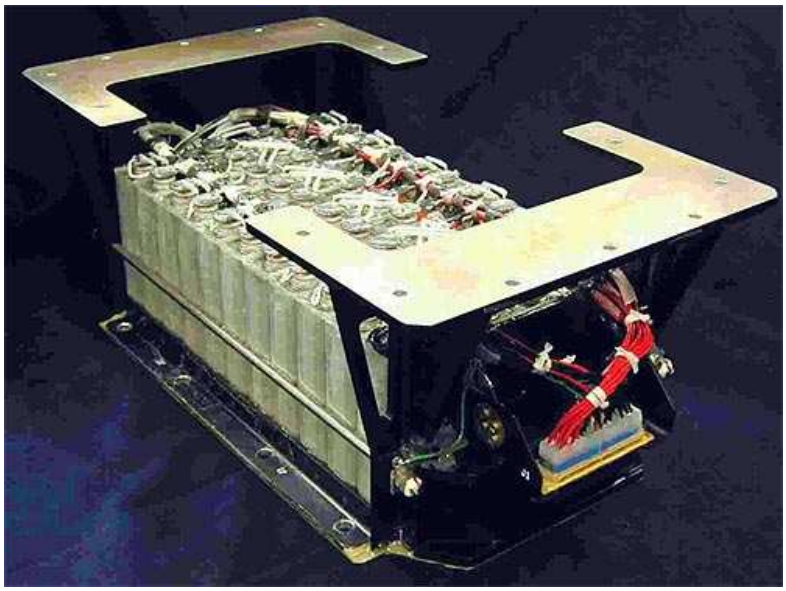

Figure 2-4 - EEI satellite battery (Image © 2006 Electro Energy Inc)

2.2.3 Cell Chemistries in use in Space

Three main types of electrochemical systems make up the bulk of batteries in spacecraft operating today: nickel cadmium, nickel metal hydride, and nickel hydrogen cells. The first two of these are liquid alkaline cells, whilst the latter are based on a hybrid of alkaline and gaseous hydrogen chemistry. Other chemistries have seen some use; in recent years, lithium-ion cells, in particular, have rapidly become the more popular choice for spacecraft batteries, especially on low cost satellites, and are now widely accepted for various missions. Silver-zinc batteries are more specialised, and have been used as a primary power source on short duration missions and on launch vehicles. Other chemistries have been suggested as potentially useful for use in space but have yet to find an application (such as high-temperature sodium-sulphur cells) or have a very limited application, such as the non-rechargeable lithium-titanium disulphide cells used on the Huygens probe [31].

Large commercial spacecraft, such as telecommunication or remote sensing satellites, have historically used purpose built cells, as the improved performance of cells that are designed for space applications justifies their higher cost when power requirements exceed a few hundred watts. For smaller satellites, however, commercial cells are often more appropriate. Although commercial cells have poorer performance than aerospace grade cells, they are often more cost-effective in the context of a small, cheap satellite [32], and their high performance makes them increasingly acceptable for larger missions.

The principal factor determining the mass of the secondary power system is the specific energy capacity (SEC), or the amount of electrical energy a cell can store per unit mass. The volumetric energy density (energy per unit volume) is also important, as a larger battery volume requires a larger (and thus heavier) bus. Specific power and power density, the maximum power output per unit mass and volume respectively, are also relevant. Values of specific energy for various cell chemistries are given in Table 2-1. Different battery types react differently to certain conditions, such as

continuous cycling or low temperatures, and this sometimes results in batteries with relatively poor specific energy being chosen for certain applications.

Cell chemistry	Specific energy ($Whkg^{-1}$)
Nickel-cadmium (Ni-Cd)	35 - 60
Nickel Metal Hydride (Ni-MH)	50 - 80
Nickel-Hydrogen (Ni-H_2)	40 - 60
Zinc-Silver (Ag-Zn)	60 - 100
High temperature Sodium Sulphur (Na-S)	100 - 150
Lithium (Li-ion, PLI, LPB, etc.)	120 - 250+

Table 2-1 - Battery performance [29,32-39]

Other important factors are the depth of discharge* (DOD) and cycle life† that are required of the power system. These two parameters directly affect each other; a higher depth of discharge per cycle results in the battery sustaining more unrecoverable loss of capacity per cycle, thus decreasing the number of charging and discharging cycles it can undergo before the performance decays below an unacceptable level. However, using a lower depth of discharge effectively reduces the specific energy.

* Depth of discharge is the proportion of the battery's total capacity that is actually used, normally expressed as a percentage. For most cell chemistries, discharging all or most of the capacity of a cell will cause severe losses of performance.

† Cycle life is the number of charge-discharge cycles the battery is required to undergo during the lifetime of the spacecraft, defined generally by the number of eclipses to which it is subjected. In LEO this is roughly 5000 cycles per year of the mission; in GEO, on the other hand, only 84 eclipses occur each year.

Nickel Cadmium and Nickel Metal Hydride

Nickel cadmium (Ni-Cd) has been the battery of choice for most LEO satellites since the 1970s, thanks to its capability to undergo many charge-discharge cycles. Until recently, nickel metal hydride (Ni-MH) technology has lagged behind nickel cadmium in this respect, but advances in cell chemistry have allowed spacecraft designers to take advantage of the superior specific energy offered by Ni-MH cells. These alkaline cells are generally very tolerant of high and low temperatures, being able to operate from -20 to 60 °C.

The nickel-cadmium cell uses pure cadmium as an anode, with a solid nickel oxide cathode and an aqueous liquid electrolyte of potassium hydroxide. Nickel metal hydride cells use the same cathode and electrolyte, but the anode consists of a metal hydride (an alloy that is capable of absorbing large volumes of hydrogen, such as $LaNi_5$) [29]. Both cells have an open circuit voltage (OCV) that varies from 1.2 - 1.5 V according to charge level.

Ni-Cd and Ni-MH cells are supplied in prismatic and cylindrical form, and work to develop bipolar cells for use in space is ongoing.

Nickel Hydrogen

Nickel hydrogen ($Ni-H_2$) cells [29] are used by most GEO satellites and large satellites in LEO, as they are capable of very deep discharges without severe hysteretic effects. Nickel hydrogen cells are capable of sustaining roughly 15% deeper discharges for the same number of cycles to failure when compared to Ni-Cd [37]. Due to the relatively small number of eclipses which occur during the lifetime of a GEO satellite, this deep discharge allows for a reduction in the mass of the storage system, since more of the battery's capacity is used, even if its total specific energy is slightly inferior to Ni-Cd or Ni-MH, and the volume specific capacity is much worse.

Ni-H_2 cells utilise a nickel oxide anode with an alkaline electrolyte, like that used in Ni-Cd and Ni-MH cells. However, the cathode is the platinum-hydrogen electrode used in H_2-O_2 fuel cells, producing a nominal voltage of 1.5 - 1.6 V. The cell is a pressurised container, which contains the hydrogen and also the electrodes and electrolyte (see Figure 2-5); in some cases, all the cells in a battery may share a single pressure vessel, or there may be several common pressure vessels, rather than an individual vessel for each cell. Sharing a pressure vessel increases specific energy, but comes at the cost of reduced reliability since a single vessel failure results in the loss of more than one cell.

Figure 2-5 - Nickel-hydrogen battery (Image © & courtesy of JAXA)

Other Chemistries

Silver-zinc (Ag-Zn) batteries are used in some LEO satellites, but are less popular as the prohibitive cost of the electrode materials and poor shelf and cycle life generally does not justify the improvement in specific energy. Ag-Zn batteries are alkaline cells with aqueous liquid electrolytes, with an OCV of 1.4 - 1.8 V [29]. They are used on launch vehicles such as the Boeing Delta II and some scientific craft such as NASA's Ranger photographic missions to the moon, where they need only be charged and discharged once. As such, they are effectively used as primary (non-rechargeable) batteries in most cases.

High temperature sodium-sulphur (Na-S) batteries are attractive due to their excellent specific energy and high voltage (around 2.5 V). An experiment on board the US Space Shuttle in 1997 was conducted to investigate the behaviour of Na-S cells in zero gravity [40]. However, the fact that the cells need to be heated to 350°C and contain hazardous and corrosive elements (liquid sodium and sulphur) renders them seemingly unsuitable for normal missions, as the thermal control, ground safety and packaging issues would seem to outweigh any potential benefits from mass savings [29,40].

Lithium-based rechargeable cells compare favourably to current technologies in most respects, and they are beginning to establish a significant foothold in the spacecraft battery industry. Given that lithium chemistry is set to be the most used secondary power system in near-future spacecraft, lithium cells will be described in detail in the next section.

2.2.4 Lithium-Based Batteries

Background

Lithium is a highly attractive material to act as an anode in an electrochemical cell. As well as being very light (and thus having a high charge capacity per unit mass), it is also the most electropositive element, which translates to a high nominal cell voltage – from 2.5 V to over 4 V depending on the precise chemistry of the cell. As the specific energy of a battery is given by its charge capacity multiplied by its voltage, lithium cells have very large specific energy capacities when compared to most other technologies currently used in space applications, as indicated earlier in Table 2-1.

In addition to giving superior capacity, the higher voltage of lithium cells means that they require less individual cells to be connected in series for a given total voltage, reducing the amount of cabling necessary between cells to produce a battery with the required specifications [29]. Liquid based lithium cells also have good cycling and

thermal characteristics, with some cell types able to operate from -30°C to +60°C [41], and have demonstrated resistance to radiation [42,43].

The first rechargeable lithium cells, developed in the 1980s in Canada, were conventional in configuration, being available in cylindrical and prismatic form. Safety issues with these early batteries, which used an anode made of pure lithium metal, resulted in the development of the lithium-ion cell, where lithium ions are intercalated in solid carbon (usually graphite or coke) to reduce the danger of explosion if cells are overcharged or short-circuited. Although this slightly reduces the specific energy (due to the additional mass of the carbon), the cycling capability of the battery is greatly improved thanks to the elimination of problems associated with electroplating of lithium onto the anode during charging.

Rechargeable lithium cells have seen use in commercial space applications, and both primary and secondary lithium cells have been used on various experimental and scientific craft [44]. NASA and the Naval Research Laboratory (NRL) in the USA have investigated lithium cells for use in space since the mid 90s, testing both Saft and Lithion cells [45,46]. JAXA, in Japan, have undertaken similar tests [47], and it was through the excellent performance of its lithium cells that their HAYABUSA probe was able to survive a potentially catastrophic attitude control failure [48]. The European Space Agency (ESA) initially began consideration of lithium-ion cells for spacecraft in 1997 [49], with the intent to develop a lithium-ion battery system using commercial off-the-shelf (COTS) cells for use in GEO satellites in partnership with COMDEV in Canada [50]. Eagle-Picher Energy Products and Lockheed Martin Missiles and Space, on the other hand, have developed large (25 Ah) lithium cells for use in space (and other aerospace) applications [38,39,51]. Testing for shocks, vibration, thermal behaviour and cycle life have all given promising results, although there has been some concern about the behaviour of the cells under variable temperature conditions [52].

AEA technology (also known as AEA Battery Systems Ltd., or ABSL), in the UK, and Saft, in France, have completed similar tests on lithium-ion technology, and both have seen their systems fly on space missions. An AEA power system using COTS Sony 18650HC [36] cells (18 and 65 refer to the diameter and length of the cell in mm respectively) was originally trialled on the STRV (Space Technology Research Vehicle) and PROBA (Project for On-Board Autonomy) experimental missions. Since then, AEA lithium-ion batteries (using the same cells) have been employed on such craft as ESA's Rosetta and Mars Express probes and the Giove-B test bed built by Surrey Satellite Technology Ltd. (SSTL) for the Galileo navigation system. Mars Express and PROBA are notably still in operation as of mid 2008, having been launched in 2004 and 2001 respectively [53].

Saft have undertaken life cycle tests on large lithium-ion cells [54] that suggest they are excellently suited to operation in geostationary orbit. Saft's VES140 lithium-ion cells were used on the STENTOR (Satellite de Télécommunications pour Expériences de Nouvelles Technologies en Orbite) experimental communications satellite (lost in the failure of the Ariane-5ECA launcher) and are currently in use on the Eutelsat W3A communication satellite, launched in 2004, which was the first commercial satellite to use lithium-ion cells [55]. The Eurostar 3000 bus, used by EADS Astrium for this and other GEO communications satellites, now uses lithium cells as standard [56]. ESA's low-cost moon probe, SMART-1, also used Saft cells [57].

Lithium and lithium-ion polymer batteries, LPBs and LiPBs [4,17,19,38,39,58], use a similar chemistry to standard lithium cells, but both the electrolyte (which is in this case a solid) and the cathode are blended with a solid polymer (usually polyethylene oxide). This makes the cell very rugged, and eliminates the possibility of evaporation or leaking of the electrolyte, such that the cell's case only has to be a thin oxygen barrier (like the sachets used by the food industry to encapsulate products like instant coffee), rather than a relatively heavy metallic can. The major operational drawback of LPBs is that the solid electrolyte only becomes adequately conductive at relatively

high temperatures, often as much as 60-100 °C [29], although some types are now able to operate down to 10 °C [39].

Thin-film LPBs [4,17,19,59,60] are capable of operating at ambient temperatures, and have demonstrated better cycling and high current characteristics than other LPBs. Thin-film LPBs are deposited onto a substrate (which could be polymeric, ceramic or metallic) using a vapour deposition technique (where the materials are vaporised under vacuum and then deposited onto the substrate). Each layer is only a few μm thick. The cathode and the electrolyte are the same as described previously, whilst the anode is commonly pure lithium [59,60]. The main drawback of thin film batteries is that they need the same level of environmental protection as other lithium batteries - this means that the mass of the encapsulation can become significant with respect to the mass of the battery itself. In addition, the batteries need a large area of substrate to be deposited onto, in order to provide substantial capacity, as they provide as little as 0.8 Wh of capacity per square metre of battery [4].

The plastic lithium-ion (PLI) cell (an example is shown in Figure 2-6) is a combination of the lithium ion and LPB technologies [29]. The PLI cell uses the same chemistry as the lithium ion cell with a polymeric electrolyte - a gel that is impregnated with a liquid electrolyte such as $LiPF_6$. Currently, this provides the best compromise between the two types. Although the gel electrolyte is not as robust as a polymer electrolyte (i.e., it is prone to gassing and leaking), PLI batteries may still be produced in thin prismatic form using simple “coffee bag” encapsulation and no additional structure, and, in addition, have good performance at high and low temperatures.

It should be noted that the naming of such cells vary greatly between manufacturers and other sources. For the purposes of this work, the terms lithium polymer and lithium-ion polymer will be applied to cells with truly solid electrolytes, while plastic lithium-ion will be used to describe cells with liquid components held in a gel (such

cells are also termed "soft pack" lithium-ion cells). This convention does not hold true throughout the available literature, however.

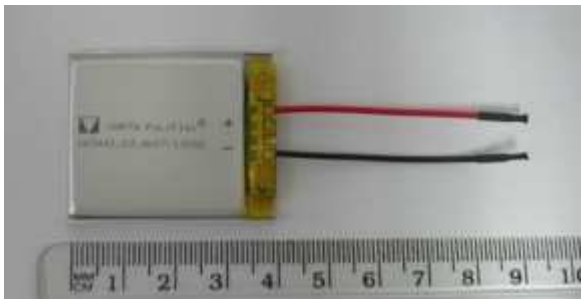

Figure 2-6 - Varta PoLiFlex PLI cell

A typical rechargeable plastic lithium-ion cell is a laminated stack consisting of an anode of lithium intercalated in graphite or another carbonaceous material, a gel polymer doped with electrolyte and a cathode which is normally $LiCoO_2$ (alternatives include $LiNiO_2$ and LiV_2O_5), as in a standard lithium-ion battery [29]. There is a metallic (copper or aluminium) current collector in contact with each electrode; in practice, there may be several electrodes, the resultant "cell" being effectively several cells in parallel, or the single cell may be folded or wound into a roll; the end result is the same. The entire cell is hermetically encapsulated, usually with a laminated plastic-aluminium membrane, to prevent oxidation of the lithium-based electrode materials and gassing of the volatile electrolyte components. Testing has successfully been undertaken to qualify commercially available examples of this battery type for use in spacecraft applications, as detailed in [61].

Disadvantages of Lithium Chemistry

The biggest disadvantages of lithium batteries are their relative unfamiliarity to the space industry and the tight control that must be exercised over their charging and discharging. Since lithium cells are recent technology, there are less data regarding their cycling ability and long-term performance.

Commercial cells, in particular, are designed to operate for a lifetime of the order of 500 cycles [34], approximately one month in LEO, with a charge/discharge profile completely unlike that required of a spacecraft battery. There would be little motivation for battery manufacturers to study such a regime, as the market for spacecraft batteries is insignificant compared to that for mobile telephones, PDAs and so on. Thus, the deterioration and failure modes of lithium cells have not been studied extensively when compared to established chemistries, such as Ni-Cd, which has been employed in space since the 1960s. Given the justifiable conservatism that pervades the space industry, the increased risk of using an unproven technology for a long duration mission would be unacceptable, even in the face of large mass benefits. The heritage of AEA's original cell, the Sony 18650HC, is now reaching a level where it is trusted for use in interplanetary probes and other large missions, but the performance of these older cells is notably poorer than that of the newest technology, with an SEC around half that of the latest lithium batteries.

When compared to current space-qualified technologies (Ni-Cd and Ni-H_2), the charge control regime for lithium cells is far more stringent, and, all else being equal, the rate capability (maximum deliverable current) poorer. Where Ni-Cd cells can sustain constant overcharging without damage, and the charge level of Ni-H_2 cells is easily monitored thanks to the variation in hydrogen pressure with charge level, lithium cells must be charged using a precise "CC-CV" (constant current, constant voltage) profile. If lithium cells are subjected to an excessive charging current or voltage, they can undergo irreversible capacity loss or even explode or catch fire [62].

To ensure that all cells receive an equal charge, manufacturers recommend that no more than four cells be connected in series. If more cells are used, variation in capacity and internal resistance between cells may result in some cells being subjected to over voltage and thus damaged. Under normal circumstances, this complex charge regime requires a more sophisticated PMS than other systems, since eight cells must be connected in series for a typical 28 V spacecraft bus. This, in turn, means that the

battery may not be treated as a closed "black box" system. Instead, the individual cells must be operated in series for discharge, and then be charged in blocks of four or less, or individual cells must be "shunted" once they are fully charged by the constant current regime [39].

The alternative to this is to screen cells prior to assembling the battery and ensure that the variations in capacity and internal resistance are minimised. However, this process naturally increases the cost of the battery, as many more cells must be bought than are actually needed, and time and facilities are required to complete the necessary testing.

2.2.5 Comparison of Lithium vs. Conventional Chemistry

Although lithium batteries are now commonplace in spacecraft, nickel cadmium is still a popular choice for many missions, particularly large spacecraft. A detailed comparison of a COTS Ni-Cd cell used by SSTL in low-cost space applications against state of the art commercial thin PLI technology is given in Table 2-2.

The critical attributes of these cells are the energy they store and power they can deliver per unit mass and, to a lesser extent, per unit volume. Given a particular requirement for the battery's performance, these values determine its mass and volume.

As can be seen, the specific energy of the PLI cell is around six times more than the Ni-Cd cell, and hence the mass of a battery made of PLI cells would be six times less if energy storage was the driving factor. Volumetrically the difference is less marked, with the PLI cell performing around four times better. However, it should be noted that the cylindrical Ni-Cd cell would not pack as easily as the flat, prismatic PLI cell, and so the difference in a complete battery would be more significant.

If maximum power output is the principal sizing requirement of the battery, the PLI cell still performs better, but the advantage is less significant. In this case, the mass of

the PLI battery would be roughly three times less, and its volume around half that of the Ni-Cd one.

Attribute	**Varta PoLiFlex** PLF523450D [34]	**Sanyo Cadnica** KR-7000F [35]
Chemistry	Lithium-ion	Nickel-cadmium
Configuration	Plastic soft pack	Liquid cylindrical
Nominal voltage	3.7 V	1.2 V
Nominal capacity	960 mAh	7000 mAh
Mass	16 g	230 g
Volume	8.70 $x10^{-6}$ m^3	7.88 $x10^{-5}$ m^3
Specific energy capacity	**222 $Whkg^{-1}$**	**36 $Whkg^{-1}$**
Volumetric energy density	**408 Whl^{-1}**	**107 Whl^{-1}**
Maximum rated current *	2 *C* = 1.92 A	4 *C* = 28 A
Maximum specific power	**444 Wkg^{-1}**	**146 Wkg^{-1}**
Maximum power density	**817 Wl^{-1}**	**426 Wl^{-1}**

Table 2-2 - Comparison of typical COTS cells

PLI batteries are typically supplied as smaller units than Ni-Cd cells, i.e., individual PLI cells are smaller in capacity than individual Ni-Cd cells. This means that more cabling is required to assemble the battery, especially if the cells are distributed throughout the spacecraft, adding mass. However, such a large number of cells connected in parallel also results in greatly enhanced reliability, since a single cell failure results in a far smaller total loss of capacity, something that would be required for a less trusted technology in any case.

* A "*C*" rate refers to a current as a proportion of the battery's capacity. A current of 1 *C* (in amps) means that the discharge is at a rate of the battery's capacity (in amp-hours). Thus a current of 1 *C* will fully discharge the battery in 1 hour, 2 *C* will discharge in half an hour, and so on. Maximum current is defined by various means; in this case, the maximum sustained current quoted by the manufacturer is used.

Comparing performance to cost, on the other hand, gives very different results, shown in Table 2-3. To assemble a battery of PLI cells costs over 4 times more than an equivalent battery of Ni-Cd cells, not including packaging, wiring, control modules and so on, of which the latter two would be more costly for a PLI cell (the smaller cells requiring more connections, and lithium cells requiring more charge control). If power is the deciding factor, the cost is nearly ten times higher. However, referring back to [2], the cost of launching a spacecraft into LEO is of the order of US$5000-10000 per kg of launch mass. Comparing this to the attributes of the cells, in terms of their capacity and power, shows that the purchase cost of COTS cells is less important than their contribution to the cost of launching the spacecraft.

Attribute	Varta PoLiFlex	Sanyo Cadnica
Unit cost (approx)	US$30	US$16
Energy cost (to purchase)	US$8.45 per Wh	US$1.90 per Wh
Power cost (to purchase)	US$4.22 per W	US$0.48 per W
Energy cost (to launch)	US$23-45 per Wh	US$140-280 per Wh
Power cost (to launch)	US$11-23 per W	US$35-70 per W

Table 2-3 - Comparison of typical COTS cells by price

The cost of purchasing the Ni-Cd cells is insignificant compared to the cost of launching them to LEO – the purchase cost is of the order of 1% of their contribution to the launching cost. For the PLI cell, the lower mass means that purchase cost is more significant, being 20-40% of the cost of launching the battery. The most notable conclusion, however, from these data is that the overall cost (combining purchase and launch cost) of a PLI battery is 3-5 times less than that of a Ni-Cd battery.

Finally, the solid-state nature of PLI batteries renders them an attractive choice for multifunctional power structures. Thin batteries can be unobtrusively incorporated into sheet materials or attached to them with little additional mass required, meaning that the complete battery retains the very high energy density displayed by the cells. By comparison, Ni-Cd batteries (which already have more inherent structure due to

the metallic 'can' type construction of the cells) must be assembled in dedicated packaging that adds extra volume and mass to the spacecraft.

2.3 Current Multifunctional Power Structure Systems

Various companies and agencies have produced prototype multifunctional power structures. These power structure systems will be described in the following section.

2.3.1 ITN Energy Systems, Inc.

ITNES is a US company that has proposed several multifunctional power systems based on thin film lithium polymer batteries (TFBs) and solar photovoltaic (PV) materials. The firm is based in Littleton, Colorado.

Flexible Integrated Power Pack

The first of these systems is the "Flexible Integrated Power Pack" (FIPP) [4], which would be a complete power system in one thin-film material. The proposed FIPP comprises a 3-layer laminated film made up of thin PV cells, thin-film (less than 0.1 mm) lithium polymer batteries and power management electronics on a polyamide substrate. The resulting material would be attached to the outer skin of a spacecraft, providing power generation, storage and control without the need for additional structure, assuming that the surface area of the spacecraft was adequate to produce the power required. GSE, a company part owned by ITNES, have produced flexible PV cells on a polyamide substrate with a total thickness of less than 0.1 mm, and ITNES have considerable experience in manufacturing TFBs. A prototype flexible power management system, also constructed on polyamide, has also been produced.

If more area was required, the FIPP could be fixed to normal array panels. Given the poor conversion efficiency of the PV cells used in the FIPP when compared to the latest gallium arsenide technology, it does not present an economical alternative to

stand-alone solar arrays using a conventional structure, as it would require a doubling of array size; however, if a novel, lightweight structure were used, significant savings could be made.

Although a demonstration FIPP unit has been built as a proof of concept, there are no production FIPP units in service yet. However, an experimental lightweight solar array using similar PV cells was flown on the 2006 NASA TacSat-2 mission [14]. MicroSat Systems, Inc. produced the "Folded Integrated Thin-film Stiffener" (FITS), a self-deploying array structure that takes advantage of the minimal mass of such PV cells. Although the deployed area of the array is significantly larger than that of a conventional one, allowing for a projected end-of-life (EOL) efficiency of 5-6%, the FITS array is still 50% lighter than an equivalent array of comparable output. Of course, even if it were modified to incorporate a battery and power management electronics, such an array structure would not be particularly multifunctional, but it is noteworthy that the same power system components could be affixed to the main structure of the spacecraft, with any additional power requirement being made up by a lightweight array.

LiBaCore

Another technology proposed by ITNES is LiBaCore, standing for Lithium Battery in a honeycomb Core [17]. The principal of LiBaCore is to fabricate ITNES's TFBs on the large amount of otherwise unused surface area available within a honeycomb core as shown in Figure 2-7. This results in a structural sandwich panel with significant integrated power storage, with the only additional mass being that of the cells themselves.

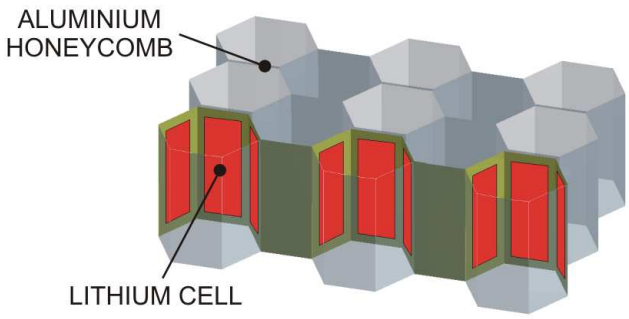

Figure 2-7 - LiBaCore concept

In order to deposit TFBs onto aluminium or titanium aluminide (the normal materials used for honeycomb cores), significant changes had to be made to the fabrication techniques - specifically, the process had to be altered to allow a lower fabrication temperature. Since the normal cathode material ($LiCoO_2$) has to be heated to temperatures above the melting point of aluminium, a different material had to be used, namely lithium molybdenum oxide. A demonstrator was produced and operated, but once again, the technology is not yet in use. The demonstration panel was based on lab-produced cells that were encapsulated in paraffin wax, which is a poor system in terms of both effectiveness and mass. As a result, the capacity of the cells degraded rapidly and significantly (to less than 10% of initial capacity), so little can be inferred regarding the electrical performance of the cells [17].

Power Fibers

Power fibers [19] are the next iteration of thin-film lithium batteries in multifunctional structures from ITNES. The principal of a power fiber is to deposit the batteries directly onto a thin fibre of carbon, glass, silicon carbide or a metal as shown schematically in Figure 2-8. The resultant "power fiber" may then be used to produce a woven fabric, composite material or simply a very compact battery (since batteries deposited on 50 μm fibres have a very large surface area when compared to those fabricated on sheet materials). ITNES have produced several different power fibers, using various substrate and electrode materials, and even "power composites"

incorporating multiple power fibers in an adhesive matrix. Tests on the power fibers have indicated that they have outstanding properties in terms of rate capability (up to 50 *C*) and cycle life, surviving for over 2000 cycles at 100% depth of discharge for a 50 *C* discharge rate, and over 90000 cycles at 100% DOD for a discharge rate of 8 *C*.

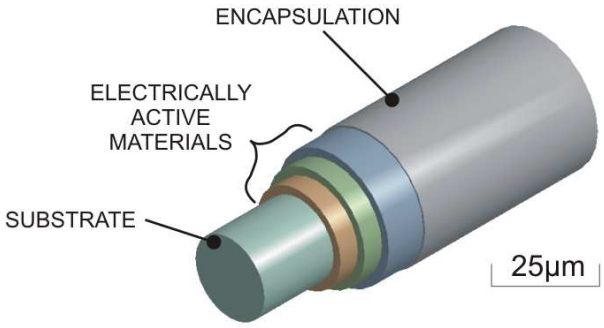

Figure 2-8 - Powerfiber concept to approximate scale

2.3.2 Boundless Corporation

Boundless, another US company, is based in Boulder, Colorado. They have developed advanced power systems for NASA, and have proposed several multifunctional structure systems based on power storage.

PowerCore

PowerCore™ [16] is in some respects a similar technology to ITN's LiBaCore system (see Section 2.3.1), consisting of a battery system which also acts as a core for a sandwich material. The principal difference is that PowerCore uses Ni-MH battery chemistry instead of lithium. Rather than depositing the battery onto a sheet for fabrication into a honeycomb, the honeycomb structure is fabricated from nickel foam, and then the active electrode materials are sintered onto it [18]. The nickel foam honeycomb has similar properties to an equivalent aluminium structure, and so the only mass contributions from battery are the active materials (nickel oxide and metal hydride electrodes and potassium hydroxide electrolyte) and the encapsulation necessary to avoid leakage. Effective specific energy capacities (where the effective

mass of the "battery" is as the mass of the multifunctional structure minus the mass of the inert structure it replaces) in excess of 80 $Whkg^{-1}$ were achieved for some samples, and theory suggests that further optimisation could easily provide over 100 $Whkg^{-1}$.

Although initial demonstration units of PowerCore were produced as early as 1998, there have been no further publications of results, and there is no evidence of imminent commercial exploitation. It seems likely that Boundless have abandoned NiMH technology for the lighter lithium technology used in their structural bicells.

Structural Bicells

As described in Section 2.2.1, a bicell is a single integrated battery that incorporates two electrochemical cells. The cells share one common electrode, either the anode or cathode, which is sandwiched between two of the other electrodes. In the case of Boundless' structural bicells, the common electrode is a standard $LiCoO_2$ cathode, whilst the two anodes are composed of a partially saturated carbon fibre composite [26,27]. The carbon fibres act as the intercalation compound for lithium ions, but because they are partially reinforced with resin, they also provide considerable structural support [15]. Since the fibres pass in and out of the matrix, the entirety of the carbon cathode can intercalate lithium even if the fibre mat is almost entirely reinforced; only one face of the anode needs to be free of resin.

Flat bicells have been constructed for general reinforcement and use as core components, with vibration testing being undertaken at the University of Southampton on a sandwich panel that uses these bicells to form part of its core [63-66], as shown in Figure 2-9. Boundless also fabricate corrugated bicells in order to make honeycomb cores entirely from structural bicell materials.

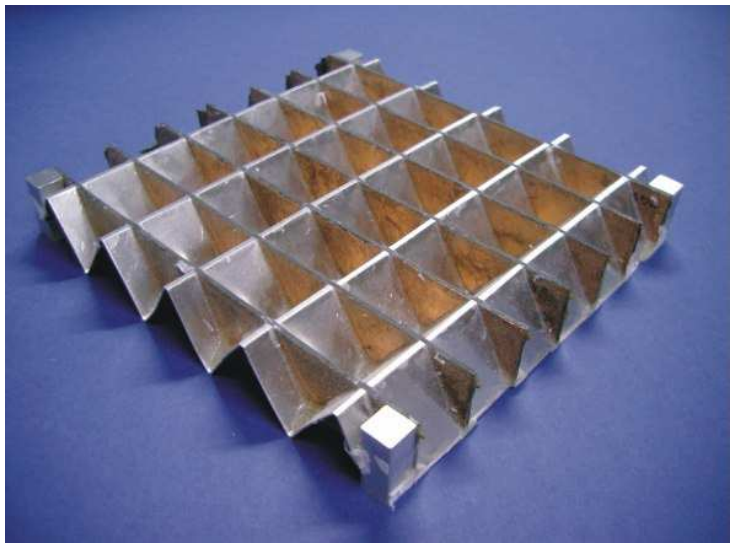

Figure 2-9 - Core of bicells (copper colour) and aluminium (image © Dr C. W. Schwingshackl)

2.3.3 US Army Research Laboratory

The US Army's Weapons and Materials Research Directorate has undertaken design and testing on structural bicells [20] that are similar to those produced by Boundless, in that they use structural carbon fibre as an anode material. However, rather than using a single structural part, every electrochemical component of the US Army cells is designed with structural performance in mind. The $LiFePO_4$ cathode, while not itself structurally useful, is cast on a perforated stainless steel substrate that is selected for structural properties as well as acting as a current collector. The electrolyte is a solid polymer, which acts as a matrix for an electrode separator composed of woven glass fibres.

As for the Boundless cells, this technology is at an early stage of development. Initial work has focussed on selection of appropriate materials (e.g., woven rather than unwoven carbon fibre, perforated stainless steel foil rather than woven mesh) and proof of concept. The electrode materials have both been tested for capacity and cycling characteristics, and some investigation of the conductivity of the electrolyte has been undertaken. A fully operation composite battery has not yet been

successfully constructed due to insulation issues, however a non-functional battery has been tested structurally and found to have a tensile modulus of 8 Gpa.

2.3.4 Structure Power Systems for other Applications

Unmanned aerial vehicles (UAVs) have some features in common with spacecraft, which make multifunctional structures an attractive and economical proposition. The small size of most UAVs means that mass savings in all subsystems are critical. Many of the smallest UAVs are all electric powered, and so in their case the batteries are a large proportion of the total mass; a reduction in battery mass (or rather, an increase in effective specific energy) translates to a significant increase in available payload or maximum range.

The Multifunctional Materials Branch of the Defence Advanced Research Projects Agency (DARPA) and the Naval Research Laboratory (NRL) in the USA have introduced the use of multifunctional structures for small unmanned aerial vehicles (UAVs), also known as micro unmanned aerial vehicles (MAVs or "μAVs"), in partnership with the UAV manufacturer AeroVironment, Inc. [21-24]. The Wasp UAV has part of its wing upper surface replaced with PLI batteries (the metallic foil on the wing in Figure 2-10 is the encapsulation of the battery). Rather than producing generic structural power storage materials, the UAV's battery and structure are designed from the outset to have optimal power storage and structural performance, using multi objective analysis [67] to achieve maximum endurance. Computerised tools are used to optimise the design of structural power elements. Analysis of conceptual designs suggests a potential 10% improvement in endurance over the best monofunctional batteries available, which would allow an optimised Wasp to fly for 1 hour 47 minutes from a single charge [68].

Figure 2-10 - AeroVironment Wasp showing multifunctional batteries on wings
Battery on left wing outlined in red. (Image © 2002 DARPA.)

The cell chemistry used in this application is the same as a standard PLI cell [25]. Initial trials at DARPA attempted to use various commercial PLI cells as the web of an "I" section beam. However, this proved unsuccessful as the only bonding areas around the edges of the cells is a thin band of encapsulation. The encapsulation is, as described in Section 2.2.4, only a thin layer of plastic/aluminium laminate and thus has virtually no structural capacity when loaded in this way. Instead, custom-built cells are manufactured directly on the upper wing surface. Thus, the structural properties of conventional PLI cells, of the same type as those that are commercially available, are used, albeit at a greater cost due to the need to custom build them. It is notable that cells based on commercial types have been used, as such cells have undergone feasibility tests for use in spacecraft [61].

Another recent development is the use of a fuel cell based multifunctional wing structure on the Hornet UAV [69]. In this case, the structure of the wing is reinforced by the metallic mesh that forms a part of the fuel cell electrode. The fuel cell technology, developed by Lynntech, Inc., offers excellent energy density (reportedly up to 400 $Whkg^{-1}$ is achievable). However, rather than carrying pressurised oxygen

and hydrogen, hydrogen is evolved from a solid material reacting with water stored on the aircraft, and oxygen is taken from the air flowing over the wing. This technology is thus less appropriate for use in space, where on-board oxygen storage would still be necessary.

2.4 Summary

2.4.1 PLI Batteries in Space

Lithium batteries, and especially PLI batteries, represent a great advance over the conventional technologies used in the space industry. As well as offering obvious and immediate improvement in energy density, lightweight prismatic PLI cells can use novel packaging methods to reduce the mass and effective volume of the power subsystem.

A potential disadvantage of PLI cells is the low cycle lives often quoted for them - the life of the cell described in Section 2.2.5 is quoted at 500 cycles (equivalent to roughly 1 month in LEO) before the capacity is reduced to 70% of initial. However, batteries used for terrestrial applications are, in most cases, subjected to deep discharges every cycle, which greatly increases degradation in performance. Ni-Cd batteries used in LEO are discharged to as little as 12% and no more than 25%, depending on the required lifetime (higher cycle life requires smaller DOD) [70].

The lithium-ion cells already in use in spacecraft are designed for similar applications to PLI cells, and have demonstrated quite acceptable cycling performance under spacecraft operating conditions. Whilst it is not certain whether this performance would also be achievable for PLI batteries, the large mass savings that would result justify some experimentation to investigate; as noted previously, qualification tests have already been completed to prove their suitability for spacecraft missions [61].

2.4.2 Common Disadvantages of Current MFS Power Systems

All of the MFS systems described in the previous pages share one common feature: they use cells manufactured specifically to be used as (or to integrate directly with) structural elements, rather than using readily available cells. Unless large production runs can be justified, this means manufacturing cells by hand. Long production runs are not a common feature of space missions and, given the need to tailor the structural and electrical properties of the MFS to the spacecraft's requirements, many units would be produced as one-offs. The need to manufacture electrochemical cells by hand presents two major obstacles to the implementation of a multifunctional powerstructure.

First is the issue of cost – manufacturing standard cells in large production runs is an automated process and results in cost per cell of the order of a few dollars per unit. On the other hand, manufacturing small numbers of cells is very costly, due to the large amount of touch labour involved. The cost of a hand built laminated cell might be thousands of dollars [24].

If the performance benefits of a multifunctional structure could be realised, then this increase in cost might be offset; however, the second major problem with cells manufactured in small numbers is that their electrochemical performance tends to suffer. With adequate facilities, expertise and good procedure, it is possible to manufacture cells whose average performance is comparable to that of mass-produced ones. The issue lies with consistency of performance rather than performance itself: cells produced in their thousands by an automated procedure will naturally be very closely matched in their attributes, whilst those assembled by hand will show more variability. This effectively reduces performance, as allowances must be made for this variability in design, and increases cost due to the need to invest more time in screening cells prior to use.

2.4.3 Commercial Cells for MFS

As described in Section 2.3.4 and [24], commercial PLI cells have been tested (and rejected) for use in certain structural applications. Similar materials have, however, been used in a custom-built cell for structural reinforcement [21-24]. These cell materials have relatively poor mechanical properties, and a commercially available cell, designed without such properties as an objective, will have yet worse structural performance. Ostensibly, therefore, using such cells in an MFS would appear to solve the problems of cost and electrical performance outlined above, whilst ultimately removing the benefits of an MFS due the resultant poor structural performance.

However, of the MFS systems previously described, not all actually employ the mechanical properties of the battery in the principal structure. In the case of LiBaCore, for example, the batteries are not expected to increase the stiffness of the honeycomb core; in fact, one would expect the material distributed over the sandwich panel to worsen its dynamic structural performance, as the additional mass would lower its natural frequencies. An increase in structural mass would result as a denser core or thicker facesheets would be required to compensate for this. Rather, the benefit arises from eliminating the structural packaging of the battery and removing its volume from the spacecraft. It should be noted the mass of a conventional battery would still need to be supported by another part of the structure if the cells were not located within the multifunctional panel, so the presence of the cells in one particular panel does not result in an increase in structural mass at the full system level.

It is not necessary, therefore, to make great use of the structural properties of the battery to take advantage of the performance of MFS. Rather, placing electrical energy storage within the structure allows the components of the battery that do not perform an electrical function to be removed, as well as reducing the total volume of the bus. It is then necessary to design the multifunctional structure in such a way that these modifications cause minimal deterioration in structural performance, for example by

placing the less structurally useful components in areas of the structure that are subjected to lowers stresses.

This concept could result in low-cost but also high performance technologies that would be of particular use for small satellites. Due to their high cost, aerospace-grade components are not usually an option for small satellite missions, and aerospace-grade multifunctional structures would be truly prohibitive; however, a simple structure made from commercial cells could be custom built quite cheaply, and would still provide performance superior to current designs. Given that such cells would not be as structurally useful as dedicated structural materials, it would be necessary to seek out a location in the structure that requires them to carry less load. The normal structural materials in such a location could then be replaced by batteries without causing an overall reduction in performance.

A well-designed spacecraft structure does not provide many candidate locations of this type, as any parts of an homogeneous structure that are not highly loaded would be removed to save mass. However, not all structural materials are intended to carry large loads: the core of a sandwich panel, for example is chosen for lightness rather than total stiffness or strength. The majority of the stress in such a panel is carried by the facesheets, while the core (usually a honeycomb of aluminium) transmits shear forces between them. Removing parts of the core and replacing them with batteries would be a simple way to produce a multifunctional structure. As long as the proportion of the core that is so replaced is relatively small, it is possible to take advantage of the higher stiffness of the batteries (if applicable) while minimising the impact of their added mass by choosing appropriate locations within the panel.

The remainder of this thesis shall assess the magnitude of mass savings that may be made through using a multifunctional power structure, to prove that employing an MFS is worthwhile from a systems engineering perspective. It will then go on to describe work to design a conceptual MFS using commercial PLI cells to replace the core of a honeycomb sandwich panel.

3 Potential Mass Savings from MFS

As has been discussed previously, the principal advantage of using a multifunctional powerstructure in a spacecraft is the reduction in mass, which in turn leads to a reduction in launching costs. Before going further, however, it is necessary to quantify these advantages, as far as is possible.

Precise data on the exact attributes of spacecraft and their batteries are limited; as such, a parametric approach was adopted to establish the importance of various aspects of the design of the spacecraft and its battery. A series of relevant performance parameters was defined and used to study how much mass could be saved, since, at the least, the range of these parameters can be established. This chapter shall present the magnitude of the mass savings available to typical classes of spacecraft, in terms of these parameters.

It should be noted that this method could be applied to any multifunctional power structure system, or indeed any alternative packing method for a spacecraft battery, so long as the appropriate ranges are set for the parameters. This chapter, however, limits the study to consider only the known or projected performance of an MFS based on commercial lithium cells.

3.1 Origins of Mass Savings

Using a multifunctional structure reduces the total mass of a spacecraft by two means. Firstly, eliminating the components of the battery that do not contribute to the battery's electrical function (principally the box, brackets and so on that comprise the enclosure), and potentially using the structural properties of the battery to replace part of the main structure, allows an amount of mass proportional to the original mass of the battery to be removed. Secondly, as the volume of the battery pack is removed from the bus, the structure itself may be made smaller as less internal volume is

required. This assumes that the size of the spacecraft is not fixed by some other constraint (for example, use of standardised structural components or an area requirement for body-mounted solar arrays) and that the battery cells can be distributed within the structure, without adding mass to it.

These benefits will necessarily be offset by the costs associated with designing a more integrated spacecraft, and the need for qualification of new technology. Calculating these costs is beyond the scope of this work, as they would vary enormously according to the nature of the spacecraft mission and the company designing it. However, it is both appropriate and relatively straightforward to calculate the magnitude of the available mass savings made through the employment of a multifunctional structure according to a series of easily defined spacecraft performance parameters, which this chapter shall demonstrate.

3.2 Spacecraft Parameters

Several important attributes affect the mass that may be saved using a multifunctional structure. These attributes shall be expressed as parameters in order to assess the effect of varying them. The parameters considered in this study are as follows:

Battery parasitic mass fraction (η_{para}): Defined as the ratio between the mass of the inert parts of the battery enclosure (M_{para}) and the total mass of the battery cells (M_{cells}), this parameter relates the mass of the active battery elements (i.e., the cells) to the mass of any inert components that support the battery. Since the principal aim of using an MFS is to eliminate this parasitic mass, it is important to ascertain how much mass may be saved by this means.

If the battery is redesigned, for example by using an MFS, the parasitic mass may be reduced, becoming zero if the battery is accommodated entirely by the primary structure with no secondary structure required. Further to this, if the structural

properties of the cells are used, it is possible to eliminate mass from the structure, which is represented by making this parameter negative.

$$\eta_{para} = \frac{M_{para}}{M_{cells}} \text{ where } M_{para} = M_{para,initial} - M_{para,removed} - M_{stru,removed} \quad (3\text{-}1)$$

Specific Energy Capacity (*SEC*$_{cell}$): This is a fundamental property of the type of cell chemistry used in the spacecraft, defined as the nominal energy capacity of a cell (its nominal voltage, V_{nom}, multiplied by its nominal capacity, C_{nom}, in Ah) divided by the mass of a bare cell (m_{cell}). This parameter is frequently used in the literature to compare different battery types' performance.

Recent advances in battery technology mean that this number varies enormously, from 40 Whkg^{-1} for the older nickel-cadmium cells that are still in use, to well over 200 Whkg^{-1} for the latest lithium-based chemistry. Variation of this parameter allows a comparison of the mass saving achieved by using a different type of cell and that achieved by using a multifunctional power structure. As noted in (3-2), this is also the ratio between the total energy capacity of the battery and the total mass of the cells that comprise it.

$$SEC_{cell} = \frac{C_{nom}V_{nom}}{m_{cell}} = \frac{E_{batt}}{M_{cells}} \quad (3\text{-}2)$$

Specific Energy Requirement (*SER*$_{sat}$): The SER of a spacecraft is defined as the total requirement for energy storage from its battery, E_{bat}, at beginning-of-life (BOL) divided by the launch mass of the spacecraft, M_{sat}. Relating this parameter to SEC_{cell} allows the mass of the battery to be calculated as a function of the mass of the spacecraft, and hence, using η_{para}, the saving in parasitic mass may be calculated.

$$SER_{sat} = \frac{E_{bat}}{M_{sat}} \tag{3-3}$$

Structural mass density (δ_{vol}): This parameter allows the volume reduction achieved by removing the battery from the spacecraft bus to be translated into a saving in structural mass. It is defined as the mass of the structure divided by V_{bus}, the volume of the main body of the craft (in stowed configuration if appropriate).

$$\delta_{vol} = \frac{M_{stru}}{V_{bus}} \tag{3-4}$$

Packing efficiency (η_{pack}): This quantity represents the fact that the removal of the battery effectively eliminates more volume than that of the cells themselves. In addition to the inert elements of the enclosure itself, a spacecraft configuration typically wastes a large amount of internal volume, due to the need for harness clearance, balancing, safety margins and the fact that it is virtually impossible to fit a series of items with mounting feet and irregular protuberances into a single space without leaving gaps. The removal of the battery, therefore, will also eliminate a corresponding amount of this wasted volume, and the η_{pack} parameter relates the volume of the cells, V_{cells}, to the proportion of the spacecraft's internal volume that is effectively occupied by the battery, V_{cells}.

$$\eta_{pack} = \frac{V_{cells}}{V_{batt}} \tag{3-5}$$

3.2.1 Parameter Values

Table 3-1 shows the ranges of values used for the parameters in the study.

Parameter	Units	Limits	
		Lower	Upper
η_{para}	None	-0.05	0.25
SEC_{cell}	$Whkg^{-1}$	120	220
SER_{sat}	$Whkg^{-1}$	<0.5	>5
δ_{vol}	kgm^{-3}	0	350
η_{pack}	None	0.5 throughout – not varied	

Table 3-1 - Parameter values

The range for η_{para} is based on historical data from previous spacecraft missions where relevant information was available, such as the CFESat mission and batteries manufactured by AEA for various spacecraft. The values of this parameter for conventional battery enclosures generally vary from 0.15 to 0.25, and so 0.25 is chosen as the highest value. The lower limit is a theoretical value for an ideal multifunctional power structure, where part of the structure is replaced by the battery, in addition to the parasitic mass itself being removed. Thus, the mass of the primary structure itself is reduced by the presence of the battery, effectively making the parasitic mass associated with the battery negative. A value of -0.05 is selected as a minimum since this would represent typical battery cells (mass density of around 2000 kgm^{-3}) replacing aluminium honeycomb (mass density of around 100 kgm^{-3}).

The minimum value of SEC_{cell} is based on data for cells currently in use in space applications: the Sony 18650 lithium-ion cell used by AEA for spacecraft battery packs, with an SEC of 129 $Whkg^{-1}$ [36]. Since this type of cell is now quite commonly used in space applications, whilst being part of the new generation of lithium batteries, it is used as the baseline cell. The upper limit is based on the performance of the latest PLI cells (such as the Varta PoLiFlex [34]).

The range of SER_{sat} is based once more on historical data. There is no real lower limit on this quantity; in the case of geostationary observation satellites, for example, the few eclipses and low eclipse power requirement mean that SER may be less than 0.5

$Whkg^{-1}$ (for example, Meteosat 5 has a battery capacity of 270 Wh, and a launch mass of 681 kg – giving an SER of less than 0.4 $Whkg^{-1}$). Spacecraft that operate in LEO require larger battery capacities in order to account for capacity fade due to repeated cycling, and hence have a higher SER for a given eclipse power requirement. However, most LEO spacecraft are observational, and so have comparatively small power requirements in eclipse (for example, ERS-1 has a 2650 Wh battery and a launch mass of 2150 kg – leading to an SER of 1.2 $Whkg^{-1}$).

The highest SER occurs for spacecraft that have large power requirements that continue during eclipse – most notably geostationary communication satellites. Such craft have lifetimes of up to 15 years, which limits their batteries' DOD to 40-60%, in spite of the relative infrequency of eclipses in GEO, and extremely high power requirements. GEO communication satellites have SER values of as much as 5 $Whkg^{-1}$. Satellites based on the EuroStar 3000 bus are a good example of this class, weighing around 5000 kg with a battery capacity of over 18 kWh – leading to an SER of 3.75 $Whkg^{-1}$. Navigation satellites such as those used in the GPS or Galileo constellations also have particularly high power requirements, which continue in eclipse, leading to SER values as high as those of communications satellites: the Giove-B demonstrator for Galileo has an SER of 4.8 $Whkg^{-1}$ (415kg, 2000 Wh).

δ_{vol} is also based on data from previous spacecraft missions. For large spacecraft (1-2 tonnes and over), this term is very small – typically less than 30 kgm^{-3} (Intelsat IV, for example, had a launch mass of 1.9 tonnes, and a δ_{vol} of 25.7 kgm^{-3}). However, as spacecraft mass decreases, δ_{vol} increases sharply, exceeding 150 kgm^{-3} for spacecraft under 100 kg. An example is this range is CFESat, with a launch mass of 157 kg and a δ_{vol} of 146 kgm^{-3}. For very small spacecraft (of the nanosat or "cubesat" type, with masses down to around 10 kg), the parameter can even exceed 500 kgm^{-3}. This study shall consider structural mass densities up to 300 kgm^{-3}, where the highest value equates to spacecraft with masses of the order of 50 kg. The baseline value is zero; whilst a structure with a density of zero is not, of course, possible, this is

representative of situations where the volume of the spacecraft is fixed, or the density is so low that no significant savings could be made.

η_{pack} is not easily quantified, as it is highly dependent on the geometry of individual cells (cylindrical cells being less efficient in this regard, for example), the design of the battery pack and the configuration of the spacecraft. Since it acts, to all intents and purposes, as a coefficient to the δ_{vol} term, it is not varied. A value of 0.5 is used throughout the study; it seems logical to assume that the value would decrease as the battery becomes volumetrically larger in comparison to the spacecraft

3.2.2 Methodology

The principle of this study is to calculate the mass savings that may be achieved for various values of the parameters listed in Table 3-1. To calculate a saving in mass, a baseline must be set; the effect of modifying the parameters may then be established by comparing the "new" design to this baseline. The selection of a value for SER_{sat} is not critical since, as shall be seen, the mass savings all vary linearly with this parameter; the baseline for δ_{vol} is zero, i.e., a spacecraft whose volume cannot be reduced. The values of SEC_{cell} and η_{para} pertain only to the power subsystem, and those chosen represent the most typical (and heaviest) battery designs in use (120 $Whkg^{-1}$ and 0.25 respectively). This baseline is independent of the size of the spacecraft.

The mass saved purely by using a different cell type, for values of SEC_{cell} up to 220 $Whkg^{-1}$, shall be plotted, as shall the mass saving achievable through using a multifunctional structure – the saving due to both parasitic mass elimination and bus volume reduction being indicated. All mass savings shall be calculated as a function of the total spacecraft mass at launch. The subscript "0" indicates the current baseline value for the parameter in question throughout. For subsequent calculations and plots, different baseline values will be shown (for example, the effect of a baseline design using higher performance cells).

The reduction in battery mass, relative to total spacecraft mass, achieved through using an alternative cell chemistry (such as PLI in place of older cylindrical Li-ion) in a conventional battery pack is calculated as follows. Firstly, the mass of the battery cells relative to the total mass is calculated as a function of SER and SEC.

$$\frac{SER_{sat}}{SEC_{cell}} = \frac{E_{sat}/M_{sat}}{E_{batt}/M_{cells}} = \frac{M_{cells}E_{sat}}{M_{sat}E_{sat}} = \frac{M_{cells}}{M_{sat}} \tag{3-6}$$

The parasitic mass is the mass of the cells multiplied by η_{para}, and hence the total battery mass, relative to the launch mass of the spacecraft, is given by:

$$\frac{M_{batt}}{M_{sat}} = \frac{SER_{sat}}{SEC_{cell}}\left(1+\eta_{para}\right) \tag{3-7}$$

If a different battery type is used, the SEC of the chosen cells will be different and, thus, there will be a change in the mass of the battery. Keeping the design of the battery enclosure and energy requirement fixed (such that η_{para} and SER do not vary), the reduction in mass is:

$$\begin{aligned}\frac{\Delta M_{batt}}{M_{sat}} &= \left(\frac{SER_{sat}}{SEC_{cell,0}}\right)\left(1+\eta_{para}\right) - \left(\frac{SER_{sat}}{SEC_{cell}}\right)\left(1+\eta_{para}\right) \\ &= \left(\frac{SER_{sat}}{SEC_{cell,0}} - \frac{SER_{sat}}{SEC_{cell}}\right)\left(1+\eta_{para}\right)\end{aligned} \tag{3-8}$$

A lighter battery pack will also have a smaller volume, and hence the structural mass may be reduced. Since the battery's mass is calculated in terms of the spacecraft mass, this must be converted into a volume using the mass density of the cell, ρ_{cell}. The value of ρ_{cell} varies slightly for different cell types, and so to take account of this, the relationship within the range studied herein is approximated as in (3-9). This is an empirical relationship based on the specifications of 250 lithium cell models (cylindrical and PLI) produced by Sanyo, IBT and Varta.

$$\rho_{cell} = 3400 - 7.5 \times SEC_{cell} \tag{3-9}$$

From this, the volume of structure required to accommodate the battery is calculated, noting that the volume required is modified by η_{pack}:

$$\frac{V_{batt}}{M_{sat}} = \frac{SER_{sat}}{SEC_{cell}} \left(\frac{1}{\rho_{cell} \eta_{pack}} \right) \tag{3-10}$$

The mass of structure required by the battery is then this volume multiplied by the structural mass density:

$$\frac{M_{stru,batt}}{M_{sat}} = \frac{SER_{sat}}{SEC_{cell}} \left(\frac{\delta_{vol}}{\rho_{cell} \eta_{pack}} \right) \tag{3-11}$$

The total mass saving achieved purely through changing SEC_{cell} is thus:

$$\frac{\Delta M_{SEC}}{M_{sat}} = \frac{SER_{sat}}{SEC_{cell,0}} \left(1 + \eta_{para} + \frac{\delta_{vol}}{\rho_{cell,0} \eta_{pack}} \right) - \frac{SER_{sat}}{SEC_{cell}} \left(1 + \eta_{para} + \frac{\delta_{vol}}{\rho_{cell} \eta_{pack}} \right) \tag{3-12}$$

If the battery pack is redesigned or a multifunctional structure is used, additional mass is saved through the reduction of the battery's parasitic mass as follows:

$$\begin{aligned} \frac{\Delta M_{para}}{M_{sat}} &= \frac{SER_{sat}}{SEC_{cell}} \eta_{para,0} - \frac{SER_{sat}}{SEC_{cell}} \eta_{para} \\ \frac{\Delta M_{para}}{M_{sat}} &= \frac{SER_{sat}}{SEC_{cell}} \left(\eta_{para,0} - \eta_{para} \right) \end{aligned} \tag{3-13}$$

Finally, the mass saving which results from removing the battery, and hence its volume, from the bus is calculated. It is assumed in this case that the entire volume requirement is removed, and so, referring to (3-10), the mass saving is given by:

$$\frac{\Delta M_{vol}}{M_{sat}} = \frac{SER_{sat}}{SEC_{cell}} \frac{\delta_{vol}}{\rho_{cell}\eta_{pack}} \tag{3-14}$$

Figure 3-1 shows a chart of the mass savings for a spacecraft using the baseline quantities defined at the start of this section, with the exception that a high value of δ_{vol} is used (300 kgm^{-3}). The mass saved by changing the cell chemistry (ΔM_{SEC}), eliminating parasitic mass and harnessing the structural properties of the cells (ΔM_{para}) and reducing structural volume (ΔM_{vol}) at each value of SEC_{cell} are indicated separately. A dashed line divides the ΔM_{SEC} saving into two areas: the lower area indicates mass saved by reducing the mass of the cells themselves, whilst the smaller upper area indicates the mass saved by reducing the volume of the bus.

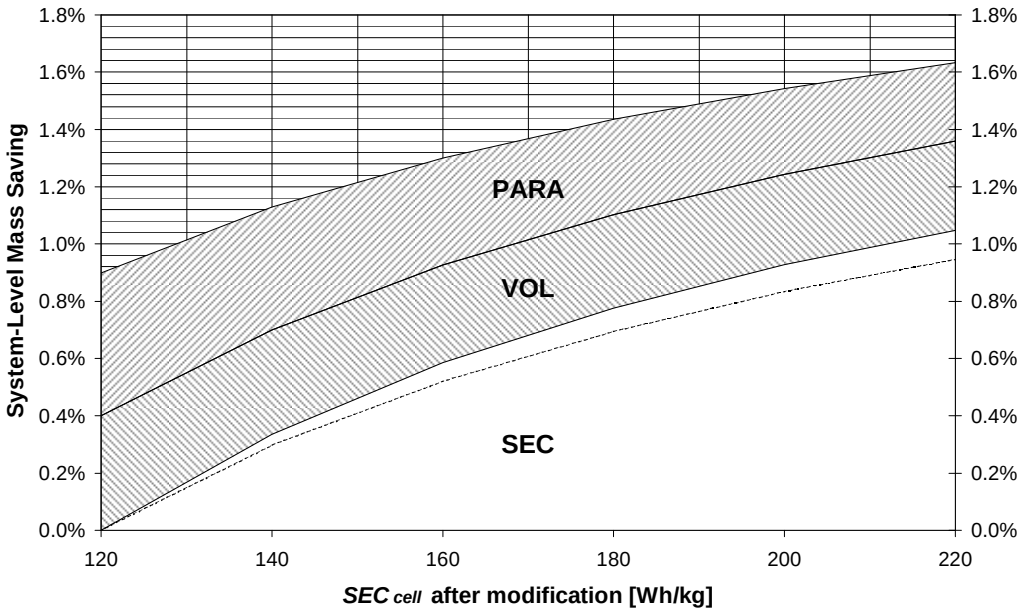

Figure 3-1 - Example graph showing mass saved by increasing SEC and adopting an MFS

This graph shows the maximum savings that may be made by replacing the conventional battery (using early Li-ion cells and a typical enclosure) in a spacecraft with the attributes defined previously (an SER of 2 Whkg^{-1} and a δ_{vol} of 300 kgm^{-3}). In this case, the maximum possible saving, within the limits set for the study, is just over 1.6% of total mass, by both using an MFS and a state-of-the-art lithium cell.

This chart may also be used to assess the options available to achieve a desired mass reduction for this particular spacecraft. For example, supposing a requirement for a mass saving of 0.8%, the following options would be available to satisfy it:

- One could simply choose an improved cell, with an SER in excess of 180 $Whkg^{-1}$.
- If the cell type was fixed, then a purely multifunctional approach could be taken (assuming that the existing cells were suited to this application). Fully eliminating the parasitic mass and volume of the battery would meet the requirement.
- One could redesign the battery to use a partial MFS (eliminating no parasitic mass but all of the battery's volume or vice-versa) and a cell with an SER of 150 $Whkg^{-1}$.

3.3 Analysis

3.3.1 Variation of Specific Energy Requirement

Referring to (3-12), (3-13) and (3-14), it is evident by inspection that all three mass saving terms are directly proportional to SER_{sat}. Hence, holding all other parameters constant, the size of the mass saving varies linearly with SER_{sat}, meaning that a spacecraft with a larger energy storage requirement benefits from a larger mass saving through use of an MFS. Figure 3-2 shows how much mass may be saved for different values of SER_{sat}. The upper area represents the absolute maximum value of the mass saving that may be made by modifying the secondary power system: increasing the SEC from 120 to 220 $Whkg^{-1}$ and eliminating the parasitic mass (i.e., modifying η_{para} from 0.25 to -0.05) and volume of the battery pack (the area shows the variation of δ_{vol} from 0 to 350 $Whkg^{-1}$). The heavy line indicates the saving made by increasing the SEC but using a conventional battery pack. The lower area indicates the saving made by using a multifunctional structure alone (fixing SEC to 120 $Whkg^{-1}$).

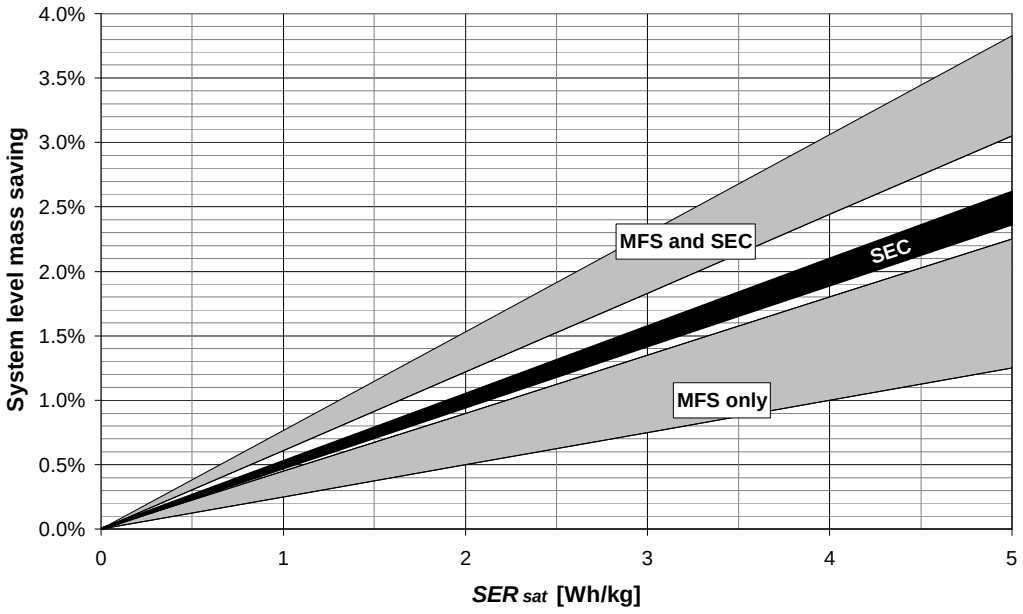

Figure 3-2 - Maximum achievable mass savings vs. SER

As an overview, this chart indicates that:

- The savings made by using a multifunctional structure are roughly equivalent to changing the cell type from conventional cylindrical lithium-ion cells to a state-of-the-art PLI cell type, for high values of δ_{vol}.

- For spacecraft with an SER of 1.5 or less, the maximum possible mass saving is around 1% or less, which is probably not sufficient to warrant the investment that would be required to achieve this saving. Such an energy requirement is consistent with spacecraft whose power requirements are either not that high (such as most types of Earth observation craft) or do not continue in eclipse (for example, spacecraft whose peak power demands occur during a data download that is conducted in sunlight).

- For spacecraft with an SER of 4 $Whkg^{-1}$ or higher, even the minimum mass saving is over 1%. This value is consistent with spacecraft whose power demands are large and, most importantly, continuous: this is most characteristic of communication

and navigation satellites, which are required to transmit high-power signals without interruption.

Since the variation in mass saving with SER is linear, from here onwards it shall be fixed at a value of 2 $Whkg^{-1}$, which is representative of a less power-hungry spacecraft, such as an Earth-observing satellite. However, the objective of the subsequent sections is to compare the relative importance of different methods of mass reduction, and so, from here on, the absolute values are of less relevance.

3.3.2 Mass Savings from Cell Chemistry

Normally, when seeking to reduce the mass of a battery (assuming that the energy storage requirement is fixed) the simplest method is to seek a cell chemistry with a higher specific energy capacity. Assuming that commercially available cells are to be used, the cell chemistry is limited to an SEC of around 220 $Whkg^{-1}$.

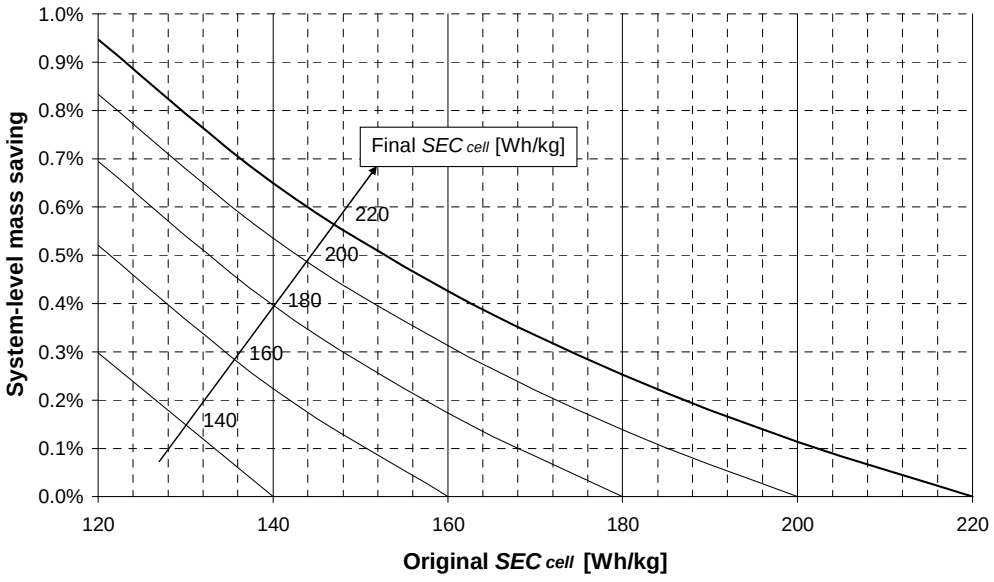

Figure 3-3 - Available mass saving from chemistry change

Figure 3-3 shows how much mass may be saved by changing the cell type. From this chart, it may be concluded that:

- Increasing SEC results in diminishing returns – the reduction in mass made by increasing SEC by 40 $Whkg^{-1}$ is more than half that made by increasing SEC by 100 $Whkg^{-1}$.
- As would be expected, if the cell used already has one of the highest available SECs, then little to no mass may be saved by changing the cell type.

3.3.3 Mass Savings from Parasitic Mass Removal

This section shall compare the savings made through the changing cell types with those made by eliminating the parasitic mass of the battery enclosure. This is representative of situations where δ_{vol} takes a small value (i.e., for spacecraft with masses of around 1 tonne or over, where δ_{vol} is generally around 25 kgm^{-3}), or if the spacecraft volume cannot be reduced, meaning that the structural volume terms in equations (3-12) and (3-14) may be neglected.

Figure 3-4 shows the system level mass savings available through eliminating the parasitic mass of the battery pack (with the baseline η_{para} assumed to be 0.25) and compares this with the mass reduction achievable through increasing SEC_{cell} from 120 to the maximum value 220 $Whkg^{-1}$.

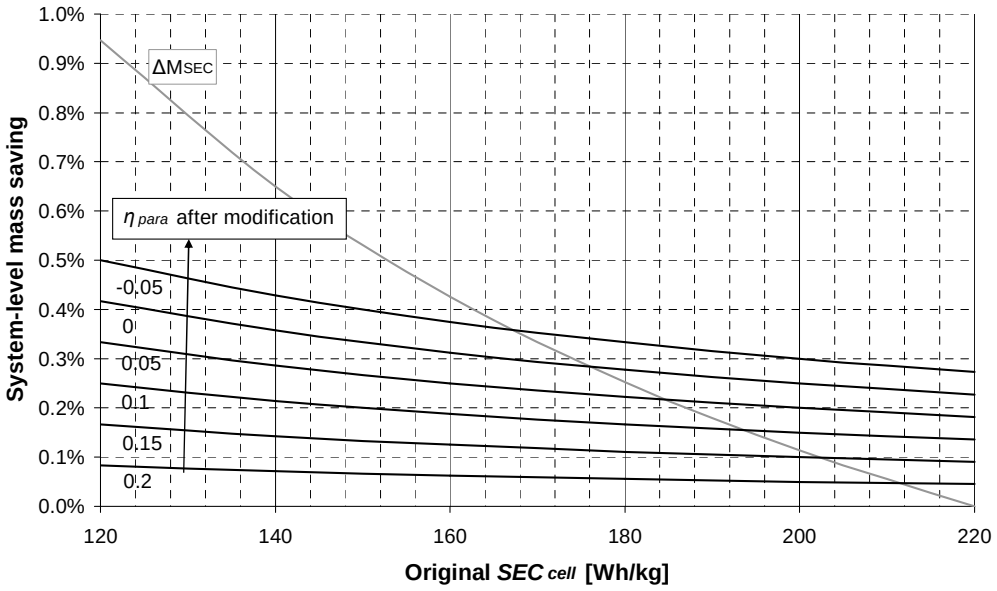

Figure 3-4 - Comparison of ΔM_{SEC} with ΔM_{para} for various values of η_{para}

It is notable that, where the initial SEC_{cell} is above 155 Whkg^{-1}, the saving that can be made by eliminating parasitic mass exceeds that deriving from changing the cell type (assuming once more that 220 Whkg^{-1} is the limit to the parameter). Even below this value, the saving made by eliminating parasitic mass is significant – 1.25% for a spacecraft with an SER of 5 Whkg^{-1}.

3.3.4 Mass Savings from Volume Reduction

For spacecraft with a high δ_{vol}, the third mass reduction element - that based on structural volume reduction - must be considered. The ΔM_{vol} term is highly variable according to the value of the δ_{vol} parameter, and varies slightly with the SEC_{cell} parameter. Figure 3-5 shows how much mass may be saved by eliminating the volume of the battery compared to the savings available from modifying SEC_{cell} (once more, from 120 to 220 Whkg^{-1}) and eliminating parasitic mass (baseline η_{para} of 0.25, final η_{para} of -0.05), for various values of δ_{vol}.

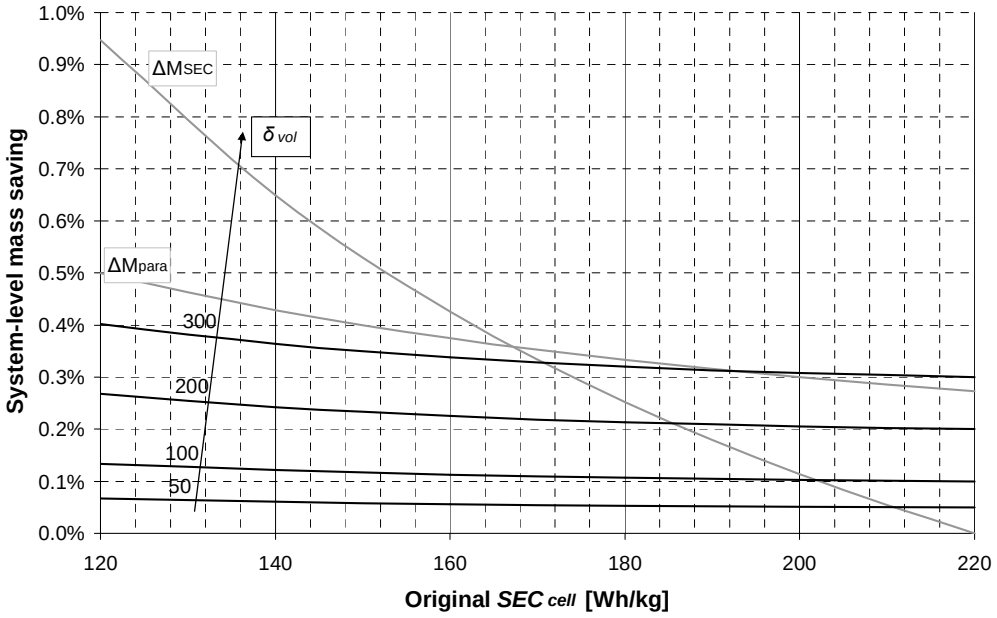

Figure 3-5 - Mass savings from volume reduction vs. SEC_{cell}, for various values of δ_{vol}

The highest value of δ_{vol} results in a similar mass saving to that achieved from eliminating parasitic mass and, when SEC_{cell} exceeds around 160 Whkg^{-1}, the potential saving exceeds that which may be achieved by changing the cell type.

3.3.5 Combined Savings

Figure 3-6 shows the combination of the mass savings that arise from parasitic mass elimination (baseline η_{para} of 0.25, final η_{para} of -0.05) and volume reduction, compared to the available mass saving from changing SEC_{cell}. For medium values of δ_{vol} (around 200 kgm^{-3}), the saving achievable through using an MFS exceeds the available mass saving from changing SEC throughout.

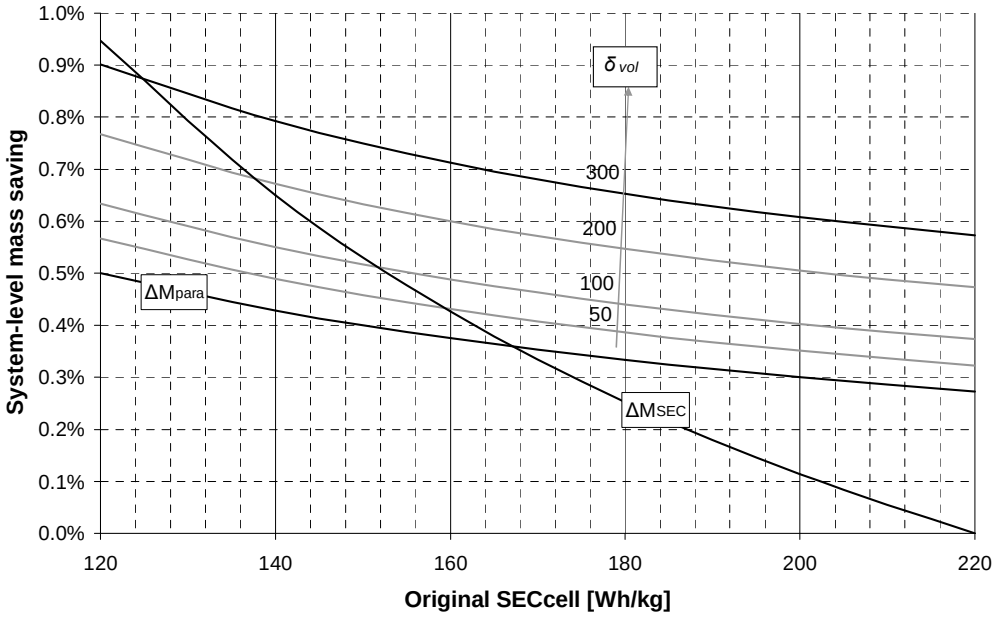

Figure 3-6 - combined savings from parasitic mass and volume reduction vs. SEC

3.4 Summary of Results

Three particular characteristics identify spacecraft that may benefit from the use of a multifunctional power structure: high energy storage requirement, high structural mass per unit volume and high cell specific energy. It is a natural conclusion that a spacecraft with a higher energy requirement will have a heavier battery, and hence will benefit from reduction in battery mass by any means. This correlates to spacecraft that have high power requirements in eclipse and/or very long lifetime requirements (a longer lifetime means that less of the battery's capacity is actually used, to allow for capacity fade).

For minisatellites (spacecraft with a mass below around 500 kg), the structural mass density becomes so high that the amount of mass that may be saved by reducing volume increases dramatically. In addition, if the design of the battery or its place in the overall spacecraft configuration is volumetrically inefficient (i.e., if η_{pack} is particularly low), removing the battery eliminates a significantly larger volume of

structure. In some cases, the saving in structural mass may exceed the saving made by eliminating the parasitic mass of the battery, and hence significant savings in mass may be made even if the MFS is not structurally optimised, due to the large savings from volume reduction.

Finally, where a spacecraft already employs a high SEC_{cell} cell type, the multifunctional structure becomes more useful. Such a battery is comparatively light due to its high performance, and thus the system-level mass saving through using a multifunctional structure is less than for a battery that uses a lower performance cell. However, if a mass reduction is required, there is less or no possibility to save mass by increasing the already high SEC_{cell}, and so using a multifunctional structure is the only way to reduce the secondary power system's mass.

4 Suitability of PLI Cells

This chapter assesses the feasibility of the powerstructure concept from the point of view of the suitability of the PLI cells for use in an MFS. Firstly, a suitable COTS cell product was selected for investigation. Two aspects of the properties of cells from this range were then assessed experimentally.

Firstly, a cell was subjected to random vibrations, without structural loads that would cause macroscopic deformation, to ensure that such cells are capable of surviving the mechanical environment of launch. This is a critical aspect of the testing, as a cell mounted within the structure would be subjected to the full force of launch vibrations, regardless of the particular structural loading to which it would be subjected.

Secondly, a series of experiments were carried out to determine the shear modulus of the cells. Since the MFS concept proposes to use these cells as a component of the core of a sandwich panel, this attribute largely determines how adopting a multifunctional approach will affect the overall mechanical performance of such a structure.

4.1 Battery Testing and Characterisation: Background

To test a cell's ability to survive mechanical vibration it is necessary to describe the testing used to assess its electrical performance. This section will describe the form that these tests commonly take.

In order to be qualified for use in a space application, batteries are subjected to testing to demonstrate that they will be capable of performing adequately. This testing reflects both the conditions in the space environment and all of the requirements of the spacecraft mission. Firstly, batteries must undergo basic electrical characterisation to establish relationships between discharge rate, depth of discharge, cycle life and voltage (see, for example, [71-73]). Then, they are subjected to further testing to

observe the way their projected environment will affect their performance, as in [39,41,44]. This testing must cover all aspects of the in-service conditions. This section will describe the methods used to perform these tests.

4.1.1 Characterisation

Characterisation is done on any cell type, whether for use in space or otherwise. Characterisation takes the form of charging and discharging many examples of the cell repeatedly under varying temperatures, discharge rates and depths of discharge.

Aims of Characterisation Tests

The results of this testing are charts that indicate the performance of a cell under different operating conditions. The two principal chart types plot voltage against state of charge (SOC), the charge level of the battery (where 1 is fully charged and 0 is the defined cut off voltage), and capacity against cycle number. The shape of the first graph (shown in Figure 4-1) varies according to temperature and discharge rate, and as such, separate plots are needed to indicate the differences. The second graph (Figure 4-2) is also affected by various factors, and so it is necessary to include individual plots for various depths of discharge and discharge rates (see [29,35,71], for example). Note that Figure 4-1 and Figure 4-2 do not pertain to a particular model of battery; their purpose is simply to show the basic shapes of graphs one would expect to see, and indicate how they vary under different conditions.

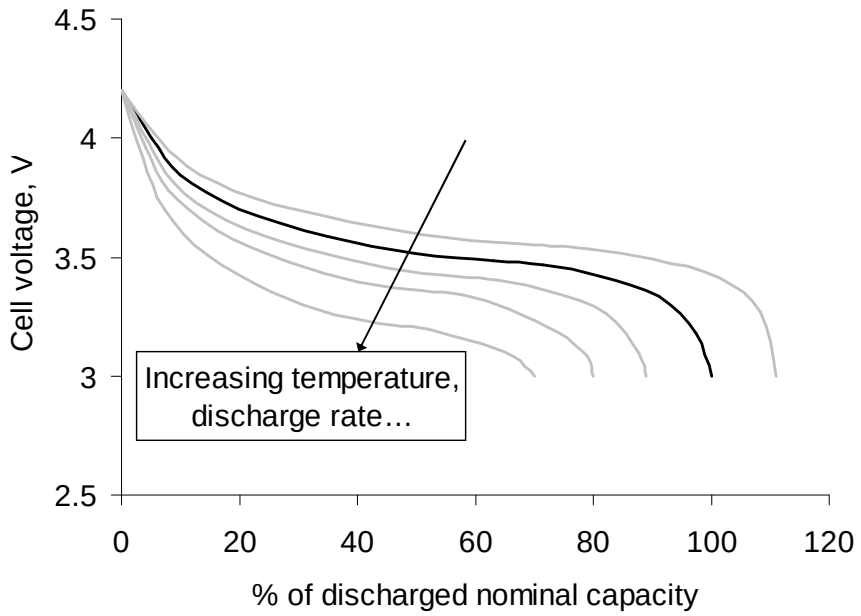

Figure 4-1 - Illustrative graph of state of charge vs. voltage, with nominal curve in black

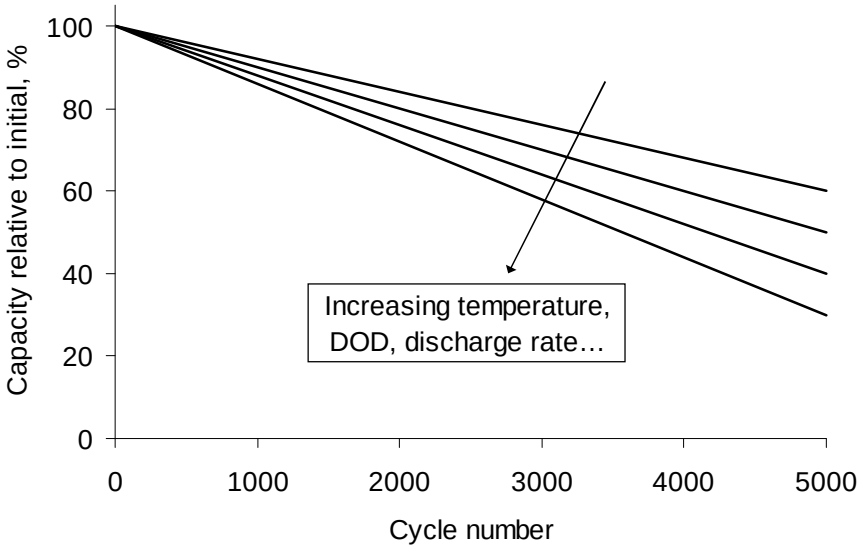

Figure 4-2 - Illustrative graph of capacity vs. cycle number

These graphs show how well suited a particular battery type is to a given application. The discharge curve, for example, must be reasonably flat for use with electronic components, many of which require a fairly uniform voltage for their operation; if the

discharge curve varies greatly with temperature, this will have implications for the thermal control of the spacecraft. The cycle graph is particularly important for space applications, as batteries used on spacecraft (especially in LEO) must be able to undergo hundreds or thousands of charge/discharge cycles during their operational life.

Characterisation Testing Methods

In order to characterise a cell as described above, many samples are tested over hundreds or thousands of discharge cycles and under varying discharge conditions. Full characterisation is beyond the scope of this work, and the performance of the cells under test is already known to an adequate degree of precision; it is only necessary to establish whether there are significant changes in the performance of the cell. As such, a less accurate but simpler system of testing may be used for this work than the methods used in industry. Examples of industrial cell characterisation methods may be found in [51,52,74] if more details are required, but a summary is given below.

Two principles guide industrial battery testing: repeatability and complete measurement. As stated, each cell will be tested over several hundred cycles. Each of these cycles must be, as far as possible, identical to ensure that any change in the cell's behaviour between cycles is attributable to its chemistry and not to variations in the environment or charge/discharge regime. As such, these factors must be carefully controlled. Since few environmental factors aside from temperature have large effects on cell performance, in reality environmental control entails controlling the temperature to which the cell is exposed very precisely. While under test, cells are typically placed in a temperature-controlled cabinet.

A computerised battery-testing device is used to charge and discharge the cells, and to log the current, voltage and temperature of the cell (which will rise above ambient during charge or discharge). The testing system provides the dual function of ensuring

that the test is precisely repeated, by maintaining a consistent charge/discharge regime, and measuring the attributes of the cell throughout testing.

The following parameters must be kept constant to ensure that the cell's electrical test regime is consistent:

- Charge current (the current at which the cell is charged during the constant current phase of the charging process).
- Taper voltage (the voltage at which the charging process changes from constant current to constant voltage).
- Cut-off current (the current level at which the charging process stops).
- Recovery period between the end of charging and the start of the subsequent discharge.
- Discharge current/discharge circuit resistance (the rate at which the battery is discharged. This is variable during the course of each test in the second case, but kept consistent between tests).
- Depth of discharge.
- Recovery period between the end of discharging and the start of the subsequent charge.

During the charging and discharging process, the current and voltage are logged. However, the charge or discharge is interrupted periodically, in order to measure the internal resistance of the cell. Typically, the current is stopped and the cell voltage is allowed to stabilise fully before the current is re-applied. This allows the full details of the voltage recovery, and thus of the internal resistance, to be determined (the behaviour of the cell's internal resistance is discussed in Section 4.2.3). In [71], a method is presented where a shorter pause is used, and a curve-fitting system allows the detailed performance to be extrapolated. If the cell is discharged to a fixed DOD

significantly less than 100%, occasional deep cycles may be conducted to assess changes in the total capacity of the cell.

These data allow a profile of the variation of voltage and internal resistance against SOC to be produced. In addition, measurement of the capacity allows the relationship between various performance parameters and cycle number to be determined. Another measure of the cell's performance that may be extracted from the cycling data is the charging efficiency, namely the ratio between the amount of energy that is passed into the cell during charging and the amount that is extracted during discharge.

These experiments are carried out for many cells, over hundreds of cycles and under various conditions, in order to provide details of the cell's behaviour under all expected circumstances.

4.1.2 Spacecraft Battery Testing

In order to qualify a cell for use in outer space, additional testing is required. A cell that has been characterised and found to have acceptable performance on Earth is not guaranteed to perform well in a spacecraft application, and commercial cells are unlikely to have been subjected to appropriate testing. Whilst actually performing all of these tests is beyond the scope of this work, it is relevant to consider what the selected cells would, ultimately, be subjected to.

Four additional areas must be considered when testing a cell for use in space. Firstly, the cell must be able to operate when under vacuum and so cycling must be carried out under vacuum conditions. This will involve cycling the cell normally (as described in Section 4.1.1) in a vacuum chamber. Secondly, temperature on a spacecraft has the potential to vary much more than temperature on Earth, and thus the cell's performance at extremes of hot and cold must be investigated. Again, this testing is broadly similar to standard characterisation testing, with more extended

temperature ranges. Thirdly, the cell will be subjected to radiation in the space environment, and so it must be exposed to comparable particle and electromagnetic radiation, being tested electrically before and after, to ensure that it will be unaffected by this environment. Finally, the cell must be subjected to a mechanical environment (mainly random vibration) representative of a spacecraft launch. If practicable, these tests are carried out in conjunction to produce a more representative testing scheme.

In addition to these specific space environment factors, it is usually necessary to repeat characterisation tests to better investigate the performance of cells in a space mission. In particular, it is not normal for terrestrial testing to cover as many charge/discharge cycles as are necessary in a spacecraft application; also, many manufacturers of spacecraft batteries prefer to perform their own tests on cells to confirm the manufacturers' data.

4.2 Effect of Vibration on Electrical Performance

PLI cells have been subjected to testing to qualify them for use in space by other authors [61], and it is assumed for the moment that the positive results of this testing can be applied to all similar cells. The testing described in [61] included a vibration test; however, there are two reasons for performing separate vibration tests on the chosen cell. Firstly, the cell may be subjected to a harsher uniform acceleration vibration environment (that is, more intense acceleration without any external macroscopic deformations) due to its location in the structure, and this acceleration may result in electrical damage. If this occurs, the reduction in performance may be greater than that incurred by using a conventional battery enclosure with damping, for example. In addition, the cells would, at some point require testing to assess the effect of loading them as a structural element. In the case of dynamic testing, it would be necessary to distinguish between the effects of the uniform acceleration of the environment and the deformation (bending, compression or shear) of the cell that results from the response of the structure. If the cell is damaged by loading that results

in macroscopic deformation, but not by uniform acceleration, then it may still be of use in spacecraft; on the other hand, if the cell is damaged when subjected to uniform acceleration only, it could not be used at all.

4.2.1 Cell Selection

This section will present a selection of commercial plastic lithium ion cells and describe the advantages and disadvantages of each type for use in the multifunctional structure application, and for the testing that shall be undertaken in this chapter. The most appropriate cell will be selected based on appropriate criteria.

Relevant Specifications

At the time of selection, the design of the MFS was not fixed. As such, it was considered that the cells could be stacked with honeycomb core, or even placed in a facesheet or a conventional structural panel, and thus that a thinner cell would be a better candidate.

The other important parameter was, and is, specific energy capacity. It is essential that the battery stores as much energy per unit mass as possible; otherwise, the higher mass of the battery will offset savings made through using the MFS.

Available Cells

Table 4-1 shows a selection of cells that were commercially available at the time of selection and of potential use in this application, along with their specifications. Cells with a thickness greater than 4 mm were excluded from the selection in order to narrow the field, and where several cells were part of the same product line with similar dimensions, the model with superior performance was included.

Manufacturer	Model	Capacity, mAh	Mass, g	SEC, $Whkg^{-1}$	Thickness, mm
IBT	E383562	720	16.0	167	3.8
Varta	PLF 383562	675	15.0	167	3.8
IBT	E383450	585	13.0	167	3.8
Varta	PLF 263441	270	6.0	167	2.6
Varta	PLF 283562	482	11.0	162	2.8
Sanyo	UPF363562	513	13.5	141	3.6
Kokam	SLPB104330	43	1.7	94	0.8
Flexion	F482303V002	14	0.6	59	0.4

Table 4-1 - PLI Cell Performance Comparison

The cells are ranked according to their specific energy capacity. In the case of the Varta, IBT and Sanyo cells, there is comparatively little variation in this parameter, whilst the Kokam and Flexion cells perform significantly less well. These cells are, nevertheless, included for comparison, as they are notably thinner than the other subjects.

Selected Cells

The Kokam and Flexion cells are the only types that are sufficiently thin to be used within a plain panel. However, of these two, the Kokam cell would still be too thick to be of real use, as the cell would have structural properties notably worse than the surrounding material, and would probably make up more than half of the thickness of the panel. The Flexion cell, while thin enough to be included unobtrusively, has a specific energy much lower than the other cells. As such, these two cells were discounted.

Of the other cells, that which provides both the best specific energy and lowest thickness is the Varta PLF 263441 (PoLiFlex) cell [33], and as such, this cell was chosen for initial studies. The PoLiFlex range continues to demonstrate excellent

performance and cells from this range have been used for testing throughout the project.

4.2.2 Electro-Mechanical Test Procedure

Overview

The tested cell was subjected to random vibrations simulating a spacecraft launch. Its electrical performance was measured before and after the vibration test by discharging the cell through a load whilst logging the accumulated charge flowing through the battery, and its terminal voltage.

In order to distinguish between the natural loss in performance due to cycling and damage caused by vibrations, the cell was subjected to six vibration tests and cycled twice between each. Thus, a larger loss in performance after a vibrated cycle than an unvibrated cycle means that the difference is attributable to the effect of the vibration.

Electrical Testing

The cell was discharged through a load that consisted of an LED and resistor, resulting in a discharge of around 100 mAh or *C*/3. The cell was discharged to 25% DOD, current and voltage being logged throughout. The discharge circuit is shown schematically in Figure 4-3.

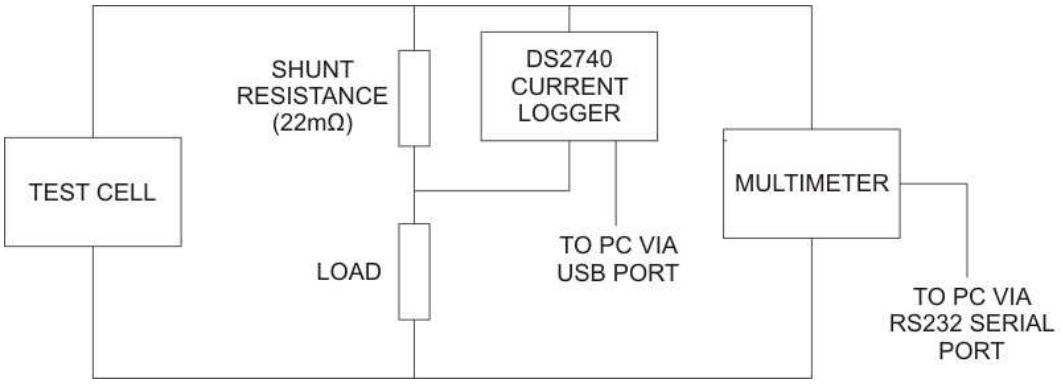

Figure 4-3 - Discharge circuit

The DS2740 [75] is an integrated circuit designed to monitor the charge level of batteries in electronic devices. It operates by measuring the voltage across a known small resistance, calculating the current flowing through the circuit from this voltage and integrating the current to calculate the total accumulated charge that has passed through the circuit. The chip outputs a signal to an RJ-11 cable, which in this case was connected to a PC via an RJ-11 to USB interface. A simple piece of software communicates with the chip and logs data from it as a text file.

The voltage reading was obtained from a multimeter. An Extech MT330 meter was used as it has an RS232 serial port interface and a software package that allows it to communicate with a PC. Again, the data were logged to a text file.

Both datasets were sampled every 10 seconds. To ensure that data were not lost, the logging was stopped and backed up every 4-5 minutes.

Uniform Acceleration Vibration Testing

The aim of the initial tests was to subject the cell to uniform acceleration only. In order to ensure that the cell responded to the vibration environment as a rigid body, that is, without being deformed significantly, it was held in an aluminium jig during testing. The jig, shown in Figure 4-4, was designed to have natural frequencies outside of the tested range (the purpose of the large pockets machined into the block was to

reduce the mass of the block, thus decreasing its response to vibration). The battery was secured in a properly sized recess inside the jig using double-sided adhesive tape, which was then attached to an LDS V830 electrodynamic shaker as shown in Figure 4-5 and Figure 4-6.

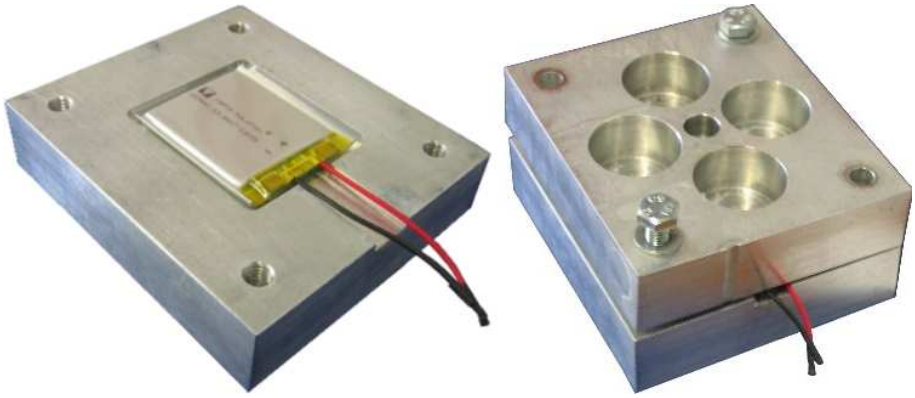

Figure 4-4 - Battery shaking jig

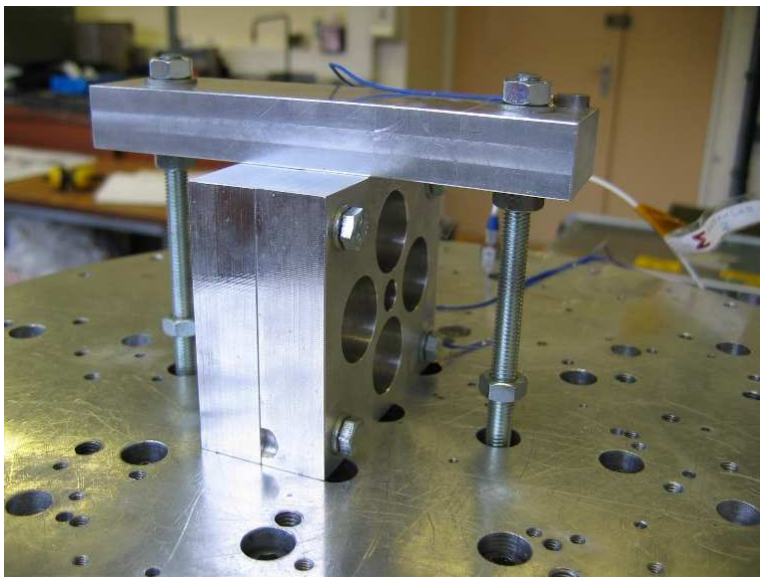

Figure 4-5 - The jig attached to the shaker

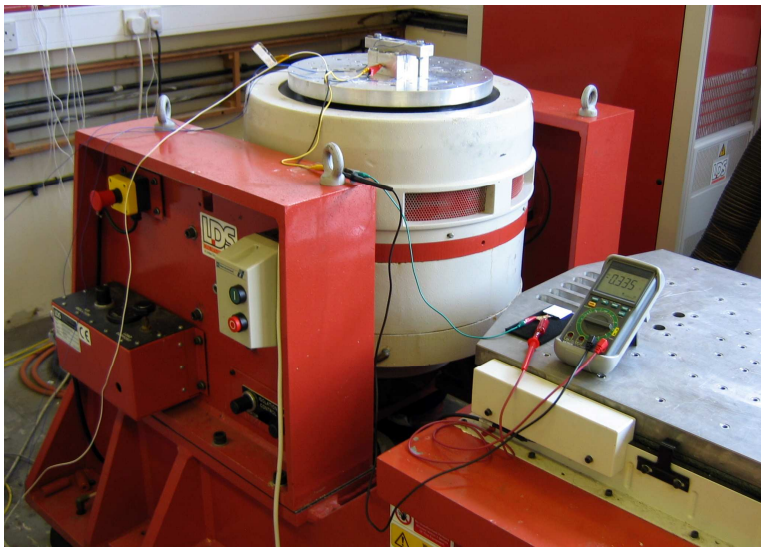

Figure 4-6 - Test setup, showing all apparatus

The random vibration profile, shown in Figure 4-7, was chosen to represent a generic spacecraft launch. The profile has a total acceleration of 15 g_{rms}. Each test lasts for a total of 12 minutes, consisting of one 4-minute period in each of the three principal axes. The duration is typical for a qualification test (in [61], for example, the duration was 2 minutes per axis).

The initial testing at 15 g_{rms} did not result in any measurable effect on the performance of the cell, as will be described in detail subsequently. As such, a single test was conducted at a higher level of acceleration. This test had an intensity of 25 g_{rms} and a similar profile to the 15 g_{rms} test as shown in Figure 4-7, with a slight reduction in intensity at low frequency to allow for the displacement limits of the shaker.

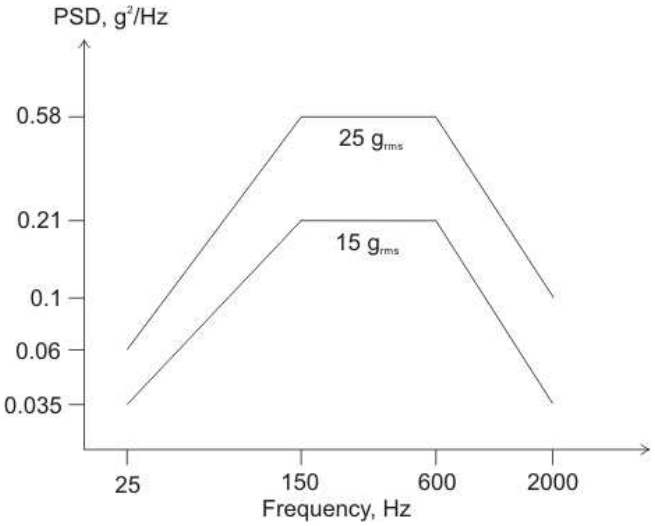

Figure 4-7 - Random vibration profiles

The response of the entire assembly to the input vibration was assessed by measuring the acceleration response at three points, as shown in Figure 4-8. A response profile for the apparatus is shown in Figure 4-9. The response shows that channel 2, the accelerometer attached to the clamp, followed the input profile correctly, aside from a slight increase in intensity at the higher end of the frequency range. This does not raise the overall loading significantly, however (the increase in acceleration is less than 0.5 g_{rms}), and the error may safely be considered conservative, since it would increase the loading on the batteries.

The larger deviations shown on channels 3 and 4 did not affect the loading on the battery, as these channels only measured the movement of the end of the bar holding the jig in place, and not that of the clamp itself. The accelerometers used for this testing were Endevco 2256-100 for the control channel (channel 1) and PCB Piezotronics 352A21 for channels 2-4.

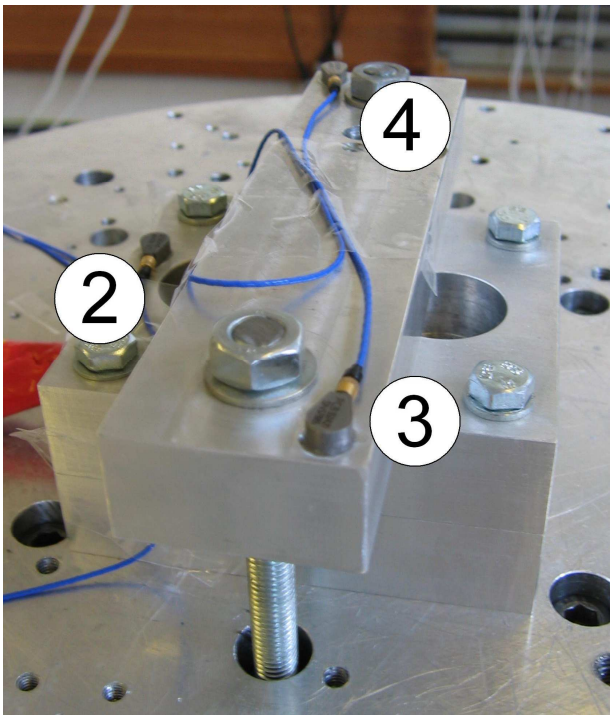

Figure 4-8 - Location of accelerometers; channel 1 (control) attached to baseplate

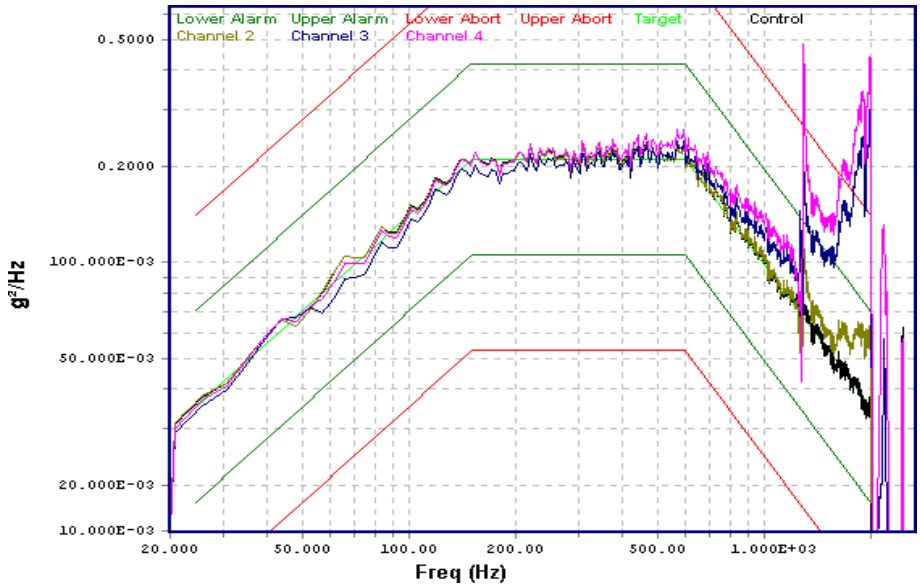

Figure 4-9 - Response of test apparatus to input vibration

4.2.3 Test Method

Rather than undertaking full characterisation of the cell after every electrical cycle as described in Section 4.1, the results of the testing were reduced to two simple parameters. This allowed notable changes in the cell's performance to be identified quickly and simply.

The two parameters chosen were based on the requirements of the cell's performance; degradation in one of these quantities could result in a reduction in the battery's lifetime. Although many factors may affect the choice of a cell for a space application, there are two principal specifications required from the battery pack: to provide adequate power to the spacecraft for a required period (i.e., storage of enough energy) and to provide the power level required at peak loads. The first parameter is represented roughly by the Ah capacity of battery, though it is slightly affected by the internal resistance of the cell. The maximum power output of a cell is not fixed per se, but is dependent on various factors such as the required lifetime (higher output power reduces cycle life) and the ease with which heat may be dissipated away from the cell. However, in terms of changes to the electrical properties of the cell, the most important factor is the internal resistance of the cell, which determines the amount of heat generated in the cell and the voltage reduction when current is drawn.

The total capacity of the cell is not easily determined, and discharging the cell fully will itself result in damage. Indeed, if a PLI cell is discharged fully, leakage or even flaming can occur. Instead, capacity is typically defined between two voltages, which in the case of lithium cells are usually 4.2 V (charged) to between 3 V and 3.5 V (discharged).

The charged voltage may vary slightly due to temperature when charging, and, as the charging was not carried out in a temperature-controlled environment, some temperature fluctuations would probably have occurred during the testing. However, given that all of the tests were carried out at a comfortable room temperature, this

would not have been sufficient to cause significant discrepancies in the data. Although published information on detailed behaviour is limited, the effect of temperature on performance in the vicinity of 20°C does not appear extensive [76]; most notably, the shape of the curve after the initial voltage drop at the start of discharge does not change shape significantly. Since the DOD and voltage may be logged precisely, a fixed amount of the cell's capacity was discharged, and the voltage drop from the start to the end of the fixed discharge measured. In order to eliminate the effect of transient internal resistances at the start of discharge, the voltage drop measured was from 5 to 25% DOD.

The depth of discharge in this case is defined by the manufacturer's specification of the cell's nominal capacity, namely 300 mAh. Thus, the region of investigation begins after 15 mAh have been discharged from the cell's fully-charged state, and ends after a total of 75 mAh have been discharged.

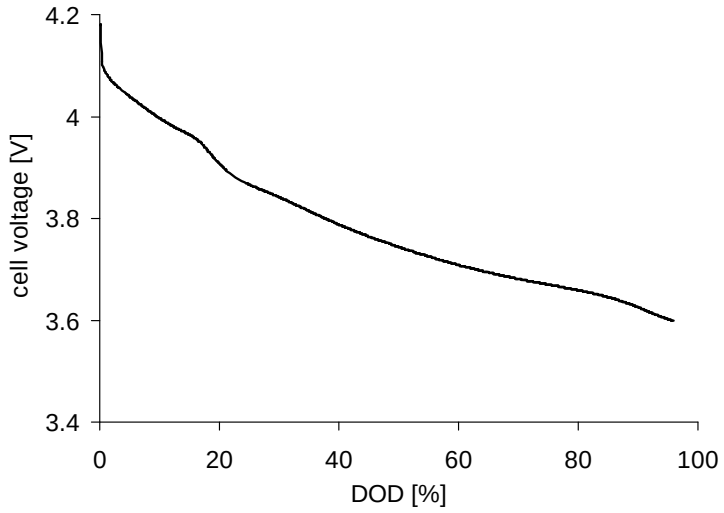

Figure 4-10 - Full discharge profile

The capacity parameter, therefore, is represented by the more easily measured end of discharge voltage, V_{EOD}. In addition to being representative of the cell's capacity, reductions in this parameter affect the lifetime of the battery, as a lower V_{EOD} will

eventually result in the battery delivering an insufficient voltage to operate the spacecraft.

The effect of internal resistance may be modelled as a circuit of several different electrical components in series or parallel with an ideal cell as described in [71]. The practical implication of this is that there are two components of the internal resistance: one that is a constant value ohmic resistance, and one that is governed by the capacitance of the cell's electrochemical components, and takes some time to reach equilibrium when the discharge current changes significantly. There is also a third component, but it is discounted as it only affects the behaviour of the cell during very low current discharges. Of the two relevant components of the resistance, the fixed ohmic resistance is the larger. Figure 4-11 shows the behaviour of the cell after the discharging current ends: the initial, virtually instantaneous voltage jump (of around 130-150 mV) is caused by the fixed resistance, whereas the other component results in the exponentially decaying voltage change as shown.

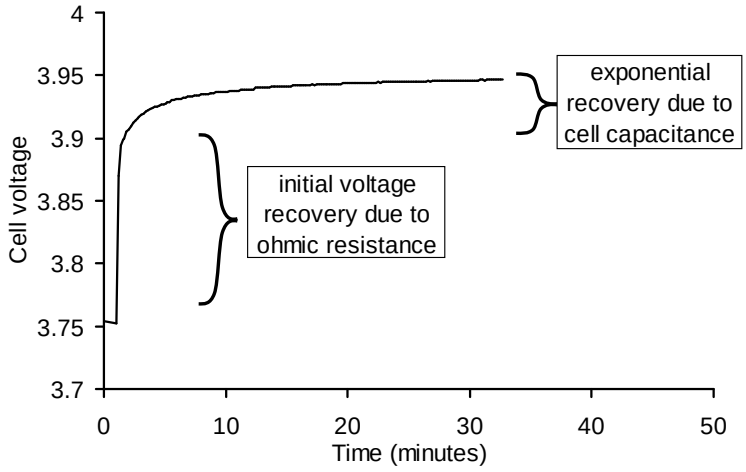

Figure 4-11 - Voltage change after end of discharge

The voltage recovered 15 minutes after the end of the discharge, V_{REC}, was used as the means of indirectly measuring the internal resistance. Since the actual value of the resistance is not significant, the voltage recovery at the end of the discharge is used as

is. Any change in the voltage recovered is indicative of a proportional change in the internal resistance.

In summary, therefore, the two indices used to measure performance changes in the cell are V_{EOD} and V_{REC}.

4.2.4 Test Results and Observations - 15 g_{rms} Tests

The logged data was processed in an Excel spreadsheet and the performance indices extracted. The results are presented in Figure 4-12 and Figure 4-13. Each point on the graphs indicates one complete discharge/charge cycle, and, where a vibration test occurred between two cycles, this is indicated by a dashed line and arrow.

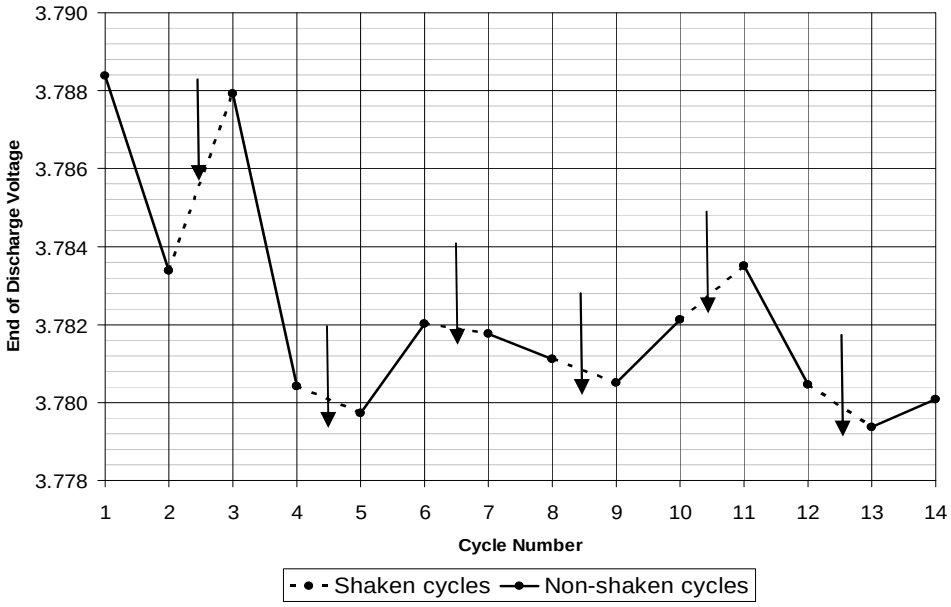

Figure 4-12 - Measured value of V_{EOD} after each test

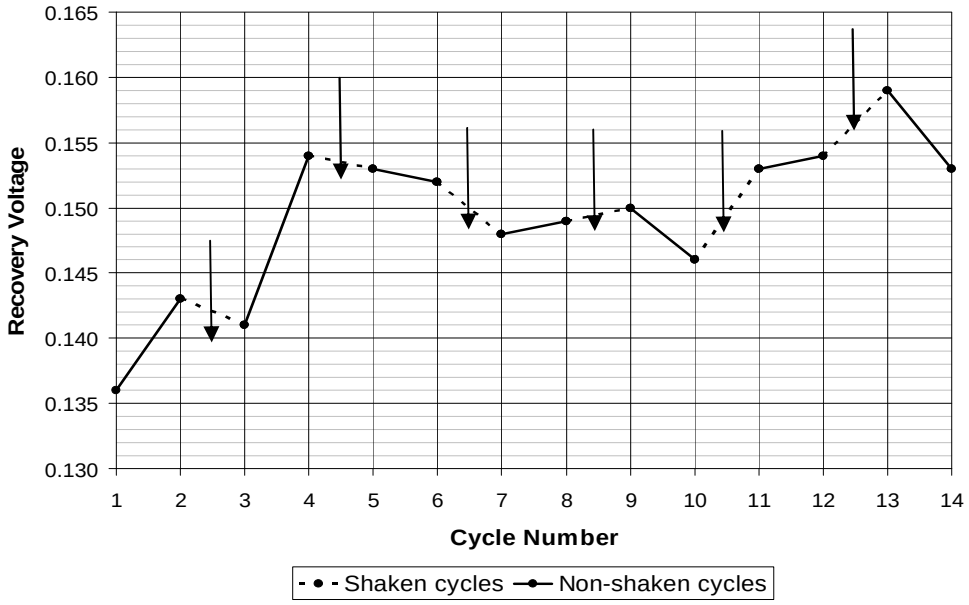

Figure 4-13 - Measured value of V_{REC} after each test

In order to clarify the magnitude of the change in the cell's performance, the changes in V_{EOD} and R_{INT} relative to their initial values are shown in Figure 4-14 and Figure 4-15.

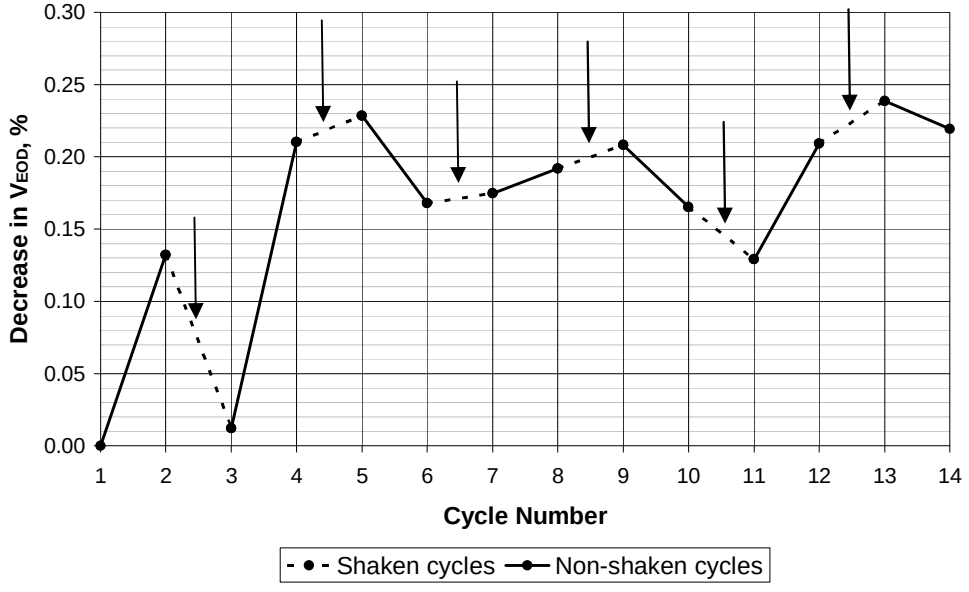

Figure 4-14 - Relative change in V_{EOD} from initial measurement

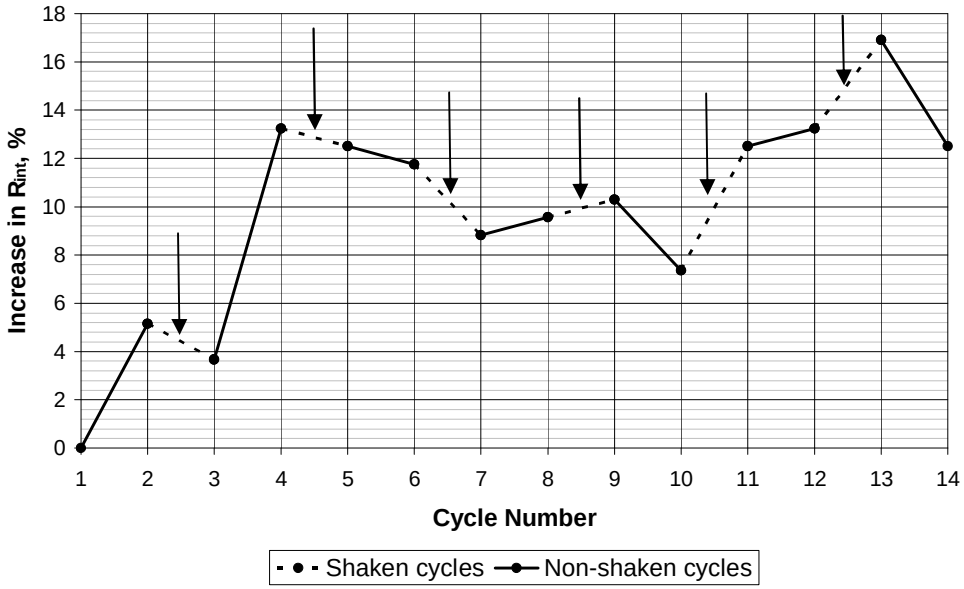

Figure 4-15 - Relative change in R_{INT} or V_{REC} from initial measurement

There is a small loss of performance over the 14 electrical cycles as expected, but there is no evident correlation between loading and performance change. In fact, the largest loss in performance occurs after cycles one and three, neither of which was shaken (damage may therefore have been caused by errors in the charging process, or the variation may be due to changes in ambient temperature). Indeed, if these two cycles are discounted there is no notable change over the course of the testing, suggesting that the measured variation is simply "noise" in the results.

For the V_{EOD} results, a lower limit can be set that determines the life of the battery, namely 3V. This is the defined 100% DOD for the cell when new, and, regardless of any changes in capacity due to aging, the cell should never be discharged below 3 V, as doing so would result in complete loss of function. The V_{EOD} after the first 25% DOD cycle is 3.788 V, and after all 14 cycles there is a total drop of 8 mV. Thus, for 25% DOD cycling, the cell is around 1% closer to failure after the testing. Neglecting the large drop after cycle 3, the overall change would be negligible.

There is no such limit for internal resistance and, ostensibly, the overall increase of 12% appears significant. However, the anomalous change after cycle 3 (unshaken) once more accounts for the majority (9%) of this change; neglecting this cycle, there appears to be significant change over the testing campaign.

4.2.5 Statistical Analysis of 15 g_{rms} Tests

End of Discharge Voltage

The mean change in this quantity, whether shaken or not, was -0.639 mV after each cycle. The mean change for unshaken cycles was -1.63 mV, and for shaken cycles, the mean was +0.539 mV (i.e., there was, on average, a performance *gain* after subjecting the cell to vibration, and a loss otherwise). The standard deviation of the change in V_{EOD} was 3.14 mV. A plot of the deviation of the change in V_{EOD} after each cycle from the mean value is shown in Figure 4-16, with the scale being the standard deviation of the data. This indicates that only the first three cycles resulted in a change in excess of one standard deviation. Of these, two resulted in a reduction in V_{EOD}, i.e., a reduction in performance, neither of which occurred after the cell was subjected to vibration.

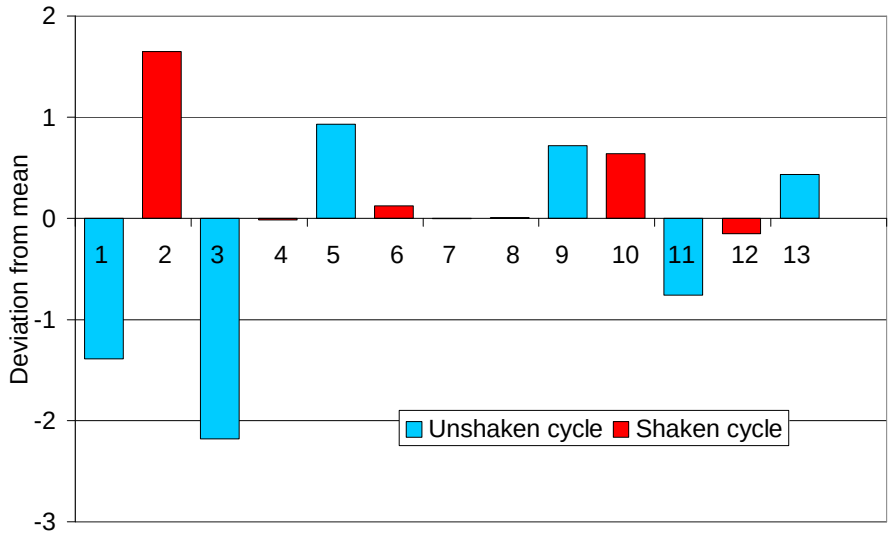

Figure 4-16 - Deviation of V_{EOD} from mean value, shown in terms of standard deviation

Recovery Voltage (Internal Resistance)

The mean change in V_{REC} over all 14 cycles was +1.31 mV per cycle. Again, more degradation in performance was observed for unshaken cycles – +1.57 mV per cycle, as opposed to +1.00 mV per cycle for shaken cycles. The standard deviation across all data was 5.38 mV. These data are presented in Figure 4-17.

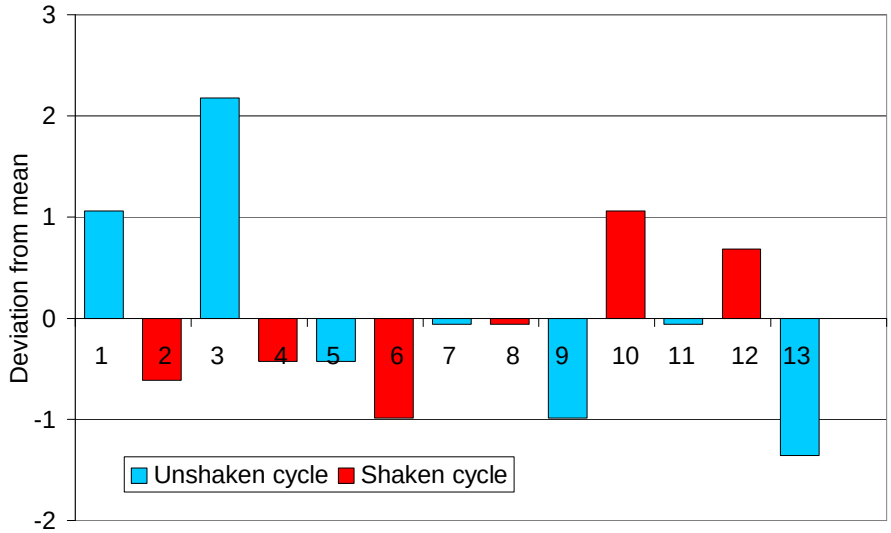

Figure 4-17 - Deviation of V_{REC} from mean value, shown in terms of standard deviation

Once more, cycles 1 and 3 differ from the mean value by more than 1 standard deviation (over 2 standard deviations in the case of cycle 3). Both of these cycles showed a loss in performance and did not occur after vibration. Cycle 10 showed a significant loss in performance associated with a cycle after a vibration test, but, since more degradation occurred in V_{REC} after non-shaken cycles, there is no evidence for a correlation between vibration and performance loss.

4.2.6 Results and Observations - 25 g_{rms} Tests

Only one vibration test was carried out at 25 g_{rms}, with four charge/discharge cycles to electrically characterise the cell before and after the test. The results of this testing are summarised in Table 4-2.

Cycle no.	V_{EOD}, V	V_{REC}, V
1	3.795	0.193
2	3.793	0.182
25 g_{rms} VIBRATION TEST		
3	3.794	0.183
4	3.795	0.188

Table 4-2 - Results of 25 g_{rms} vibration test

The end of discharge voltage actually increased (i.e., performance improved) after the vibration test, whilst recovery voltage increased by a mere 1 mV (slightly more than 0.5%, but less than the standard deviation of the 15 g_{rms} data, 5.38 mV).

4.2.7 Summary of Results

Whilst this testing is not conclusive, the fact that there is no measurable degradation within the errors of the equipment used is an encouraging result. Whilst further testing would be required to gain more reliable results, it can be said with adequate confidence that the PoLiFlex cells are resilient to the launch environment.

4.3 Mechanical Characterisation of Cells

In order to model the behaviour of multifunctional panels, it is necessary to have knowledge of the mechanical attributes of the cells. This section describes the testing conducted to investigate the performance of PoLiFlex cells in this regard. A series of dynamic tests were carried out with the aim of determining the shear modulus and ultimate stress of the cells.

4.3.1 Required Data

Since the cells are to be employed as a part of the core of a sandwich panel, the material characterisation shall focus on those attributes relevant to this application (as

for other core materials), namely the shear moduli in the plane of the panel. Also of potential interest is the compressive modulus, though this usually has less of an effect [77]. Rather than determining both the shear and compressive moduli, the shear modulus was measured first. A sensitivity analysis was then undertaken, using finite element models, in order to demonstrate that the knowledge of the precise value of the compressive modulus was unnecessary to produce accurate models (Section 4.3.9).

The failure characteristics of the cells are also of importance. Given the dual functions of electrical energy storage and structural load-bearing, both structural and electrical failure due to mechanical loading are significance. Testing lithium cells to destruction, as would be done with normal structural components when investigating mechanical failure, can be hazardous due to the potential leakage of toxic or corrosive chemicals. Potentially, failure of the cells' environmental protection could result in fire. For this reason, the maximum stress the cells can undergo without failure was not measured directly, though the level of stress encountered during testing sets a lower bound on this quantity.

4.3.2 Cell Model Selection

The PoLiFlex range of cells had already been selected for earlier testing (Section 4.2), so cells of this type were also used for the mechanical testing. Since the shear modulus of the batteries out of their own plane was to be measured, a thicker cell was most useful as it allowed greater displacements, and hence more accurate measurements. At the time of testing, the thickest PoLiFlex cell available was the PLF 523450 model, with a thickness of 5.2 mm. This cell was thus used for the mechanical tests.

4.3.3 Methodology

Given that the batteries are still comparatively thin, measuring the shear modulus statically would require relatively sensitive measurement of displacement. In addition, the forces produced by the testing machines available in a standard structural testing

facility would be likely to result in failure of the test article without any useful data being gathered.

An easier approach in this context is to determine the value of the shear modulus dynamically. This does not require such large displacements, as the acceleration response is of interest, and the loading applied to the cells can be carefully controlled. A simple "mass and spring" system can be constructed using several cells loaded in shear as the spring and an appropriately sized steel block as a mass. Measuring the natural frequency of the system allows the stiffness of the "spring", and hence the shear modulus of the cells, to be determined. This method has been used previously by other authors to assess the shear modulus of multifunctional battery materials [63].

4.3.4 Experimental Apparatus & Procedure

The PLF523450 cells were arranged in four pairs as shown schematically in Figure 4-18. Excitation was applied to the frame across a range of frequencies. The accelerometer mounted on the mass measured the response of the system on the direction of the excitation, the plotted response showing the resonant frequencies.

The frame was machined from 10 mm and 15 mm aluminium plate and assembled by means of M4 steel bolts and studs as shown in Figure 4-19 (note that only half the batteries are in place in this image). The interfaces between the batteries and the frame and the batteries themselves were fixed using a thin layer of Araldite epoxy adhesive. A box structure was adopted to prevent other modes of vibration (mainly those of the frame itself) from being excited and to ensure the cells were not excessively loaded during the testing.

In addition, the block was fixed to the frame at both ends using 0.2 mm steel shim, thus supporting the weight of the block and constraining it to oscillate in the correct axis, shown schematically in Figure 4-20. Figure 4-21 shows the completed apparatus. After the completion of the experiments, an FE model confirmed that the influence of

the shims on the results was negligible. The FE modelling will be covered in more detail in Section 4.3.7, since the results of the experiments are required to properly model the system.

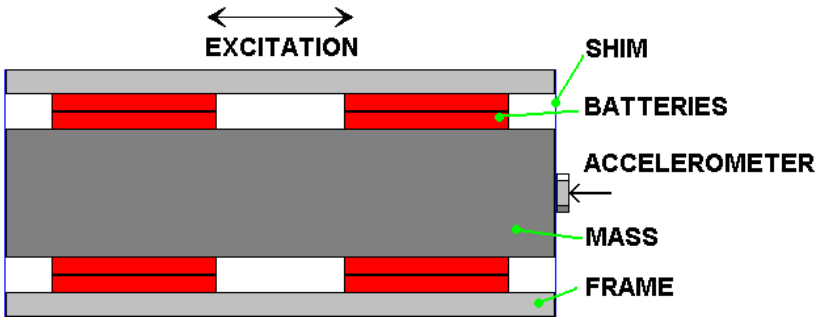

Figure 4-18 - Schematic view of experimental set-up (from above)

The steel block has a mass of 2.94 kg; each cell has a thickness of 5.2 mm and an area of 1673 mm^2. The cells are arranged in four pairs (i.e., the effective thickness is doubled, and the area quadrupled).

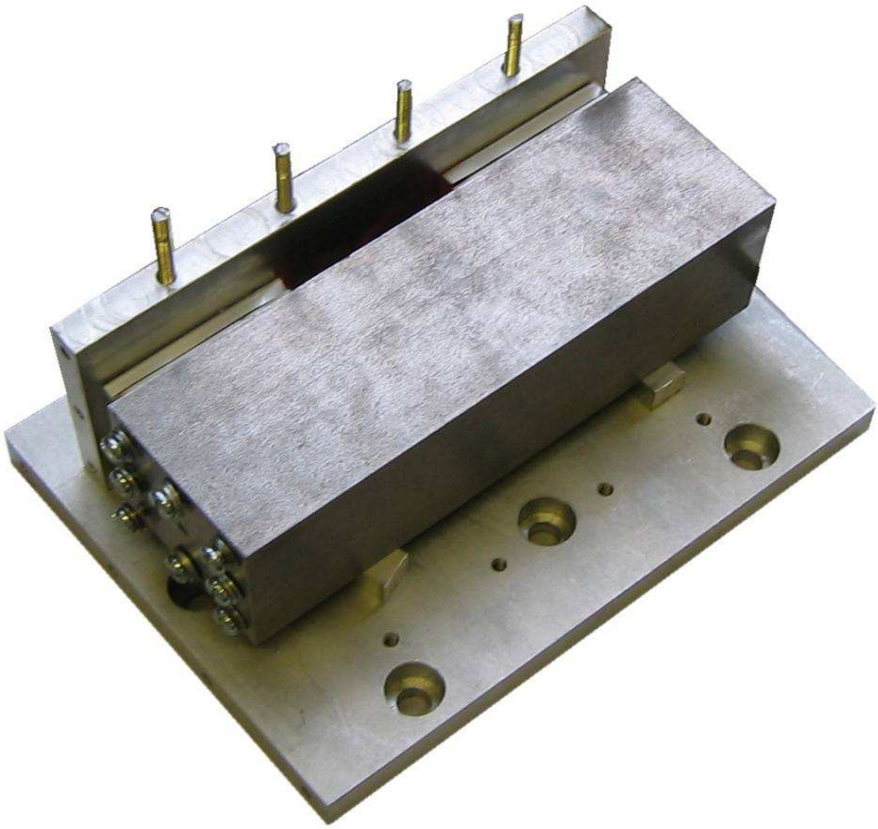

Figure 4-19 - Partially assembled apparatus

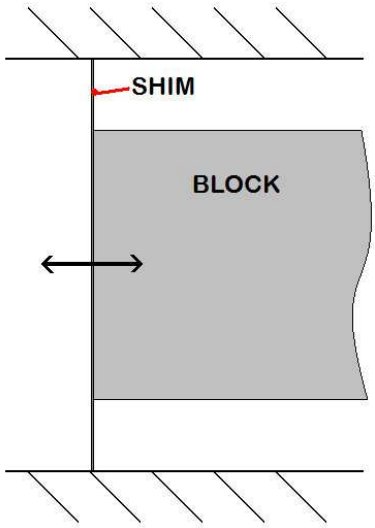

Figure 4-20 - Use of shim to constrain oscillation

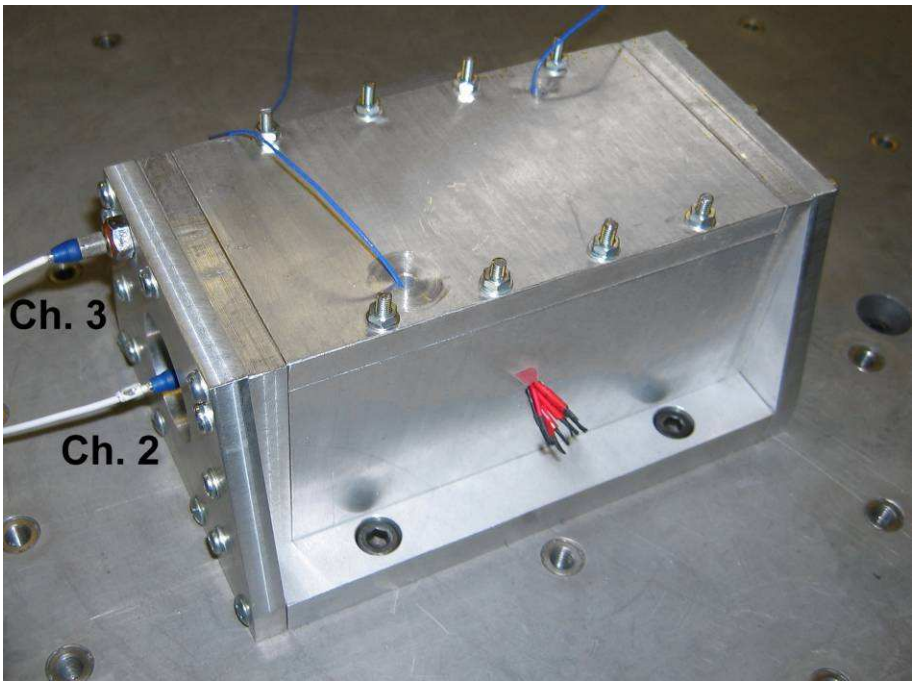

Figure 4-21 - Assembled apparatus on the slip table, showing accelerometer channels 2 and 3

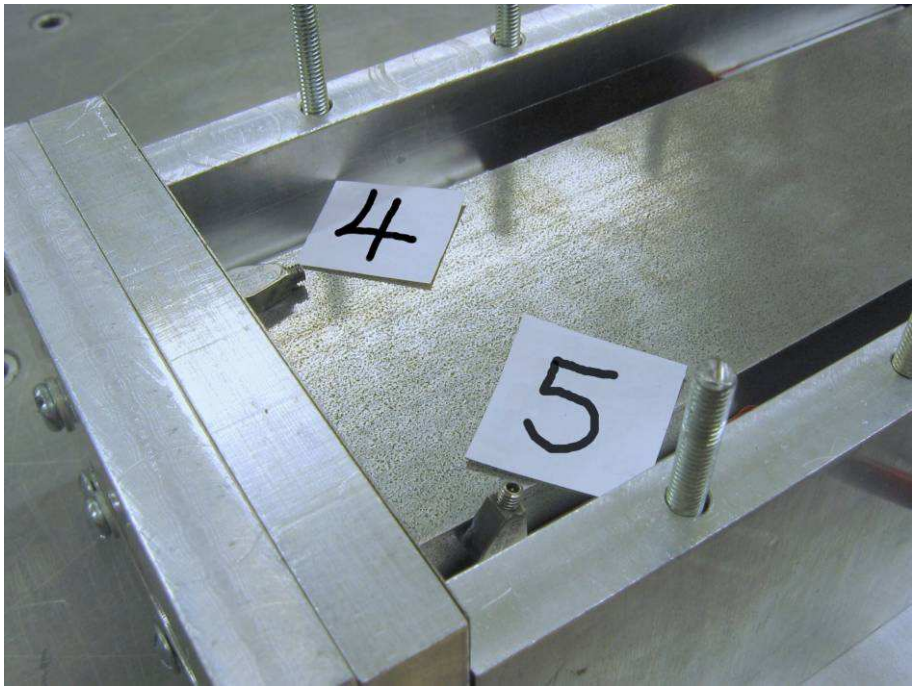

Figure 4-22 - Detail showing position of accelerometer channels 4 (vertical) and 5 (lateral)

The frame was bolted to the slip table of an LDS V830 electrodynamic shaker. In addition to the accelerometer mounted on the block, several additional accelerometers were attached to the frame and block in order to monitor the overall response of the system and ensure that no other resonance was occurring. Channel 1 was the control channel, mounted on the slip table itself. The positions of channels 2 (mounted on the central block) and 3 (mounted on the outside of the frame) are shown in Figure 4-21. The locations of channels 4 and 5, which measure the response of the steel block out of the intended plane, are shown in Figure 4-22. The accelerometers used were Endevco 2256-100 for channels 1-3 and PCB Piezotronics 352A21 for channels 4 and 5. The data were sampled at a rate of 2.5 kHz (due to the nature of the data acquisition system used, no time history data was available).

After assembling the frame as shown, the apparatus was subjected to a 0.05 g sine sweep from 100 to 1000 Hz at 2 oct/min to identify the location and magnitude of the system's resonances. Once the level of amplification in resonance was identified, a series of sine tests at increasing acceleration levels was completed (the levels being shown in Table 4-3). The output cables from the batteries were left accessible during this testing to observe whether or not they continued to function, though due to time constraints, no detailed investigation of electrical performance was conducted.

4.3.5 Results

The results of the vibration tests are summarised in Table 4-3 and Figure 4-23. Due to the variation of the frequency and magnitude of the system's response with respect to the magnitude of the input, some of the sine tests were repeated to establish whether this was due to permanent mechanical degradation, hence the last seven tests are duplicates.

As noted previously, three additional accelerometers were mounted on the apparatus to ensure that there was no motion in the apparatus other than the desired translational motion of the steel block. The response of all five channels during a 0.25

g_{rms} sine sweep is shown in Figure 4-24. The chart confirms that the response of the frame in the axis of excitation (channel 3) is not significant compared to the desired response of the block (channel 2) and that the shim restraining the ends of the block was sufficient to prevent the block from undergoing significant oscillations in the other two axes (channels 4 and 5). A plot of the amplification factor (the ratio of the system's response to the input acceleration) exhibited by channel 2 is shown in Figure 4-25. The reduction in frequency and amplification at resonance with higher input shown in this plot suggests that the cells behave as a softening spring when loaded in this way.

Test #	Input (g_{peak})	Resonance (Hz)	Max. response (g_{peak})	Amplification factor (response/input)
A1	0.27	553	2.15	7.90
A2	0.54	517	3.48	6.51
A3	0.81	487	4.46	5.70
A4	1.07	455	5.27	4.94
A5	1.34	432	5.93	4.39
A6	1.61	410	6.73	4.17
A7	1.88	391	7.45	3.91
A8	2.15	375	8.40	3.89
A9	2.69	342	9.68	3.59
A10	3.22	317	10.6	3.30
A11	3.76	298	11.6	3.09
A12	4.30	278	12.4	2.89
A13	5.37	257	14.0	2.61
A14	6.43	238	15.9	2.46
A15	7.47	221	17.5	2.31
A16	8.55	195	19.1	2.22
A17	9.62	182	20.4	2.09
A18	10.7	171	21.5	2.00
Repeated tests				
B22	0.27	512	1.57	5.85
B23	0.80	422	2.91	3.62
B24	1.07	382	3.40	3.17
B25	2.15	290	5.90	2.75
B26	3.22	248	8.85	2.75
B27	4.29	228	11.5	2.68
B28	5.37	208	13.3	2.47

Table 4-3 - Results of dynamic testing

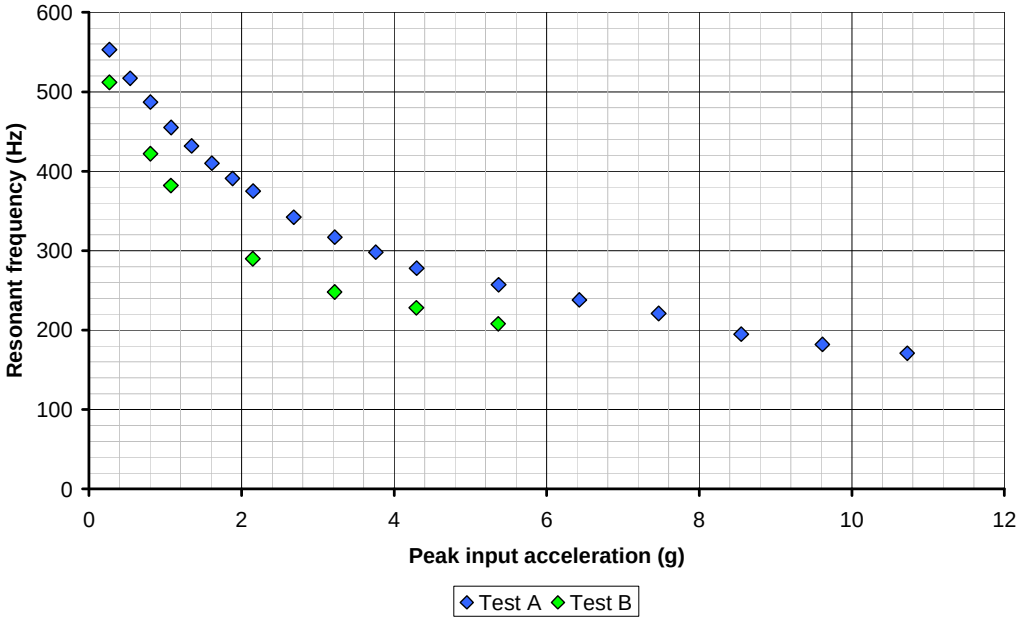

Figure 4-23 - Resonant frequency vs. input acceleration

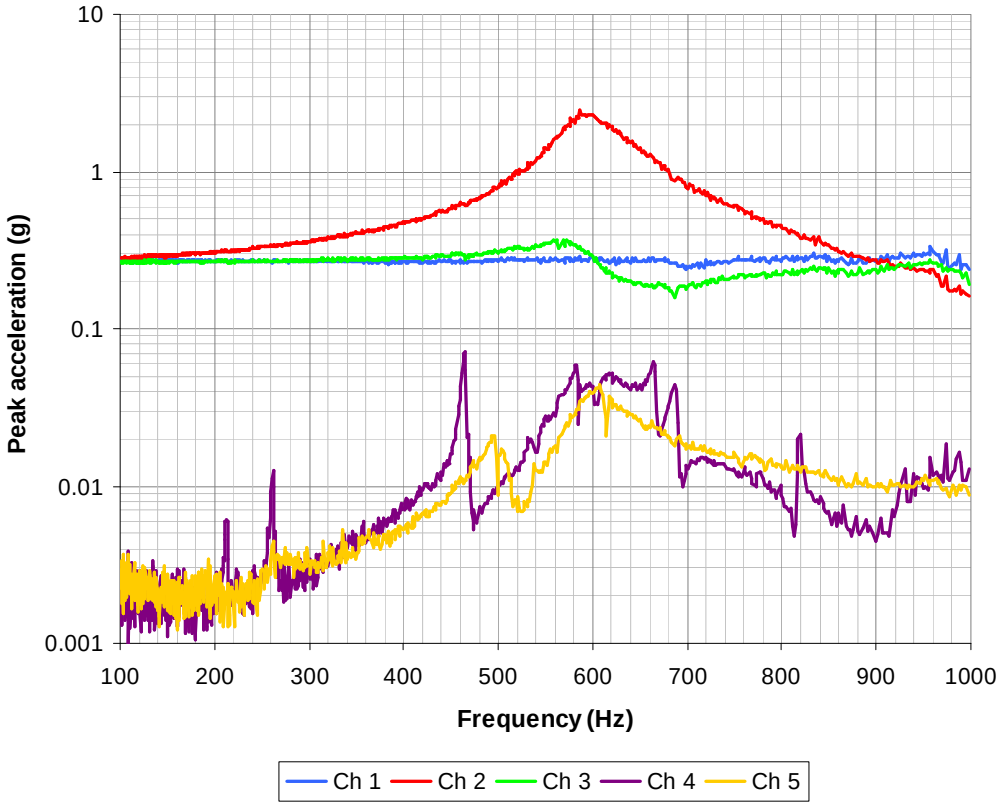

Figure 4-24 - Acceleration response of all channels at 0.25 g_{rms}

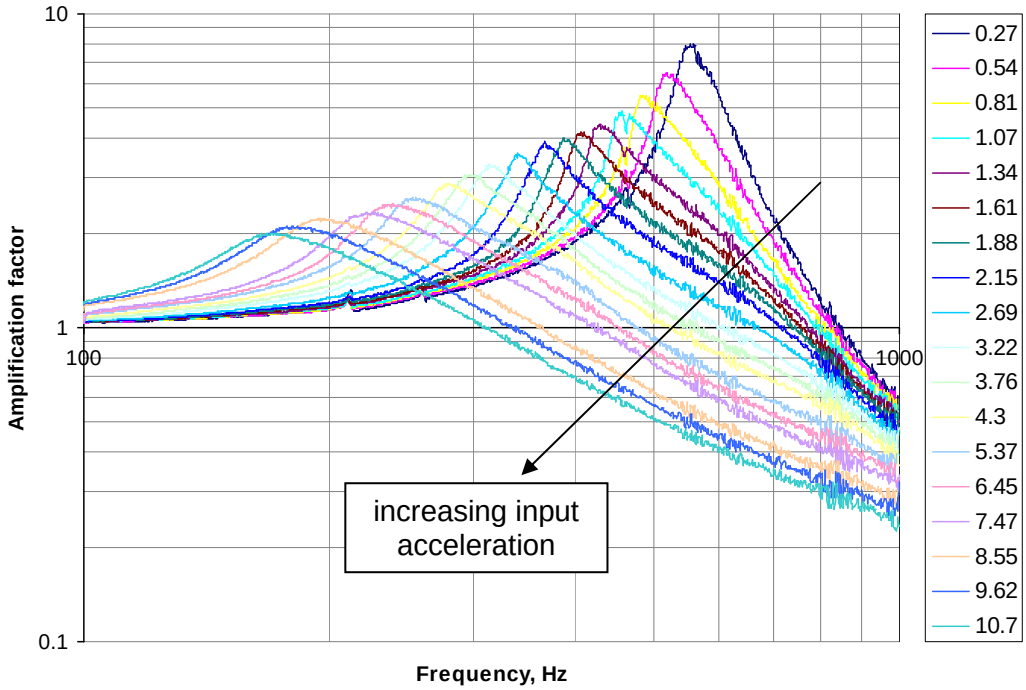

Figure 4-25 - Amplification factor on channel 2 vs. frequency.

The legend indicates the magnitude of the input acceleration (g_{peak}).

4.3.6 Analysis

In order to calculate the shear modulus of the batteries, the testing apparatus will be modelled as a simple mass and spring system as described above. The natural frequency of a simple mass and spring system is given by the following equation:

$$f = \frac{1}{2\pi}\sqrt{\frac{k}{m}} \tag{4-1}$$

Where f is the natural frequency, m is the mass of the moving part (2.94 kg in the case of the steel block used in this apparatus) and k is the stiffness constant of the spring.

In this case, the stiffness of the spring is determined by the attributes of the cells supporting the block, as loaded in shear:

$$k = \frac{G \times A}{h} \tag{4-2}$$

Where G is the shear modulus, A is the total area of the test articles loaded in shear and h is the thickness of each pair of batteries. As there are four pairs of batteries, A is equal to 4 times the area of one battery (4 x 1673 mm^2) and h to twice the thickness of one battery (2 x 5.2 mm).

Substituting and rearranging gives the following expression for G in terms of the measured natural frequency and other known quantities:

$$G = (2\pi f)^2 \frac{hm}{A} \tag{4-3}$$

Evaluating the value of G for the measured natural frequencies gives the results shown in Figure 4-26. As the figure shows, increasing acceleration (and hence stress) results in a dramatic reduction in stiffness. In addition, data from the repeated tests suggest that the structural properties of the cells were degraded during the course of the initial tests, since the values calculated for stiffness are considerably lower during the second run of tests.

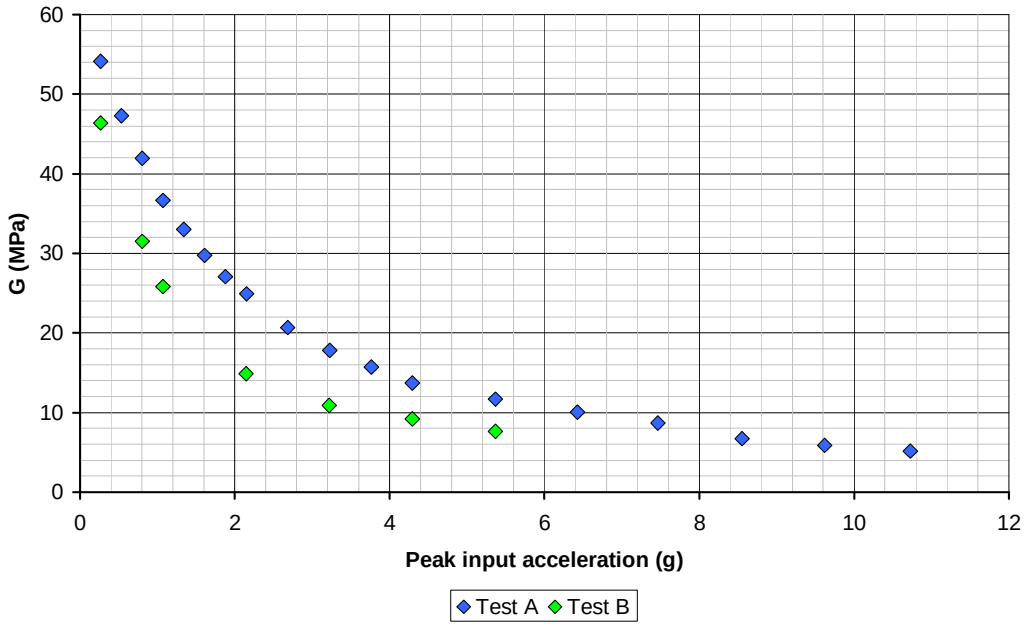

Figure 4-26 - Measured shear modulus vs. input acceleration

The amplification factor* (and hence the damping) of the system at resonance also varies with the input acceleration, and so Figure 4-26 does not directly indicate the relationship between stiffness and the level of stress in the batteries at resonance. It is necessary to understand this relationship in order to select an appropriate value of *G* for use in modelling, and so the shear stress must be calculated.

Shear stress in a material is equal to the shear force applied to it divided by the cross sectional area over which the shear force is applied. In this case, the cross section of the battery stacks is approximately uniform through their thickness, and so the shear stress throughout them may also be assumed uniform. The peak shear force applied to the battery stacks is calculated by multiplying the mass of the block by the peak acceleration at resonance. The effective cross sectional area of the four stacks of batteries is, as above, 4 times the cross sectional area of one battery. Hence, the peak shear stress is given by:

* The ratio between the acceleration response of the system and the input acceleration.

$$\tau_{peak} = \frac{ma_{out,peak}}{A} \tag{4-4}$$

A and m have the same meaning as previously in this section; $a_{out,peak}$ is the peak acceleration response of the block. The relationship between G and the shear stress in the batteries is shown in Figure 4-27.

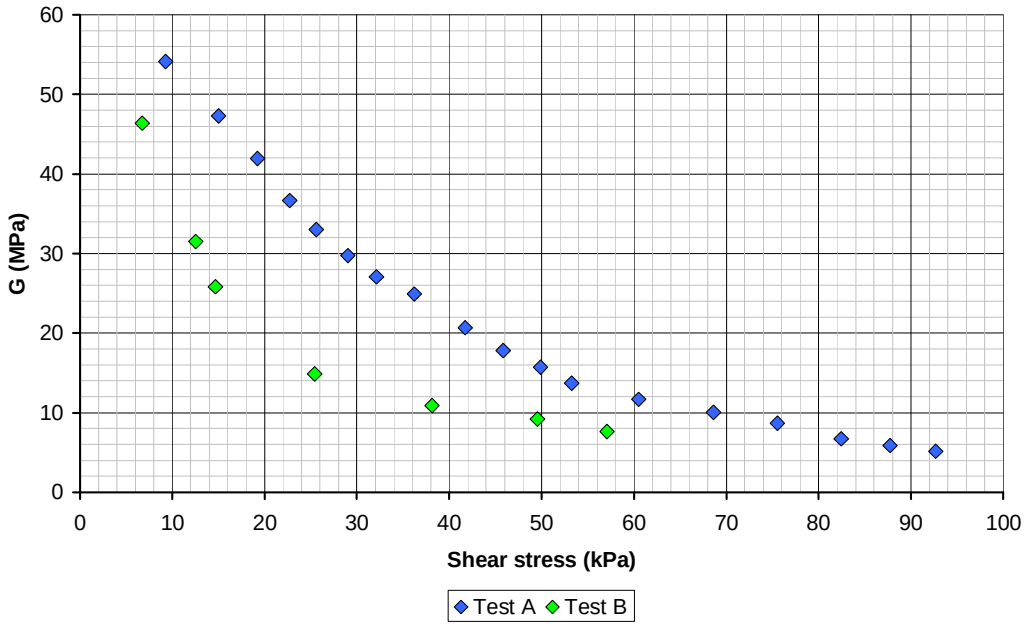

Figure 4-27 - Measured shear modulus vs. applied shear stress

When compared to the results in Figure 4-26, this chart shows a more significant change in the properties of the cells during the second series of tests. Increased damping results in less displacement, and hence, less stress on the cells. Comparing the amplification factor (the ratio of the acceleration of the block to the input acceleration) at resonance to the shear stress indicates the change in the damping characteristics of the cells. This relationship is shown in Figure 4-28.

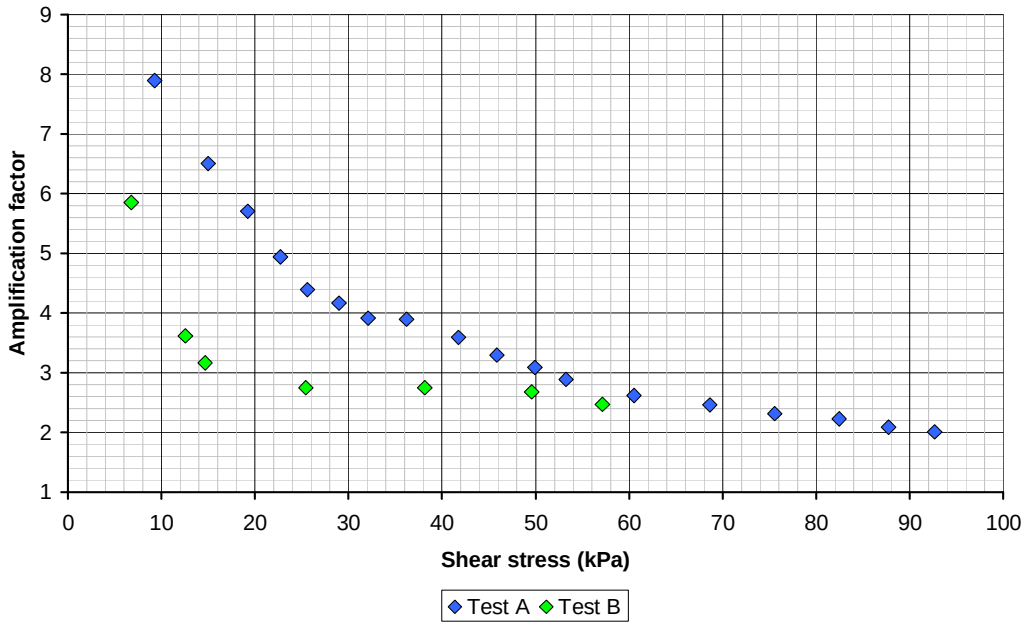

Figure 4-28 - Measured amplification factor vs. applied shear stress

The response of the block decreases significantly with increasing stress, more so during the second test, indicating a corresponding increase in damping. This effect may, equally, be attributable to a dependence on frequency or displacement; unfortunately, time constraints prevented further experimental investigations into the cells' non-linear behaviour.

4.3.7 Comparison with FE Model

An FE model of the testing apparatus was produced prior to the experiments in order to ensure that the frame itself would not respond to the applied vibration in a manner that could affect the results. This model correctly predicted that the frame's first mode of vibration would not fall within the frequency range used during the testing, and showed that the use of the shim to support the block laterally should not affect the longitudinal motion significantly. However, at the time, the stiffness of the cells was an unknown quantity, and so the cell material was substituted with polythene in the model. The fact that the cells' measured stiffness was much lower than this assumed

value, together with their damping characteristics, required that the FE model be re-run, with these attributes included. The highest acceleration cases are particularly important, since the low resonant frequencies would result in larger displacements than anticipated. The shim is more likely to affect the results under these circumstances: being very thin, the shim has little bending stiffness, but has significant load-bearing properties when loaded in tension.

For this reason, it was important to assess the effect the shim could have on the results under these conditions. Four models were produced, therefore, using the mechanical properties of the cells at the lowest and highest tested input acceleration (0.27 and 10.7 g_{peak}, respectively) and with the presence of the shims either neglected or included in the model. The mesh of model, generated using the Ansys® Workbench software package, is shown in Figure 4-29, with a partial cutaway to show the batteries, block and shim, while Figure 4-30 shows the first mode shape result, with the frame hidden, as produced by a modal analysis. The details of the elements used in the model can be found in Table 4-4.

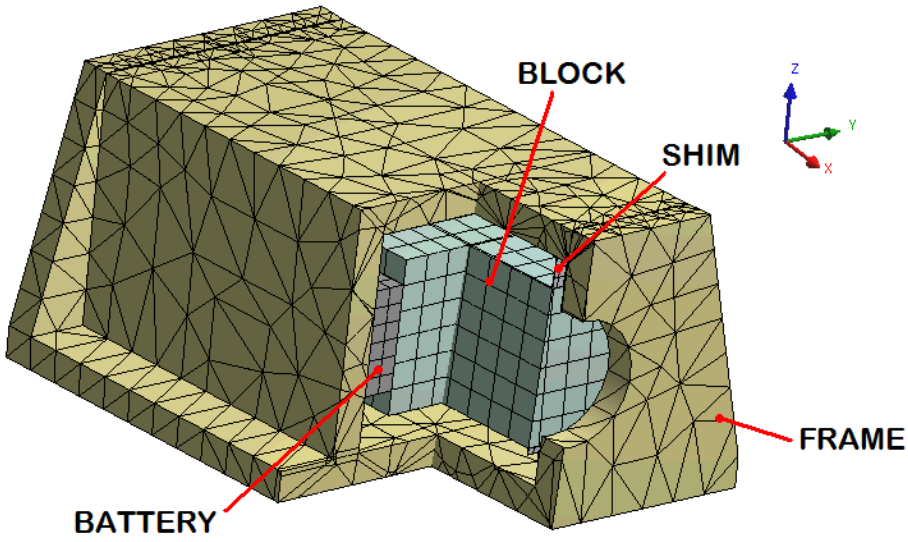

Figure 4-29 - FE model of battery shear testing rig (partial cutaway)

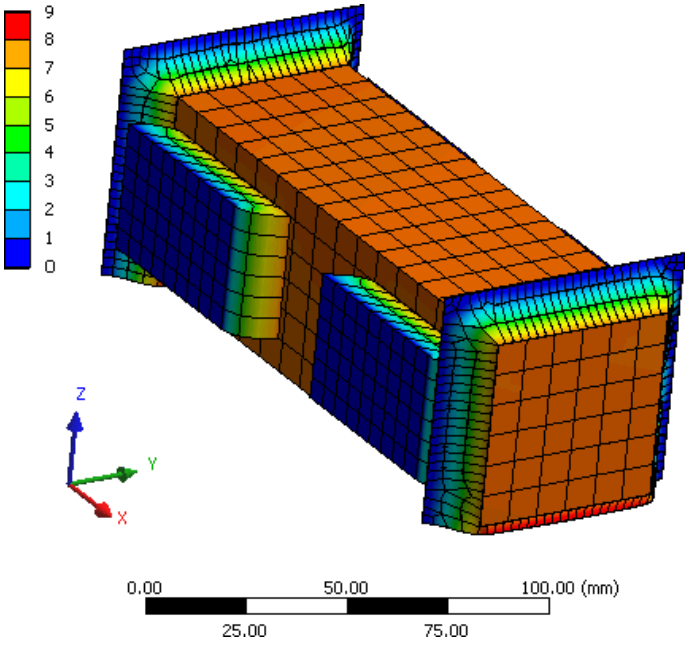

Figure 4-30 - First mode shape, showing block, batteries and shim.

Scale shows normalised displacement.

Component	Element type	Number
Frame	Solid187 - 10 Node Tetrahedral Structural Solid	2481
Block/Batteries	Solid186 - 20 Node Hexahedral Structural Solid	1008
Contact	Conta170 and Conta174	1224
Total (no shim)	**-**	**4713**
Shim	Shell181 - 4 Node Linear Quadrilateral/Triangular Shell	507
Total (inc. shim)	**-**	**5220**

Table 4-4 - FE model attributes

To provide a comparison with the experimental sine tests, a harmonic analysis (using the mode superposition method) was undertaken. The entire base (lower Z face) of the external frame was fully constrained (rotation and translation) to represent the apparatus being bolted to the slip table.

The non-linear behaviour of the cells could not be included in the model, so instead, the two loading cases were considered separately, with different material properties being used for the cells for each of the two acceleration levels. The stiffness has

already been calculated, in the previous section, but, for the purpose of this modelling, it was necessary to calculate the viscous damping ratio, ξ, at resonance. The damping ratio is related to the amplification factor, or transmissibility, Q, of the system by equation (4-5), assuming that the peak response occurs near to the natural (i.e., undamped) frequency of the system.

$$Q = \sqrt{\frac{1+(2\xi)^2}{(2\xi)^2}} \tag{4-5}$$

This rearranges to give:

$$\xi = \frac{1}{2\sqrt{Q^2 - 1}} \tag{4-6}$$

The battery characteristics used for the model, including the calculated values of the damping factor, are given in Table 4-5, and the results of the modelling are shown in Table 4-6 and Table 4-7. Note that only the results of the model at resonance are given; the analysis is linear, whilst the real system is not, and so the calculated material properties would not be valid away from the system's resonance.

Model	Shear modulus (MPa)	Input acceleration (g_{peak})	Amplification factor, Q	Damping ratio, ξ
Low level	54.1	0.27	7.9	0.06
High level	5.2	10.7	2.0	0.29

Table 4-5 - Battery characteristics for FE model

Result	Maximum response, g	Resonant frequency, Hz
Experimental data	2.15	553
FE model, with shim	2.14	525
FE model, without shim	2.14	523

Table 4-6 - Results for low level (0.27 g) tests

Result	Maximum response, g	Resonant frequency, Hz
Experimental data	21.5	171
FE model, with shim	19.5	183
FE model, without shim	19.4	184

Table 4-7 - Results for high level (10.7 g) tests

These results correlate well with the experimental results, the predicted response and frequency for all four models being within 10% of the measured value. More importantly, the model indicates very little change in the predicted response when the shim is removed, supporting the assumption that the measured response of the system is due to the batteries and not the shim.

4.3.8 Interpretation of Results

Shear Modulus

The most significant observation from this testing is the relatively low value of the shear stiffness of the cells: even its highest value, 54.1 MPa, is an order of magnitude smaller than that of a typical honeycomb core material. This is less than might be hoped for, and limits how much mass may be saved through using the batteries in an MFS. However, it does simplify the considerations given to the battery components when designing such a structure.

The non-linear relationship between stress and stiffness would, under other circumstances, present a complex problem with regards to structural design. If the stiffness of the batteries was high, it would be desirable to make use of this stiffness to enhance the dynamic behaviour of the MFS; however, loading them excessively would reduce this stiffness. Likewise, detailed knowledge of the mechanical degradation demonstrated in Figure 4-27 would be required if the cells were to be subject to structural loads, to establish how much loading could safely be applied

without causing permanent structural deterioration. However, the low stiffness of the cells renders this somewhat less relevant, as it is necessary to minimise loads upon them in any case. In addition, whilst the effect of shear loading on the electrical characteristics of the cells has not been investigated in detail, it would once again be necessary to minimise stress on the cells if it was found that this loading did cause degradation in their performance.

In summary, whilst the poor structural characteristics of the PLI cells make them less useful as structural components, this poor performance leads to a simpler design approach, as all requirements reduce to that of minimising the stress in the batteries. This eliminates the need to consider the effect of high stress levels on the structural and electrical performance of the batteries, though it does mean that additional structure may be required to maintain adequate mechanical performance.

Damping Characteristics

Although the stiffness of the cells was found to be poor, their damping characteristics do show promise, with the critical damping ratio exceeding 25% when the cells are heavily loaded. Thus, the cells can contribute to the structural response of a panel to vibration by improving its overall damping behaviour, even if they do not make good conventional structural elements.

Maximum Stress

As noted in Section 4.3.1, testing the cells to the point of structural failure raised issues of operator safety, and so the stress required to cause mechanical failure of the cells is still not known. However, a lower bound can be placed on this quantity from the peak value of stress encountered during the sine testing, which was 92.7 kPa. It is unknown how far from failure the cells were at this point, however.

4.3.9 Poisson's Ratio and Compressive Modulus

As noted in Section 4.3.1, a simple sensitivity analysis was conducted to establish whether it was necessary to determine the compressive modulus of the batteries experimentally to produce accurate dynamic models of a sandwich panel.

A sandwich panel was modelled using the Ansys Workbench software package with the attributes shown in Table 4-8, to asses whether the exact value of the compressive modulus of the batteries had to be known, or if simply taking a typical value for Poisson's ratio (and using it to calculate the compressive modulus, using the standard relationship: $E = 2G(1+\nu)$) would be sufficient. An image of the modelled panel, showing the mesh, is shown in Figure 4-31.

Attribute	Value
Panel dimensions	100 mm x 100 mm
Core thickness	10 mm
Facesheet material	1 mm thick aluminium alloy
Core material	PLI Battery

Table 4-8 - Properties of FE model panel

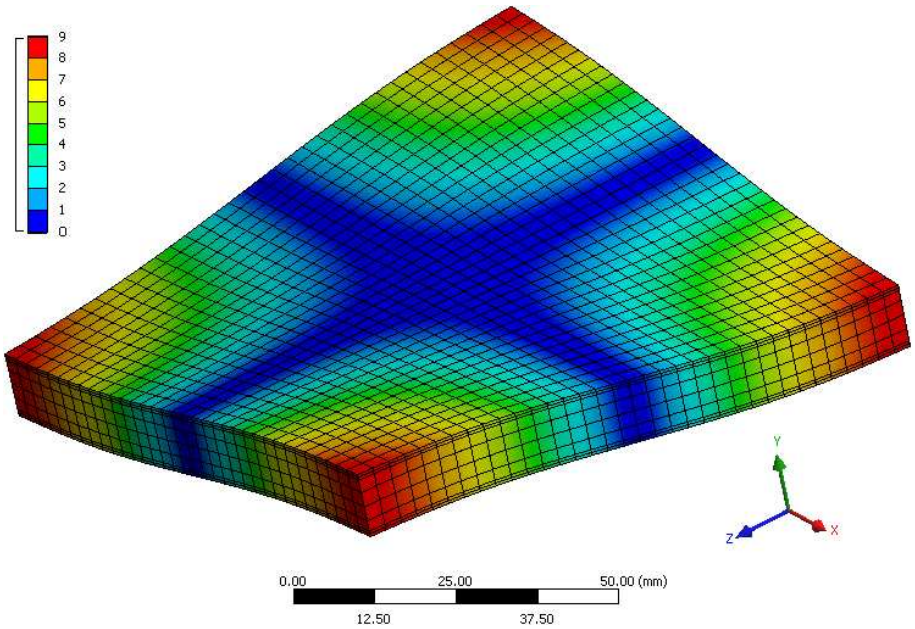

Figure 4-31 - First mode shape and mesh. Scale shows normalised total deformation.

Component	Element type	Number
Core	Solid186 - 20 Node Hexahedral Structural Solid	4624
Facesheets	Shell181 - 4 Node Linear Quadrilateral Shell	2312
Contact	Conta170 and Conta174	4624
Total	**-**	**11560**

Table 4-9 - Elements used in FE model

The shear modulus was fixed at 25 MPa, approximating to the average value displayed during the tests. Poisson's ratio was varied from zero to 0.5. A modal analysis was then run to calculate the natural frequencies of the unsupported panel, with the results shown in Table 4-10.

Result	ν = 0	ν = 0.5	% Difference
Frequency of 1st mode (Hz)	708.62	708.96	0.048
Frequency of 2nd mode (Hz)	1031.4	1032.3	0.087
Frequency of 3rd mode (Hz)	1055.4	1056.4	0.095

Table 4-10 - Results of sensitivity analysis

Given the evidently negligible impact of varying Poisson's ratio on the natural frequencies of the panel, further investigation of this parameter was not considered worthwhile. A value of zero will be used, as this produces the lower (and thus more conservative) result for the natural frequency. This leads to a value of 50 MPa for the compressive modulus.

4.4 Conclusions

The high intensity vibration tests have demonstrated the cells' capability to survive the mechanical environment that a powerstructure would experience. No loss in capacity or increase in internal resistance that could be attributed to vibration was measured after seven tests at 15 g_{rms} and one at 25 g_{rms}, over a total of 18 electrical charge/discharge cycles. This testing indicated that a multifunctional power structure of this type should suffer no degradation in electrical performance from a simulated launch vibration environment.

The most notable conclusion of the mechanical testing is that the mechanical performance of the cells is relatively poor. The cells were found to behave in a highly non-linear fashion, similarly to a softening spring, and there was some indication that the mechanical properties of the cells degraded after they were subjected to loading. However, the fact that they are considerably less stiff than the aluminium honeycomb the replace means that the details of this non-linearity are less important; regardless of the variation of the properties of the cells, their minimal load carrying capacity will make little contribution to the structure. Nevertheless, it is necessary to select an appropriate value of G in order to model the MFS. Given the variability in this quantity that has already been noted, it is difficult to apply a precise value; however, as long as the value chosen is conservative, the resultant models will also be conservative. For the purposes of future FE modelling, a reasonable value will be assumed for the stiffness; the validity of the chosen value can only be assessed after the models have solved.

5 Manufacture, Testing and Modelling of MFS Panels

This chapter will assess the practical implications of employing an MFS based on PLI cells. First among these is the effect the process of manufacturing such a panel will have on electrical performance. The first task, therefore, was to build a multifunctional panel to ensure that there were no obstacles to doing so. The panel was manufactured and the cells within tested to ensure that they continued to function after being exposed to the heat and vacuum of curing, and that no complications occurred in the process.

The second consideration was the panel's response to structural loading. As the purpose of this panel was to investigate the feasibility of the manufacturing process, it was not designed for optimal structural or electrical performance. In order to address the structural performance of an optimised MFS, however, it will be necessary to model their structural behaviour. Testing the response of an experimental subject such as this allows the validity of the FEA models used to model the optimal designs to be assessed, as well as demonstrating that the cells are able to maintain their electrical functionality under real structural loading.

5.1 Panel Design

5.1.1 Material Selection

Facesheets: Carbon Fibre Prepreg

Sandwich panel facesheets for spacecraft structures are typically made from either composite materials – carbon fibre, glass fibre or Aramid fibre reinforced plastic – or aluminium. Carbon fibre (CFRP) provides generally superior structural properties in a space application thanks to its low density and high stiffness, and is becoming a popular option to replace conventional aluminium structures [78]. The two other

composite materials are used in specialised applications, and have inferior properties to CFRP in most situations. On the other hand, aluminium structures are still commonly used in space, as manufacturing and machining composite materials requires specialised equipment. Additionally, aluminium provides protection from radiation, and thus performs the dual function of structural support and radiation protection.

The inferior radiation shielding properties of CFRP structures may, however, be enhanced. In [79,80,81], methods are described that increase significantly the radiation protection afforded by carbon composite structures. The principal of both methods is to increase the average atomic number of atoms in the material and consequentially to improve its ability to absorb ionising radiation.

The multifunctional structure was, therefore, constructed using CFRP facesheets. This allowed the best structural performance to be attained, and given the potential to augment the radiation resistance of the materials, presents no real disadvantage. As noted, the manufacture of CFRP panels is less straightforward than that of aluminium; however, the facilities and equipment required to process composite materials are available in the Transport Systems Research Laboratory at the University of Southampton.

The preferred manufacturing process for carbon fibre composites is autoclave curing of pre-impregnated continuous fibre (prepreg). In this case, the fibre and matrix of the composite are supplied in one unit, and the only processing required is to cut the prepreg to the desired shape and assemble the required number of layers. The choice of resin system is described shortly.

Since such a panel would be loaded in more than one direction, woven prepreg (continuous carbon fibres that are woven into a cloth), with an equal proportion of fibres in the 0 and 90° orientations, is the most straightforward choice of fibre. Woven cloths are easier to handle than unidirectional fibres and perform equally well in

applications that require more isotropic properties. Since the panel was intended simply to prove the manufacturing process, however, it was not designed to meet any particular structural requirements, and so the thickness of the facesheets was not of critical importance. Facesheets of 1-2.5 mm thickness in a quasi-isotropic lay-up (equal proportions of fibres in the -45°, 0°, +45° and 90°) were selected, as this would facilitate handling, and is reasonable for a panel of this size (for details on the layout of the panel, see Section 5.1.2). A prepreg with an areal weight of 600 gm^{-2}, and thus a cured thickness of 0.5-0.6 mm, allows for some flexibility within this range without requiring an excessive number of layers.

Resin System (Prepreg and Adhesive)

For maximal structural performance, a pre-catalysed, elevated temperature curing epoxy adhesive is preferred. The alternative is to use an adhesive that cures at room temperature, though this results in less optimised structural performance. Curing at high temperature, however, presents a problem in this case, as the Varta cells are subject to a strict temperature range for safe and effective operation, as follows [33]:

- 45°C: Maximum rated temperature for recharging.
- 60°C: Maximum rated temperature for storage or discharge.
- 70°C: Maximum safe temperature.
- 85°C: Absolute safety limit (exposure for up to 4 hours presents no safety risk).

Most resin systems cure at 120-150°C or higher, which is clearly unsuitable for this application, as it would not only affect the performance of the cell but would also present a safety risk (leakage of corrosive electrolyte or fire). Initial investigations identified SP Systems' SE70 [82], as potentially usable; however, even the lowest curing temperatures would cause damage to the cell, and even a small excursion in

temperature due to poor calibration or malfunction of instruments could result in safety issues.

Further searching identified the -44 resin series, produced by Amber Composites. This resin can cure at temperatures as low as 50°C, though this curing cycle takes 18 hours. This is deemed acceptable, as it leaves a margin of 10°C before the temperature exceeds the manufacturer's recommended maximum for storage of the cell.

The resin is available as both an adhesive film (EF44 [83]) and a prepreg matrix with a variety of reinforcing fibres (E644 [84]). EF44 was the natural choice as an adhesive film, since there is no other readily available pre-catalysed resin system that can be used with the batteries. It would have been possible to use a different system for the facesheets, since they were cured separately; however, E644 was chosen since it allowed for some flexibility, should an alternative manufacturing method be adopted in the future. In any case, the performance and cost of the E644 prepreg are similar to higher-temperature curing composites, with the exception that they have a lower glass transition temperature if not post-cured. However, since high temperatures would damage the batteries in any case, this is not an issue. The carbon cloth adopted used a 2-2 twill* weave pattern with 12000 filaments per tow, leading to an areal weight of 650 gm^{-2}.

Core: Aluminium Honeycomb

Three principal materials may be considered for use as core materials in spacecraft sandwich structures, all in a honeycomb configuration [85]. Fibreglass is useful thanks to it being a good electrical and thermal insulator, and Nomex honeycomb is highly tolerant of damage. However, as the most common design driver for structures is the launch vibration environment, aluminium is the preferred material as it produces panels with the highest stiffness to mass ratio and thus the best dynamic structural

* Information on weave types is available online at: www.azom.com/

behaviour (although the density of Nomex is lower, the stiffness of aluminium honeycomb is an order of magnitude higher). Another factor affecting this decision was the fact that aluminium and carbon form a galvanic cell in the presence of humidity, causing corrosion. However, given that this panel was simply a proof of concept, and that moisture is not a problem commonly encountered by spacecraft, this effect was neglected. In practice, a thin layer of glass fibre would be used to insulate the two materials from each other, or a less chemically active core material (titanium, for example) would be used.

Since the aim of this work is to produce a generic structural panel in order to demonstrate the feasibility of a concept, aluminium honeycomb was used as the core material in conjunction with the Varta PoLiFlex PLF 263441 cells, used for vibration testing in Section 4.2. As noted previously, these cells have high specific energy capacity and a surplus was available form the original vibration testing.

Amongst the most important considerations in this case is availability, since honeycomb is not commonly available in thicknesses as low as 2.6 mm. The only supplier found in the UK that could supply 2.6 mm thick honeycomb was Amber Composites, which sells aerospace- and commercial-grade hexagonal cell aluminium honeycomb at thicknesses down to 2 mm. This being established, it was necessary to define the other specifications of the honeycomb, namely the cell size and foil thickness; however, given that the primary purpose of manufacturing the panel was related to the manufacturing process and not the end product, the precise attributes of the core were unimportant. The decision was based on availability, and the chosen core was AAC-5.2-1/4-25P-5052 [86]. This material has a cell size of 0.25" (6.35 mm) and a foil thickness of 6.35 μm, giving it a density of 83.2 kgm^{-3}, these being typical attributes for a spacecraft sandwich panel core.

5.1.2 Panel Layout

To produce a test case of a realistic application, the panel was designed to conform to a standard SSTL electronics tray. Its dimensions and the layout of inserts for fixing points are shown in Figure 5-1. Two plies of the 600 gm^{-2} EF644 carbon fibre/epoxy prepreg were used per facesheet, with an even mix of 0-90° and ±45° plies, as shown in Figure 5-2, resulting in a quasi-isotropic material.

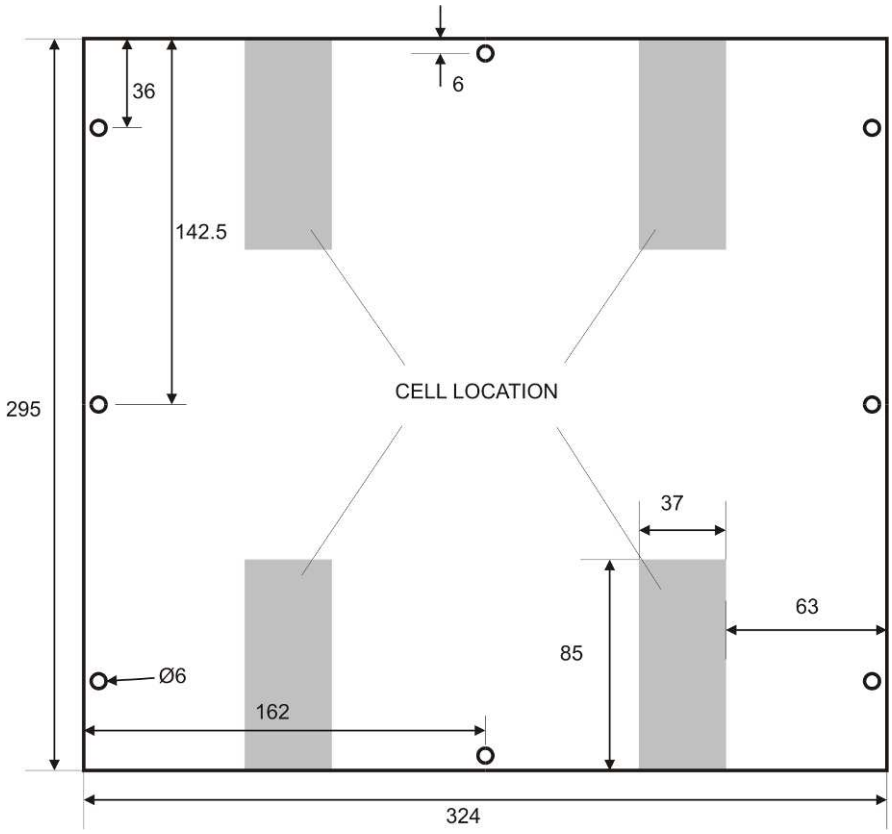

Figure 5-1 - Panel layout

±45º
0-90º
CORE
0-90º
±45º

Figure 5-2 - Panel lay-up

The batteries are placed in groups of two at the edges of the panel as indicated in Figure 5-1. This location was chosen primarily for ease of wiring access to the cells, rather than for optimised structural performance, since this initial panel is intended primarily to prove the manufacturing technique. However, from a "rule of thumb" standpoint, the impact of the batteries on the structure may be assumed small if the panel is restrained by the inserts; the mass and stiffness they add would have the greatest effect at the centre or supports of the panel and least around its edge.

5.2 Manufacturing

The manufacturing process followed that used for a conventional panel in most respects, using vacuum bagging and an unpressurised oven to cure the facesheets. The same method was subsequently used to cure the adhesive that attaches the core, batteries and inserts to the facesheets. The major points of the manufacturing process are described in this section; Appendix II covers this subject in more detail.

5.2.1 Facesheets

The preferred method to process prepreg composites is using a vacuum bag and autoclave. The high pressure of the autoclave results in minimal voiding and excellent resin consolidation. However, adequate results can be achieved using a vacuum bag and unpressurised oven if the resin flow is good [85], and this method was used for the manufacturing of the MFS panel.

After being cut to size, the prepreg is covered in a layer of peel ply, a fabric that is permeable to resin but does not adhere to the cured material. This, in turn, is covered by a layer of release film, that limits the flow of resin, and finally a layer of fleece-like breather, which provides a permeable air path from the vacuum pump to the entire panel. These materials are shown in Figure 5-3.

The materials are now vacuum bagged by sealing a piece of vacuum film over the plate, leaving a breach valve passing through the film. The plate is then placed into the oven and connected to the vacuum pump. If the seal of the bag is adequate, the oven is programmed with the appropriate curing cycle. The plate is shown in the oven, connected to the vacuum pump, in Figure 5-4.

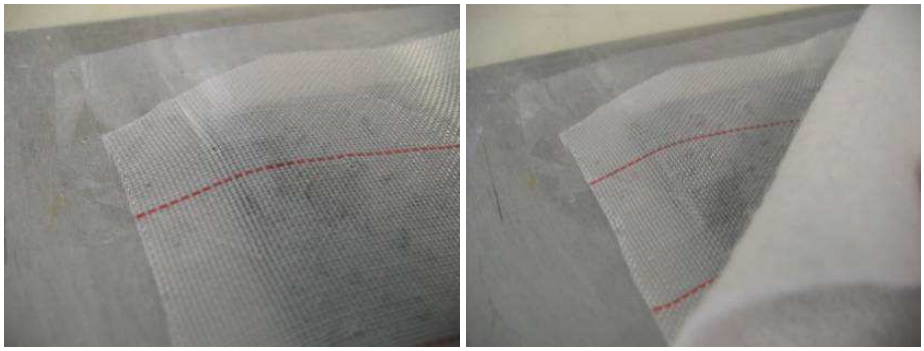

Figure 5-3 - Peel ply, release film (L) and breather (R)

Figure 5-4 - The plate in the curing oven under vacuum

5.2.2 Sandwich Panel Assembly

The complete sandwich panel consisted of the following components: two CFRP facesheets, two pieces of resin adhesive film, eight aluminium inserts for fixing points,

eight batteries plus wires and a sheet of aluminium honeycomb. The assembly of these components into a sandwich panel is described in this section.

The first task was to cut the two facesheets to the correct size using a diamond edged circular saw. Next, the honeycomb and adhesive were cut to fit the facesheets, both being cut with a knife or with normal scissors. A cardboard template was used to cut gaps in the honeycomb for the batteries and inserts. The batteries and inserts were then placed onto a sheet of adhesive (located using the cardboard template), which was in turn placed on one of the facesheets. To prevent electrical shorts, any bare metal on the batteries was covered in insulating tape. Next, the honeycomb was put in place, and strips of the adhesive film used to bond it to the batteries and inserts. Finally, the second layer of adhesive and facesheet were put in place.

Strips of peel ply were attached to the perimeter of the panel using adhesive tape, and the entire panel was wrapped in breather. Finally, the panel was vacuum bagged as described previously and placed in the oven (shown in Figure 5-5). The curing cycle used at this stage was 50°C for 16 hours; the completed panel is shown in Figure 5-6.

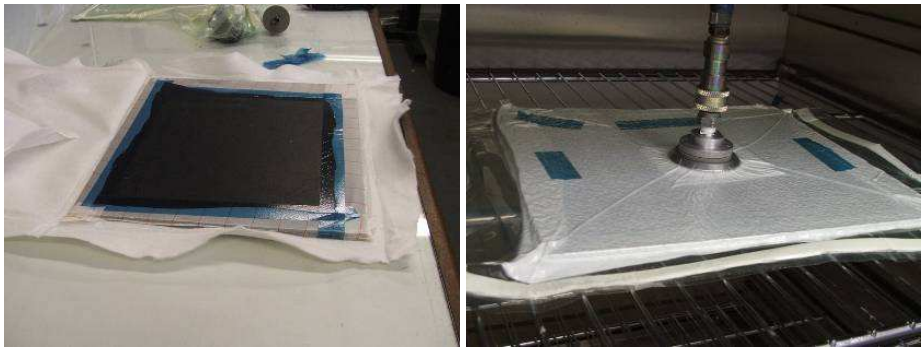

Figure 5-5 - Panel with peel ply (L) and vacuum bagged in the oven (R)

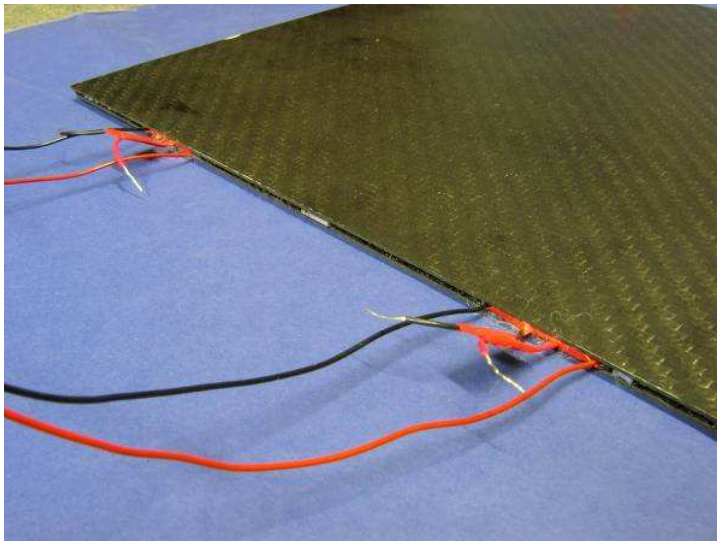

Figure 5-6 - The multifunctional panel

5.3 Effect on Electrical Performance

The heat and vacuum applied to the cells within the panel may have affected their performance. To test this, four of the eight cells were characterised before manufacture, then tested again afterwards. R_{INT} was found to increase by roughly 10%, and a slight decrease in V_{EOD}, roughly 5%, occurred. During the period between the two tests, some degradation was observed in a control specimen, so this effect may be due to aging or self-discharge. The effect does not appear to be sufficient to affect the performance of the powerstructure significantly, however, and the cells did survive the environment without failure.

5.4 Structural Performance

Structural tests were carried out on the MFS panel to ensure that FEA models made subsequently would produce reliable results. The tests also allowed the cells' ability to survive within a loaded MFS to be confirmed. To achieve this, the MFS panel was vibrated using an electrodynamic shaker, and the experimental results were compared to an FE model of the panel under vibration.

5.4.1 Material Properties

In order to produce an FE model of the panel, the mechanical properties of the materials used in it had to be known. For the aluminium honeycomb, the manufacturer's data was used, whilst, for the batteries, the data collected experimentally (see Section 4.3) was available. For the EF644 CFRP face sheets, however, no reliable data was available, and so it was necessary to obtain the properties of the carbon fibre composite experimentally. Two separate dynamic tests were conducted to establish the CFRP's bending modulus.

The first test compared the modes of a sheet of CFRP to standard analytical equations. For this test, a sample of the material was fixed to an electrodynamic shaker, clamped in the cantilevered configuration shown in Figure 5-7. It was then subjected to a vertical sine test (10-500 Hz at 0.1 g) in order to identify its modes of vibration. Readings were taken using three PCB Piezotronics 352A21 accelerometers, whilst an Endevco 2256-100 was used as the control channel. The length of the facesheet outside of the clamp was 324 mm and its width was 303 mm. The cured thickness of the material was 2.38 mm, consisting of four layers of prepreg in a balanced, quasi-isotropic lay-up as shown in Figure 5-8.

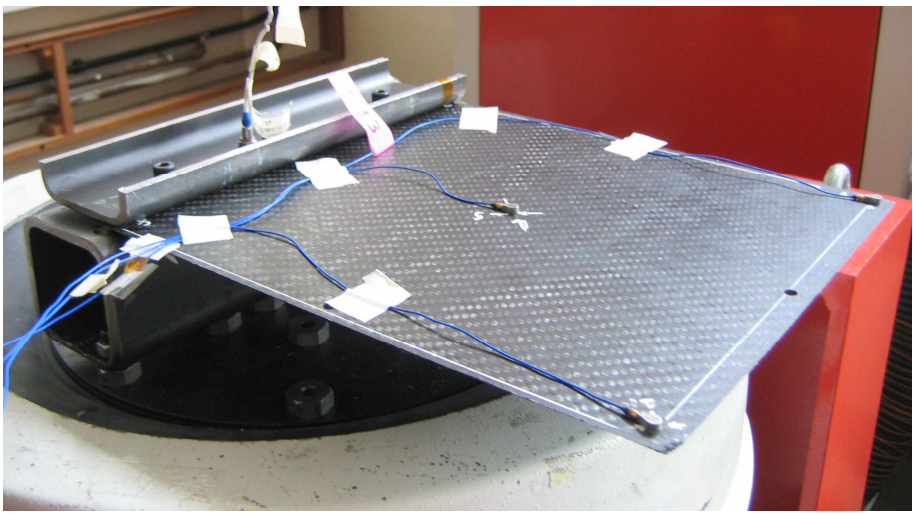

Figure 5-7 - Test set up for facesheet characterisation test

0-90º
±45º
±45º
0-90º

Figure 5-8 - Facesheet lay-up

The 2D modes of the panel in this arrangement are effectively the same as those of a cantilevered beam, and thus analytical equations [87] for the natural frequencies for such a structure may be applied, as in (5-1).

$$f_n = \frac{K_n}{\pi L^2}\sqrt{\frac{EI}{\rho A}} \tag{5-1}$$

In this equation, f_n is the frequency of the nth mode of vibration, K_n is a constant associated with that mode, L is the effective length of the beam, E is the bending modulus (which is the unknown in this case), I is the second moment of area, ρ is the material density and A is the beam's cross-sectional area. The values of K_n for the first three modes are 1.758, 11.015 and 30.85 respectively.

Performing a sine sweep on the panel identified the first three natural frequencies of the type required (i.e., those following 2D beam mode shapes) at 20.6, 135 and 368 Hz, which, combined with a density of 1600 kgm^{-3} and the dimensions given above, lead to values of 50.5, 55.2 and 52.3 GPa for the bending stiffness. Using the first value, 50.5 GPa, in an FE model gives the results shown in Table 5-1. This model was a modal analysis, using Ansys Workbench. 1978 Shell181 (4-Node Linear Quadrilateral Shell) elements were used.

Result	Experiment	FE model	% Difference
Frequency of 1st mode (Hz)	20.6	20.6	0.00%
Frequency of 2nd mode (Hz)	135	129	-4.44%
Frequency of 3rd mode (Hz)	368	362.5	-1.49%

Table 5-1 - FE mode results for cantilevered characterisation test

These results were then compared to a less-constrained dynamic impact hammer test. The same sample as above was simply supported at two points (the midpoints of two adjacent edges, as indicated in Figure 5-10) using fishing line, and otherwise allowed to hang freely. The full length of the panel was 340 mm, and its width and thickness 303 and 2.38 mm respectively. The dynamic response was measured by tapping with an impact hammer and measuring the panel's response with an accelerometer. The result was compared to an FE model using the stiffness as calculated above. A chart of the response of corner 2 of the panel to a tap at corner 4 (as defined in Figure 5-10) is shown in Figure 5-9. Although the signal is somewhat noisy, the first peak is clear and located at 58.0 Hz.

The mesh of the FE model, which was created using the Ansys Workbench package, is shown in Figure 5-10; all 1020 elements are Shell181 (4-Node Linear Quadrilateral Shell). The support was modelled by constraining the nodes indicated in the figure in translation, leaving them free to rotate.

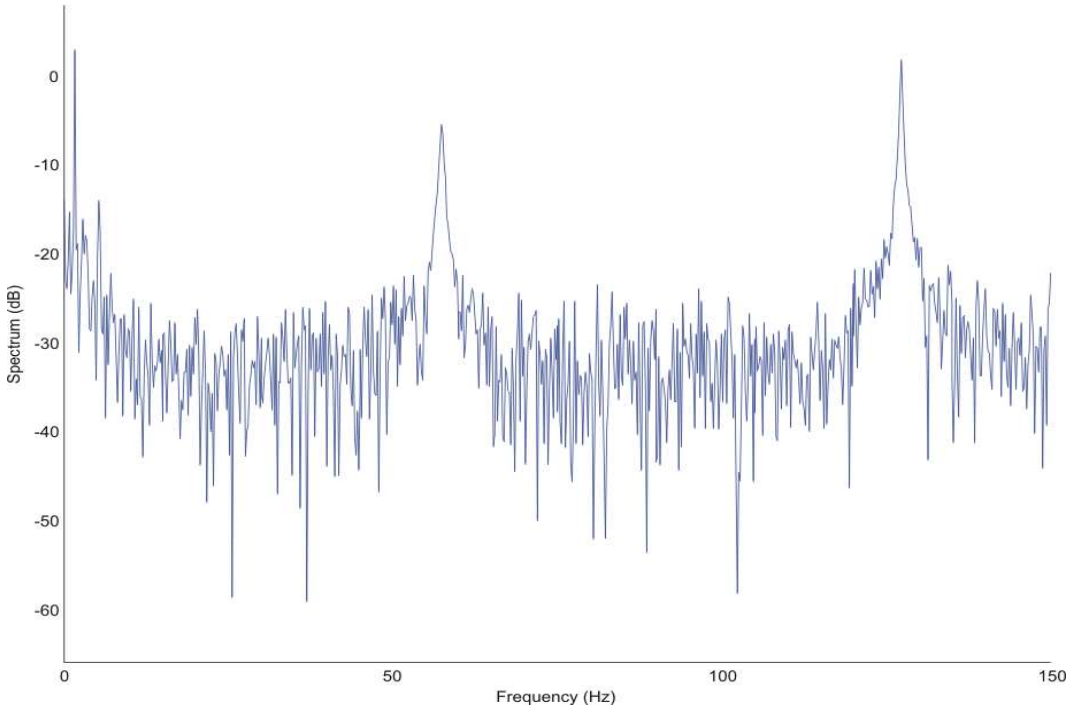

Figure 5-9 - Dynamic response of panel

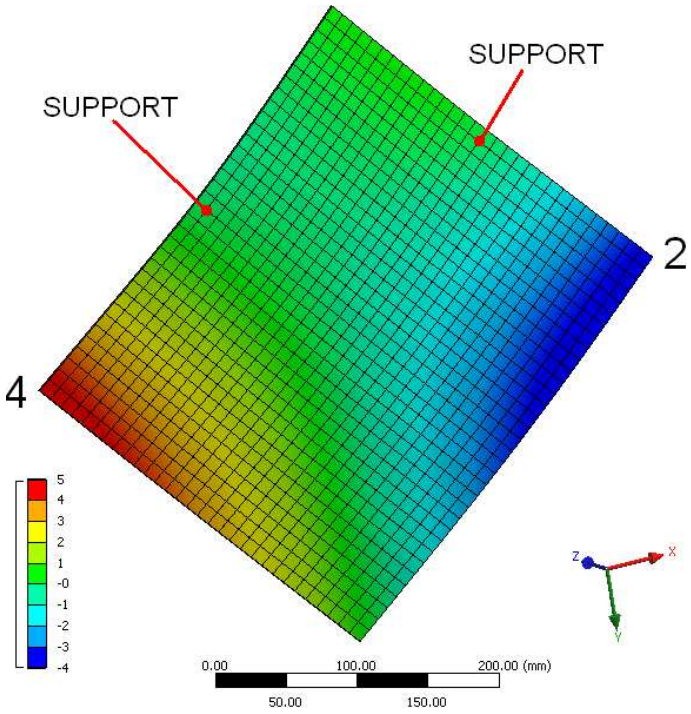

Figure 5-10 - FE results for 1st mode.

Scale shows normalised deformation in Z direction (i.e., normal to panel). Positive displacements are out of the page.

Figure 5-10 also shows the results of a modal analysis of the facesheet's first mode of vibration when simply supported as during the experiment. Tuning the value of the stiffness to the measured natural frequency suggests a slightly lower stiffness than determined using the other tests; a value of 50 rather than 50.5 GPa for the modulus results in a natural frequency of 58.1 Hz for the FEA model.

The impact hammer testing supports the experimental results from the test using the shaker, with the difference from the lowest value, 50.5 GPa, being only 1%. Given that the testing on the shaker is representative of the conditions the MFS panel will be subjected to, and noting the excellent agreement between the experiment, analytical result and FE model, these material properties were used. The modulus calculated from the 1st mode, 50.5 GPa, was used, as the 1st mode is of greatest importance to the overall response, and this value was the lower and thus more conservative result.

5.4.2 Experimental Procedure

For testing, the panel was not restrained using the inserts; instead, it was clamped at one end, the clamp in turn being fixed to the head of a vertical shaker, as for the material characterisation tests described in the last section. Although this was less representative of the type of support arrangement such a panel would have during a real spacecraft launch, for these experiments, it had three advantages. Firstly, it was considerably simpler to implement, requiring no modifications to the panel (such as drilling) or the manufacture of a separate mounting device. Secondly, it subjected the two groups of cells in the panel to varying levels of mechanical loading, allowing comparisons to be made of the effect (if any) of vibration and stress on the batteries' electrical performance. Finally, this is a comparatively harsh condition, meaning that any results regarding the survival of the cells and the structure s a whole should be conservative. The experimental setup is shown in Figure 5-11.

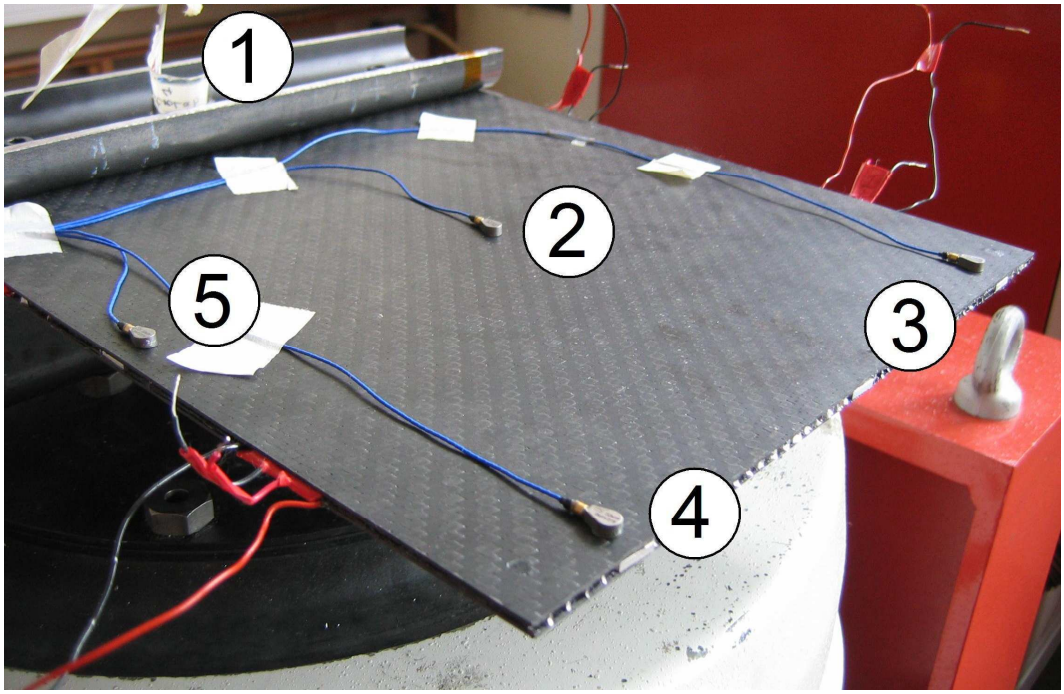

Figure 5-11 - Experimental setup showing positions of accelerometers

The panel was initially subjected to a low-level sine test, and then to random vibration tests of increasing magnitude. The highest-level test had a total acceleration of 7 g_{rms}, this lower level being used as the cantilevered support resulted in a large amplification (over 10 times at the tip of the panel). All the tests used similar profile shapes to that shown in Figure 4-7. The response was measured by four PCB Piezotronics 352A21 accelerometers, fixed in place using beeswax, and the control channel for the shaker was a single Endevco 2256-100 superglued to the clamp. The locations of the accelerometers are shown in Figure 5-11. Since the aim of the tests was simply to provide an approximate comparison between the FE models and a real panel, the accelerometer positions were not measured precisely. All data were sampled at 2500 Hz, using an average from ten 2-second samples. Due to the nature of the data acquisition system, no time history data was available from the testing.

5.4.3 Experimental Results

Electrically, no effect on the cells' voltages was observed after 5 and 7 g_{rms} vibration for 5 minutes, which would have subjected the outer batteries to acceleration of the order of 50-70 g_{rms}. Full electrical characterisation was not carried out but the cells continued to function without any sign of degradation.

The structural response of the panel to a 5.26 g_{rms} random vibration input is shown in Figure 5-12 along with the control input (Channel 1). Channel 3 closely followed channel 4 in shape, whilst channels 2 and 5 showed a broadly similar response at a lower level. The first resonant frequency occurred at 44.5 Hz and the total acceleration running on each channel is shown in Table 5-2. There is a significant acceleration response up to 1500 Hz, beyond which there is no notable contribution to the total response, as shown in Figure 5-13.

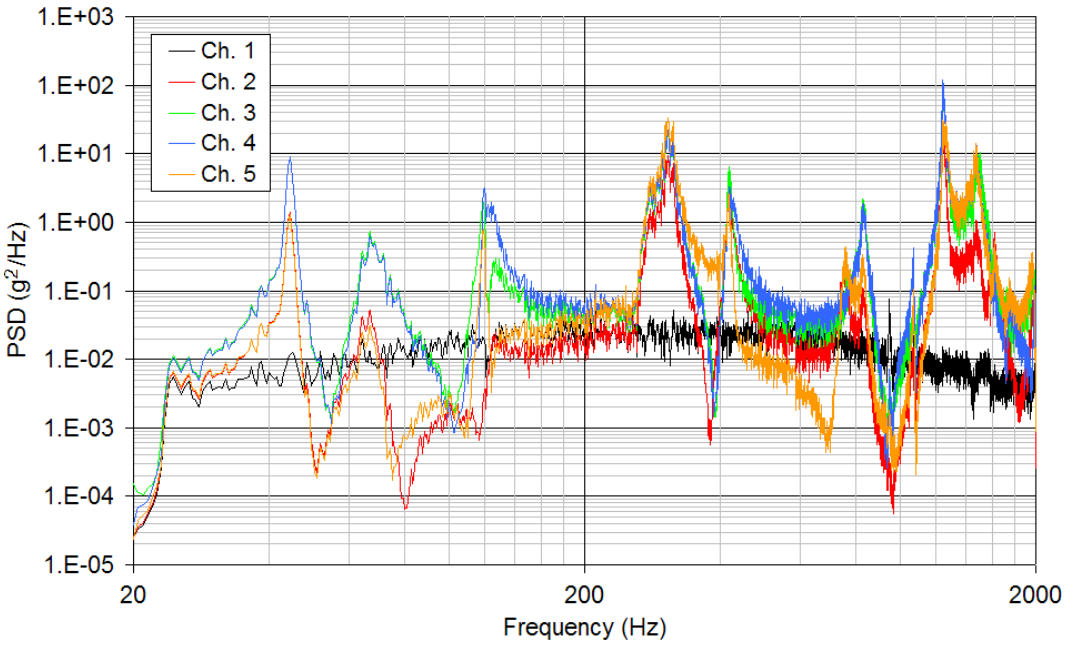

Figure 5-12 - Response of panel to random vibration

Channel	Total acceleration
1 (ctrl.)	5.26 g_{rms}
2	27.2 g_{rms}
3	54.9 g_{rms}
4	56.4 g_{rms}
5	47.4 g_{rms}

Table 5-2 - Total g_{rms} acceleration on all five channels

Figure 5-13 shows that, for acceleration, the first mode was less important, with the majority of the response being due to higher modes around 300 and 1250 Hz. However, the calculated root-mean-squared deformation, as shown in Figure 5-14, was almost entirely due to the first mode, with over 90% of the total deformation accounted for by 50 Hz on all four channels. Figure 5-13 was produced by summing the measured PSD; Figure 5-14 was generated by integrating the data twice with respect to frequency to calculate the PSD deformation, then summing this in turn.

It is of note that, while the vast majority of the deformation was accounted for by the first mode of vibration, this is not true of the acceleration. In fact, less than 10% of the acceleration response is due to the first mode, which is a rather unexpected result and may indicate that some aspect of the experimental setup allowed the panel to respond excessively at high frequencies.

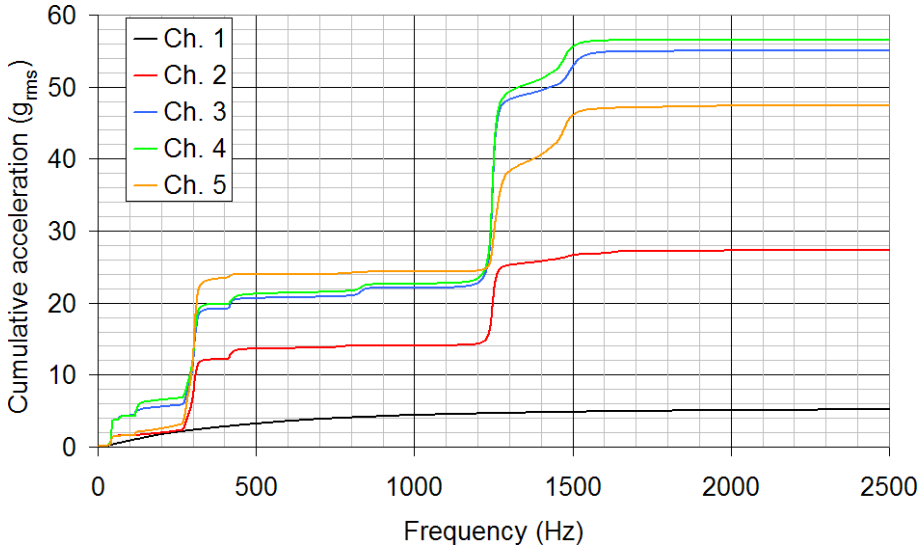

Figure 5-13 - Cumulative acceleration vs. frequency for channels 2-5

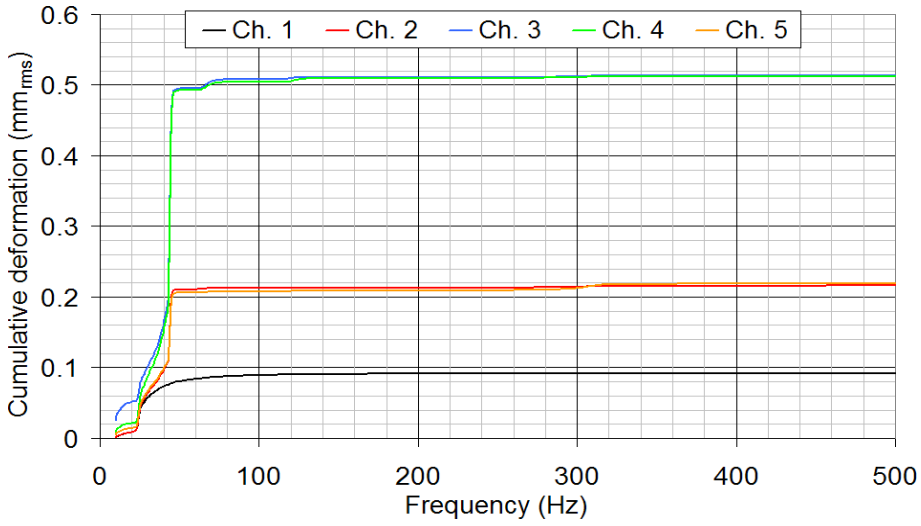

Figure 5-14 - Cumulative deformation up to 500 Hz (beyond this, deformation is negligible)

5.4.4 Finite Element Models

The panel was modelled using a 5 mm mesh, with 2.6 mm through the thickness of the core. The details of the elements used are shown in Table 5-3. The material properties used for the CFRP facesheets and cells are as calculated previously; the honeycomb properties are as given in Table 5-4 (these values are from the manufacturer's datasheet, with the exception of G_{xz} and $E_{x,y}$, which are assumed values required for the FE model). The clamp was represented by applying a fixed support (rotation and translation) constraint over an area extending 25 mm from one short edge of the panel, as indicated in Figure 5-15. A detail of the meshed model (with one facesheet omitted) is shown in Figure 5-16.

Frequency range	**Experiment**	**Number**
Facesheets	Shell181 - 4-Node Linear Quadrilateral Shell	7670
Honeycomb	Solid186 - 20 Node Quadratic Hexahedron	3593
Cells	Solid186 - 20 Node Quadratic Hexahedron	544
Inserts	Solid186 - 20 Node Quadratic Hexahedron	955
Contact	Conta174 and Targe170	81494
Total	-	**93386**

Table 5-3 - Elements used in panel model

Attribute	**Value**
Thickness	2.6 mm
Compressive modulus out of plane (E_z)	965 MPa
Compressive modulus in plane ($E_{x,y}$)	100 MPa
Shear modulus out of plane (G_{xz})	55 MPa
Shear modulus out of plane (G_{xz})	207 MPa
Shear modulus in plane (G_{xy})	487 MPa
Density	83.3 kgm^{-3}

Table 5-4 - Honeycomb material properties. Axes as defined in Figure 5-15.

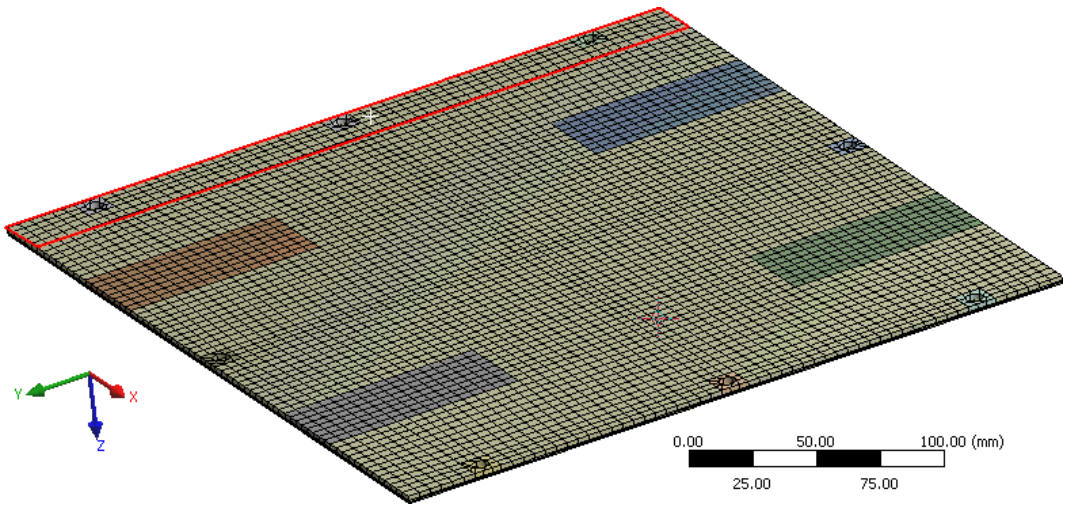

Figure 5-15 - Mesh of experimental panel model. Red-bordered area shows area of support.

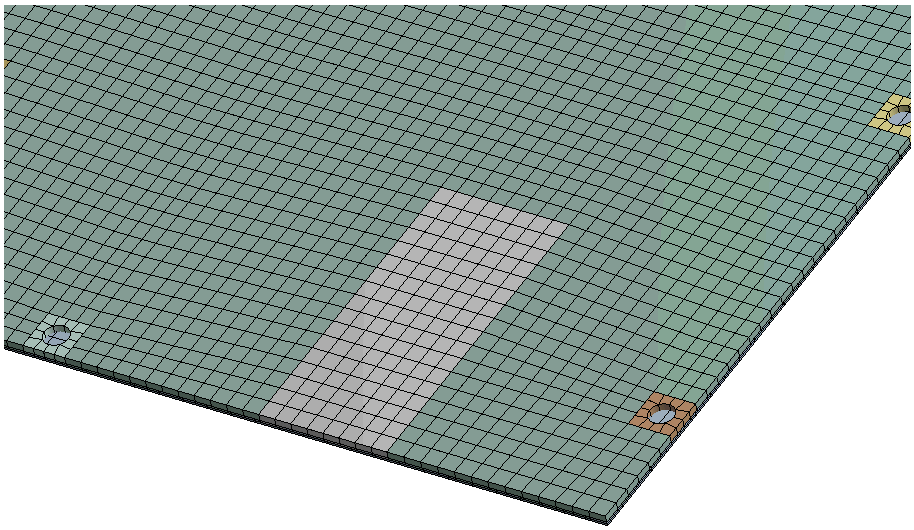

Figure 5-16 - Experimental panel mesh detail

5.4.5 FE Results and Comparison

The FE model predicted the first mode of vibration at 42.9 Hz, a difference of less than 4% from the experimental result. The mode shape is shown in Figure 5-17. The higher modes differed somewhat from the experimental results, but the significant modes were within 10-15% up to 1000 Hz.

Taking a value for the damping coefficient of 3%, which is typical for a sandwich panel, a random vibration FE analysis using the same input profile as the experiment predicts the deformations shown in Table 5-5. These results give a good match across the panel, with virtually the entire response being due to the first mode, as expected.

Channel	Experiment	FE model	Difference
2	0.22 mm	0.19 mm	-14%
3	0.51 mm	0.54 mm	+6%
4	0.51 mm	0.54 mm	+6%
5	0.22 mm	0.18 mm	-18%

Table 5-5 - Comparison of deformation results from FE model and experiment

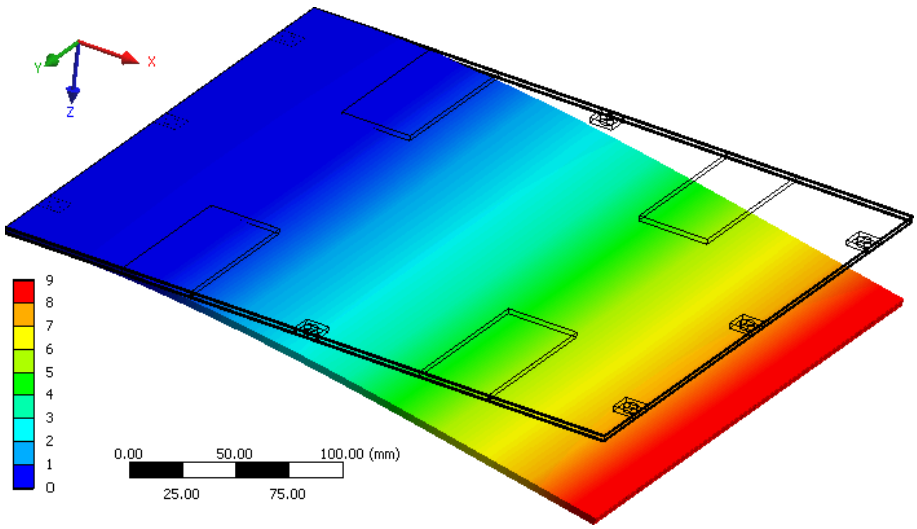

Figure 5-17 - 1st mode of panel at 42.9 Hz. Scale shows normalised deformation.

Retaining the 3% constant damping ratio, the first mode prediction gives a good match to the experimental acceleration data. However, as noted previously, the first mode did not contribute significantly to the overall acceleration in the experimental results. The predicted and measured acceleration responses from the first mode are shown in Table 5-6.

Channel	Experiment	FE model	Difference
2	1.53 g_{rms}	1.41 g_{rms}	-8%
3	3.77 g_{rms}	4.00 g_{rms}	+0.8%
4	3.78 g_{rms}	4.00 g_{rms}	+0.5%
5	1.49 g_{rms}	1.33 g_{rms}	-11%

Table 5-6 - Comparison of acceleration results from FE and experiment (1st mode)

The next acceleration response from the panel occurs at 120 Hz, where the acceleration measured on channels 3, 4 and 5 increases slightly. This is not a large increase, but is remarked upon as it appears to occur due to an asymmetric twisting mode of the panel, corresponding to a mode shape predicted at 106 Hz by the FE model. This mode is shown in Figure 5-18.

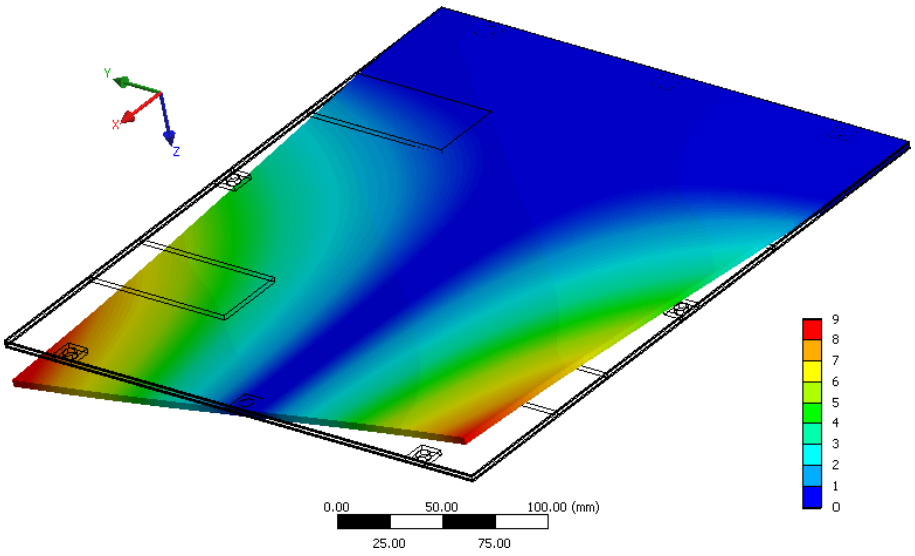

Figure 5-18 - 2nd mode predicted by FE model. Scale shows normalised deformation.

The measured response at this frequency in the experiment is not great. An increase of 1.1 and 2.1 g_{rms} occurred on channels 3 and 4 respectively, and channel 5 increased by 0.76 g_{rms} (the lack of response from channel 2 also suggests this mode shape, as the centre of the panel should not be affected). What is significant is that a seemingly asymmetric mode has been excited by a symmetric acceleration field, suggesting that asymmetry of the panel or its restraint may have affected the results elsewhere.

Two regions of the frequency range are responsible for the majority of the acceleration measured in the experimental data. These occur at around 250-350 Hz and 1200-1500 Hz, as shown in Figure 5-13.

Comparing this with the FE results at the first point, the model predicts the third and fourth modes at 263 and 331 Hz, which are both symmetric and which correspond fairly well with the broad peak shown between 280 and 320 Hz in Figure 5-12. However, as Figure 5-20 shows, the majority of the acceleration predicted by the FE model in this range is due to the 263 Hz mode shape. This indicates that either the frequency of the 3rd mode has been under-predicted significantly, or the fifth mode (an asymmetric twisting mode) was excited in addition to the symmetric modes.

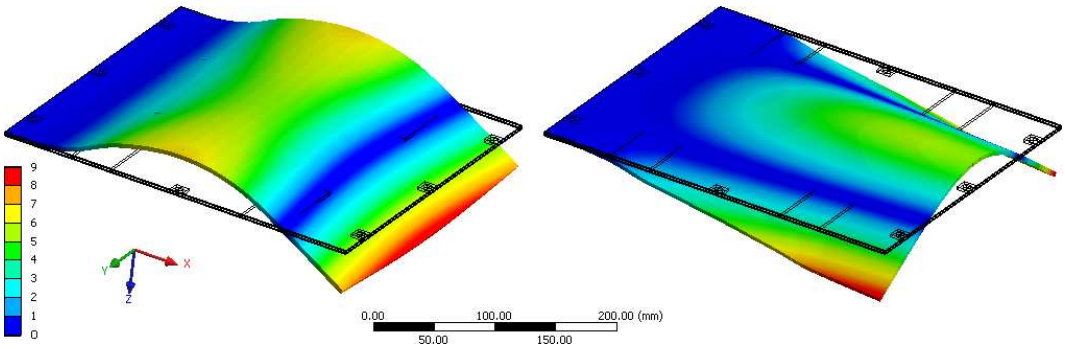

Figure 5-19 - Modes at 263 Hz (L) and 331 Hz (R). Scale shows normalised deformation

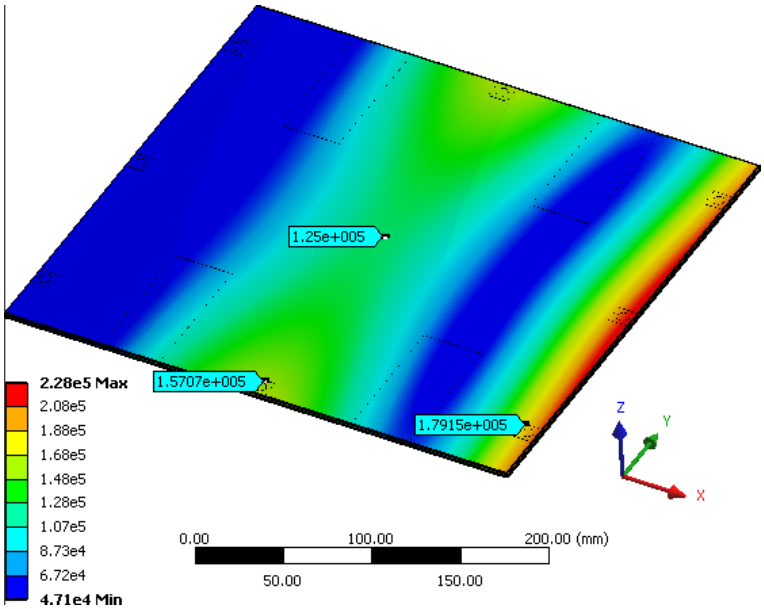

Figure 5-20 - Acceleration response from 200 to 500 Hz. Scale in mms^{-2}.
Note that this graphic shows the absolute acceleration, including the input at all frequencies.
To compare with Figure 5-13, the input from 0-200 Hz and 500-2000 Hz was subtracted.

The FE model's predicted acceleration on channels 2, 3 and 4 gives an acceptable match to the experiment if a damping coefficient of 1% is used, rather than the 3% used previously. Even with this lower damping coefficient, however, the FE prediction for channel 5 under-predicts the experiment somewhat. The results of the FE model and experiment are shown in Table 5-7.

Channel	Experiment	FE model	Difference
2	11.4 g_{rms}	9.21 g_{rms}	-21.1%
3	14.9 g_{rms}	14.71 g_{rms}	-2.4%
4	14.5 g_{rms}	14.71 g_{rms}	0.0%
5	20.9 g_{rms}	12.47 g_{rms}	-42%

Table 5-7 - Comparison of cumulative acceleration results from 2-500 Hz

Beyond 500 Hz, the correspondence between the FE model and the experiment is poorer for acceleration. Between 500 and 1000 Hz, both the experiment and FE model showed negligible acceleration response. The next jump in acceleration occurred

between 1200 and 1500 Hz in the experimental results, and so the results from 1000 to 2000 Hz are compared. Given the complex response of the experimental panel in this region, no attempt has been made to identify which particular mode or modes account for the majority of the response.

The distribution of acceleration across the panel is shown in Figure 5-21, and the results for the four measurement positions are given in Table 5-8. As can be seen, the FE model predictions are significantly lower than the experimental results in this high-frequency region.

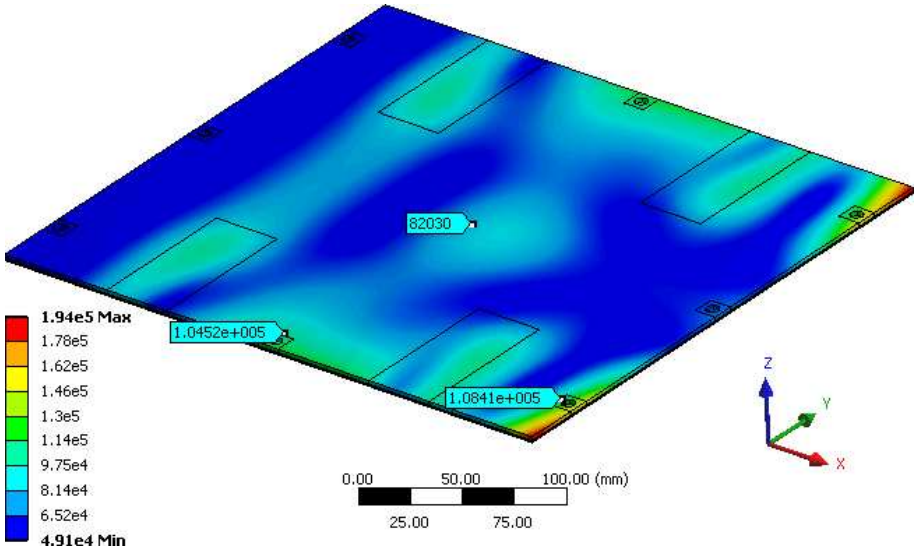

Figure 5-21 - Acceleration response from 1000 to 2000 Hz. Scale in mms^{-2}.
Note that this graphic shows the absolute acceleration, including the input at all frequencies.
To compare with Figure 5-13, the input from 0-1000 Hz was subtracted.

Channel	Experiment	FE model	Difference
2	13.2 g_{rms}	4.23 g_{rms}	-68%
3	33.0 g_{rms}	6.88 g_{rms}	-79%
4	34.0 g_{rms}	6.88 g_{rms}	-78%
5	23.1 g_{rms}	6.47 g_{rms}	-72%

Table 5-8 - Comparison of cumulative acceleration results from 1-2000 Hz

5.4.6 Observations

The correspondence of the deformation results for the finite element and experimental cases is promising, as the deformation of the panel also determines the structural stress within it. The stress in the panel was not measured directly, but the fact that the FE model can predict the deformation of an MFS panel also means that the stress predictions should be equally accurate. Whilst the results predicted by the FE model are not of sufficient accuracy to predict the behaviour of a real panel in great detail, due to the approximation used for the damping coefficient, the fact that the main use of the models is to compare similar panels to one another makes this less relevant. A slight modification of this parameter for every model would not alter the differences between them.

Modelling of the acceleration response at low frequencies produced acceptable results, though a lower damping coefficient was required. The nature of the support arrangement and/or the asymmetry of the panel meant that, whilst the panel was properly clamped and responded symmetrically at low frequencies, higher frequency modelling was less reliable. This problem would have been compounded by the limitations of the FE method when modelling high-frequency vibrations. Time constraints, and a lack of raw data from the equipment used, made further investigations of the panel's behaviour impractical.

5.5 Conclusions

PLI cells have demonstrated that they continued to function during the manufacturing of the powerstructure, though the process caused a small loss in performance. This slight performance loss, coupled with the poor structural properties of the cells presented in Section 4.3, suggests that cold-bonding would be a better choice if permitted by the design of the panel in question; however, the tests showed that, if required, cells can be incorporated into a panel even if they must be in place during the curing process.

The dynamic testing on the completed panel assessed the reliability of an FE model of a multifunctional structure of this type. Such models can be relied upon to produce acceptable predictions of the panel's deformation and stress level, though prediction of the acceleration was found to be less reliable. In addition, the cells further demonstrated their ability to retain electrical function when subjected to vibrations.

6 Structural Performance of MFS Panels

Having completed this experimental work, the final task was to establish how successfully the MFS concept would reduce the mass of the spacecraft. To this end, a generic structure was designed, and then modified to incorporate PLI cells, thus producing a multifunctional structure design. By varying the number and layout of the cells within the panel and then running FE models of the resultant panels, it was possible to select the designs with the best structural performance.

This trade-off was conducted in two stages: firstly, the majority of panel designs were eliminated using a modal analysis. The second step was more computationally expensive and consisted of modelling the response of the remaining designs to random vibration, and selecting the best designs on this basis. Comparing their performance to that of the original panel and referring to the parametric study in Chapter 3 allows the overall effect of this type of MFS on the spacecraft to be assessed.

6.1 Structural Design

6.1.1 Shear Modulus of Batteries

As shown in Section 4.3 the shear modulus, *G*, displayed by the batteries varies according to the level of stress to which they are subjected. In order to produce models, it was necessary to assume a value for this quantity. Since the stiffness of the cells was, even at its highest value, measured to be much lower than the stiffness of the surrounding honeycomb core (54.1 MPa, the best value for the cells, compared to 500 MPa for the honeycomb), and they will replace only a small proportion of the core, their structural contribution is fairly small. Thus, it was assumed that the effect of the precise value of the stiffness on the overall behaviour of the panel would be small, and the value chosen was 25 MPa, which is slightly less than half the highest measured value. The validity of this assumption was tested by calculating the level of

shear stress in the cells: by comparing this quantity to Figure 4-27, it was established whether the measured shear stress should be higher or lower and, if appropriate, the model was re-evaluated using a more conservative value.

6.1.2 Configuration

Rather than modelling a specific panel configuration, such as that described in Chapter 4, a generic square panel was chosen for this study. The panel modelled was a 500 mm square sandwich panel with a 20 mm cube insert at each corner. A panel of this size could represent a principal structural component of a mini- or microsatellite, or an internal shear panel or mounting "shelf" in a larger craft.

The attributes of the materials used in the panel are shown in Table 6-1 and Table 6-2. Note that the out-of-plane shear moduli of the honeycomb core are averaged: in practice the values of G_{xz} and G_{yz} will differ somewhat, but for the purposes of modelling this generic structure, they are treated as being equal. Also, the values of $E_{x,y}$ and G_{xy} are simply required for the creation of the FE model; if they were less than one tenth of E_z and $G_{xz,yz}$ respectively, the software would return an error, but these properties do not have any bearing on the performance of the structure, nor are they representative of a real honeycomb core.

Attribute	Value
Thickness	1 mm
Modulus of elasticity	75 GPa
Poisson's ratio	0.05
Density	1600 kgm^{-3}

Table 6-1 - Facesheet and insert material properties

Attribute	Value
Thickness	20 mm
Compressive modulus out of plane (E_z)	1775 MPa
Compressive modulus in plane ($E_{x,y}$)	180 MPa
Shear modulus out of plane ($G_{xz,yz}$)	500 MPa
Shear modulus in plane (G_{xy})	50 MPa
Density	100 kgm^{-3}

Table 6-2 - Core material properties

In order to consider a variety of panel designs for optimisation without the need for excessive modelling, a series of constraints was placed on the design of the panel. The process of designing the MFS panel will be described in the next section.

6.2 Spacecraft and Structure Parameters

Referring back to Section 3.2, only one of the 4 relevant parameters there defined will be varied for the purposes of producing varied panel designs: the specific energy storage requirement of the spacecraft. Some assumptions are required to relate a given value of SER_{sat} to a generic panel configuration. Since only a part of the structure is considered, and not the entire spacecraft or even the entire structure, three new parameters must be introduced.

Structural mass fraction, α_{stru}, relates the mass of the spacecraft's primary structure to the total mass of the spacecraft. This varies from as little as 8%, a typical value for large communications satellites, to 25% or higher for the smallest spacecraft.

$$\alpha_{stru} = \frac{M_{stru}}{M_{sat}} \tag{6-1}$$

Specific multifunctional energy capacity, SEC_{mfs}, relates the energy stored in an MFS panel to the mass of the original inert panel it replaces.

$$SEC_{mfs} = \frac{E_{batt}}{M_{panel}} \tag{6-2}$$

Finally, the **multifunctional potential,** η_{mfs}, measures how much of the structure can actually be used as a multifunctional structure. Not all structural elements are sandwich panels, and it is clear that one could not insert electrical cells into the core of every sandwich panel in a structure, as some panels will for various reasons be unsuited to such a purpose. An external panel used for the mounting of solar arrays, for example, would result in the batteries being exposed to damaging temperatures [88], whilst some panels would include so many inserts as to render placement of cells impractical. Equally, distributing the battery too widely through the structure would result in long and possibly awkward cable paths. η_{mfs} is defined as the ratio between the mass of the multifunctional panels in the spacecraft and the total mass of structure.

$$\eta_{mfs} = \frac{M_{mfs}}{M_{stru}} \tag{6-3}$$

Combining these terms (noting that $M_{mfs} = M_{panel}$ and $E_{batt} = E_{sat}$ where the "spacecraft" considered is a single multifunctional panel) results in an expression for satellite specific energy requirement:

$$\alpha_{stru} SEC_{mfs} \eta_{mfs} = \frac{M_{stru}}{M_{sat}} \frac{E_{batt}}{M_{mfs}} \frac{M_{mfs}}{M_{stru}} = \frac{E_{batt}}{M_{sat}} = SER_{sat} \tag{6-4}$$

It is difficult to quantify η_{mfs}, as its value is too dependent on the precise attributes of the particular spacecraft design to make doing so useful. A value of 0.25 is used throughout, though, given that a range of values is used for other parameters, one could consider different values of η_{mfs} by holding one of these constant instead. Varying the measurable parameters, SER_{sat} and α_{stru}, on the other hand, allows one to calculate values of SEC_{mfs}, as shown in Table 6-3.

The attributes of the batteries are then used to convert these values into a number of cells per panel. The attributes of the battery are shown in Table 6-4. Note that the values used for modelling are slightly altered from those of the real cell to allow a uniform mesh to be used; the attributes of a real cell are also shown in the table.

SER_{sat}, $Whkg^{-1}$	Values of α_{stru}			
	0.1	**0.15**	**0.2**	**0.25**
1	40	27	20	16
2	80	53	40	32
3	120	80	60	48
4	160	107	80	64
5	200	133	100	80

Table 6-3 - SEC_{mfs} for various values of SER_{sat} and α_{stru}

Attribute	PLF523450	Assumed value
Footprint	49.2 x 34 mm	50 x 35 mm
Depth	5.2 mm	5 mm
Specific Energy	222 $Whkg^{-1}$	222 $Whkg^{-1}$
Density	1840 kgm^{-3}	1840 kgm^{-3}
Mass	16 g	16.1 g
Energy capacity	3.55 Wh	3.57 Wh

Table 6-4 - Cell attributes

Using a 20 mm deep core means the cells must be placed in stacks of 4. This results in each single battery unit of four cells having an energy capacity of 14.3 Wh. Using this value, and the mass of the original panel (1.39 kg), the values of SEC_{mfs} from Table 6-3 may be converted into a number of battery units per panel. Of course, it is impossible to include fractional numbers of cells in a panel, and so these numbers must be rounded. In any case, the precise parameter values listed do not refer to a particular spacecraft; rather, the range of values is of interest. As will be noted subsequently, the battery layout in the panels modelled will be symmetric about two axes, so the

number of four cell stacks will be rounded to a multiple of four. These values are shown in Table 6-5.

SER_{sat}, $Whkg^{-1}$	Values of α_{stru}			
	0.1	0.15	0.2	0.25
1	4	4	4	4
2	8	4	4	4
3	12	8	4	4
4	16	12	8	8
5	20	12	8	8

Table 6-5 - Number of cells per panel, in multiples of 4

6.3 Loading and Layout

6.3.1 Added Mass

A multifunctional structural panel will still be subjected to the normal in-service loads of its monofunctional counterpart. To represent this, the modelled panel has a load equal to 3 times its own mass smeared evenly over its area. This is consistent with an overall structural mass fraction (α_{stru}) of 25%, though of course an individual panel is not necessarily representative of the spacecraft as a whole. In the case of larger spacecraft with significantly lower values of α_{stru} (and hence, on average, more mass mounted on each structural component) it is reasonable to assume that some panels would be less heavily loaded. The additional mass is represented in the model by increasing the density of the facesheets appropriately.

It is assumed that this mass includes the battery, so the smeared mass is reduced when batteries are moved to the core of the panel. For example, the plain panel with no batteries has a "dry" mass of 1.387 kg, and 4.161 kg of additional mass smeared over it to represent the components that would typically be mounted on a structural panel. One then removes a theoretical battery of four sets of four cells (each cell having a

mass of 16.1 g), plus its enclosure from the load mounted on the panel. The mass of the enclosure is assumed to be one quarter of the mass of the cells, equating to a value of η_{para} of 25%, which is typical for a spacecraft battery.

The mass of this battery, 0.32 kg, is thus removed from the smeared mass on the facesheets, and, to make the multifunctional panel, the cells are added to the core, replacing part of the original honeycomb. This results in an overall mass reduction equal to the parasitic mass of the original battery plus the mass of the core that is replaced by the cells. This is summarised in Table 6-6, using the example given here (i.e., a battery of 16 cells). The density of the battery is 1840 kgm^{-3}, whilst the density of the core is 100 kgm^{-3}, resulting in a value of η_{para} after modification of -5.4%. In practice, the multifunctional structure would not necessarily replace the panel upon which the original battery was mounted; indeed, it is more likely that the structure would be designed from the outset to be multifunctional. However, removing the battery from a normal mounting would result in part of the structure being loaded differently, and, by considering this in the multifunctional panel, the change in mass this effects may be accounted for.

Component	Conventional design	MFS panel
Facesheets	0.800 kg	0.800 kg
Core	0.587 kg	0.573 kg
Cells	0.258 kg	0.258 kg
Battery enclosure	0.062 kg	-
Smeared mass	4.161 kg	3.841 kg
Total	**5.548 kg**	**5.472 kg**

Table 6-6 - Mass properties of conventional and MFS panel

6.3.2 Cell Layout

Relocating the cells from a conventional mounting to within the core has two effects on the dynamic behaviour of the panel. Firstly, it moves the mass of the cells further

from the centre of the panel, which will improve its dynamic characteristics. From this point of view, the cells should be as close to the supports of the panel as is possible. Secondly, removing part of the core and replacing it with the lower modulus cells will reduce the overall stiffness of the panel. From this perspective, it is desirable to place the cells as far as possible from the supports, which creates a conflict. The location of the cells must, therefore, be optimised.

Finding the precise optimal location for all of the cells would be a time-consuming process, so a series of constraints were applied to reduce the number of permutations.

The layout of the batteries is symmetric about the two axes of symmetry of the panel itself as shown in Figure 6-1. This was done to simplify the modelling procedure, though it may mean that the "optimal" designs chosen were not truly optimal. Likewise, to limit the number of permutations, the cells will be arranged in no more than two groups per edge of the panel (i.e., a total of 8 cell groups per panel). This not only simplifies the process of modelling the panels, but would also reduce the amount of labour required to manufacture the panel.

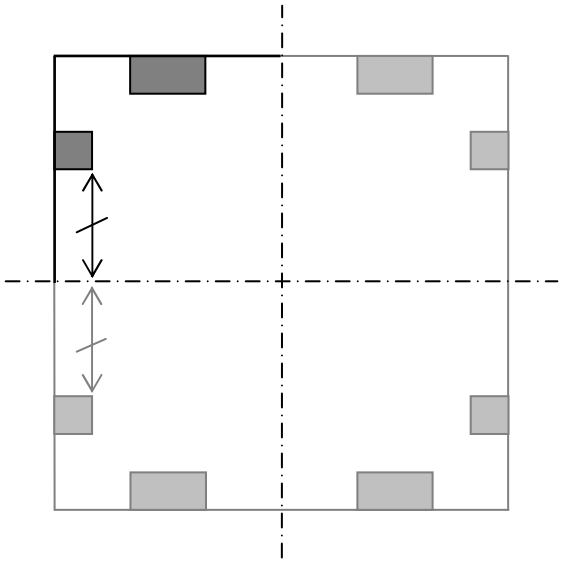

Figure 6-1 - Symmetric cell layout

In addition, the cells are placed with one face exposed, i.e., they are not fully surrounded by the original core material. This is a practical consideration, which is done for two reasons.

The first and most obvious benefit of placing the cells at the edge of the panel is that of cabling: the need to route power cables through the core or facesheets would add complexity to the design and likely affect the structural performance, so placing the cells where they may be easily accessed is important.

Secondly, although it has been demonstrated that the cells can survive the curing environment required to cure the resin adhesive used in a conventional sandwich panel, it may still be preferable to use cold-bonding (i.e., an adhesive that cures at room temperature) to fix the cells in place, after the facesheets and core have been assembled and cured. This approach allows more commonly used, higher-temperature resins to be used for the rest of the panel, improving its mechanical characteristics. It also allows the act of putting the cells in place to be delayed, which reduces the probability of accidental damage to cells that have been bonded in place: if, for example, a cell were to be inadvertently short-circuited, and thus rendered inoperative, after being glued in place, the entire panel would probably have to be discarded. Replacing the panel and the cells placed in it would be costly both in financial terms and in terms of delays to the project, and so a minor reduction in performance to mitigate this risk would quite possibly be acceptable.

The location of the cells in the panel is varied with a resolution of 25 mm, half the length of the battery itself. The range of values is dependent on the number of cells along the edge of panel in question: the batteries were not placed any closer than 50 mm to the corner of the panel, ensuring that the presence of the batteries did not significantly reduce the cross section of the honeycomb in this highly loaded region. The other extreme is the midpoint of the edge, since the panel is symmetric.

6.3.3 Terminology

Given these constraints, each panel design is thus defined by three characteristics: 1. The number of cell blocks per quarter panel; 2. How they are divided between the two outer edges (referred to as the configuration); and 3. The location of the cell group(s) along the edge.

The configuration indicates how many cell blocks per quarter panel are located on the Y and X edges respectively, so for example a 2-1 configuration indicates two blocks of cells on the Y edge and one on the X edge, whereas a 3-0 configuration would place 3 cell blocks on the Y edge and none on the X edge.

The location of the cell blocks along each edge is defined by the distance in mm from the corner of the panel to the first cell, the Y edge being listed first. Therefore, a 3-cell panel, in 2-1 configuration, with the cells in the 75-100 location would be as shown in Figure 6-2.

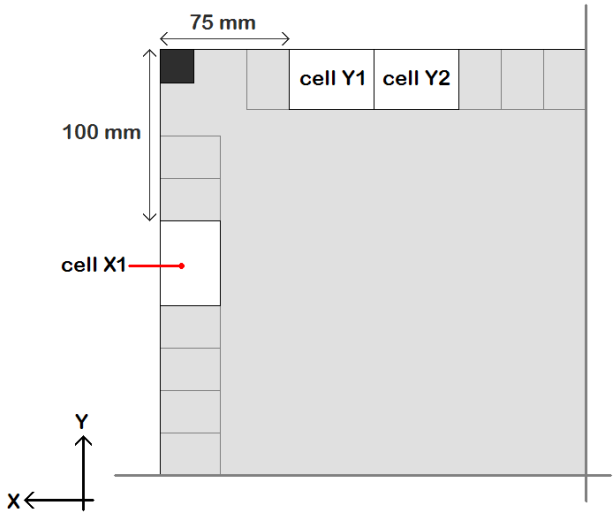

Figure 6-2 - Example panel in 3_2-1_75-100 configuration

6.4 FE Modelling: First Mode of Vibration

Using the values and constraints outlined above, a total of 147 unique panel designs were produced. In order to rapidly eliminate a large proportion of these designs by a simple criterion, the first pass of the optimisation procedure was based on the frequency of the first mode of vibration. This is often one of the primary requirements for spacecraft structures, so investigating the first mode allowed the majority of the panels to be discarded on the basis that their natural frequencies are too low. More detailed optimisation was then carried out on full models of the more promising designs, as will be described in Section 6.6.

To facilitate the production of a large number of models, with varying quantities and layouts of battery cells in the core, the core was modelled as a series of solids whose material properties could be changed between standard honeycomb and PLI cell, as shown in Figure 6-3. Whilst this slightly increased the number of elements in the model, and hence the processing time, it allowed such changes to be made in the Simulation environment rather than the DesignModeller parametric CAD programme, saving time in the model creation stage. The first cell blocks, X-1 and Y-1, are located 50 mm from the corner of the panel; each solid is 25 by 35 mm in footprint, and 20 mm deep, allowing the cells to be placed with a resolution of 25 mm. For example, if two complete stacks of cells were to be placed on the Y edge of the panel, 125 mm from the corner, solids Y-1 to Y-3 would be set to honeycomb, Y-4 to Y-7 would be PLI cell and Y-8 would also be honeycomb. The panels were modelled using the Ansys Workbench software and meshed using the elements shown in Table 6-7.

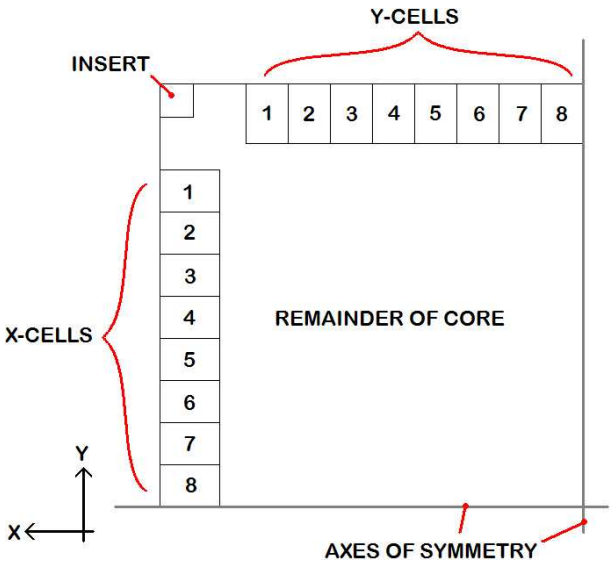

Figure 6-3 - Cell layout

Component	Element type	Number
Facesheets	Shell181 – 4 Node Linear Quadrilateral Shell	5000
Honeycomb	Solid186 – 20 Node Quadratic Hexahedron	7696
Cells	Solid186 – 20 Node Quadratic Hexahedron	1920
Insert	Solid186 – 20 Node Quadratic Hexahedron	64
Contact	Targe170, Conta173, Conta174	98596
Total	-	**113337**

Table 6-7 - Elements used in panel model (for 1-1 configuration)

Note that, to save processing time, only one quarter of the panel was actually modelled, with symmetry constraints being applied along the appropriate edges. This symmetry was represented by constraining the motion of the nodes along the planes of symmetry. Referring to Figure 6-3 to define a coordinate system, these nodes were constrained to translate only in the Z-axis (orthogonal to the X- and Y-axes indicated on the figure). Rotation was permitted only around the axis perpendicular to the plane itself. The meshed model is shown in Figure 6-4. In addition to this symmetry constraint, the corner insert was restrained with a fixed support on the lower (Z-)

face, i.e., the nodes comprising this face were fully constrained in translation and rotation.

A modal analysis was then run to find the natural frequencies of the panel, the first mode shape of the quarter panel being shown in Figure 6-5. The frequency of the first mode of vibration is often one of the primary requirements for a spacecraft structure, so investigating the first mode allows the majority of the models to be discarded on this basis; further optimisation was then carried out on a full model. It should be noted that no lower limit was placed on the frequency of the first mode. In practice, a requirement is placed on the spacecraft as a whole by the launch authority; the performance expected of individual components varies.

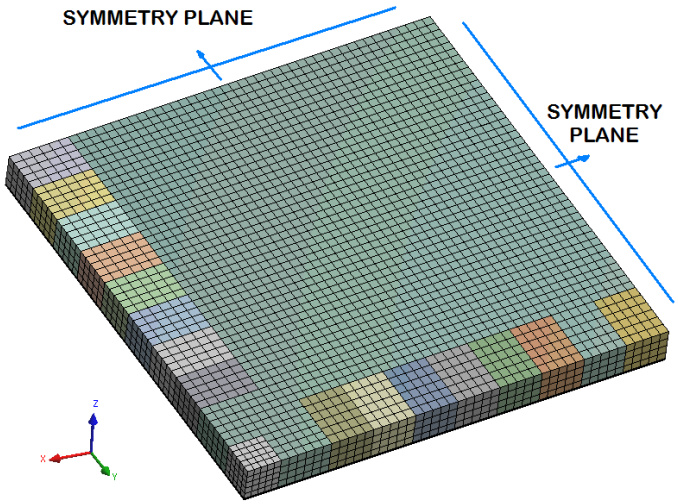

Figure 6-4 - Mesh for model of quarter panel (facesheet omitted for clarity)

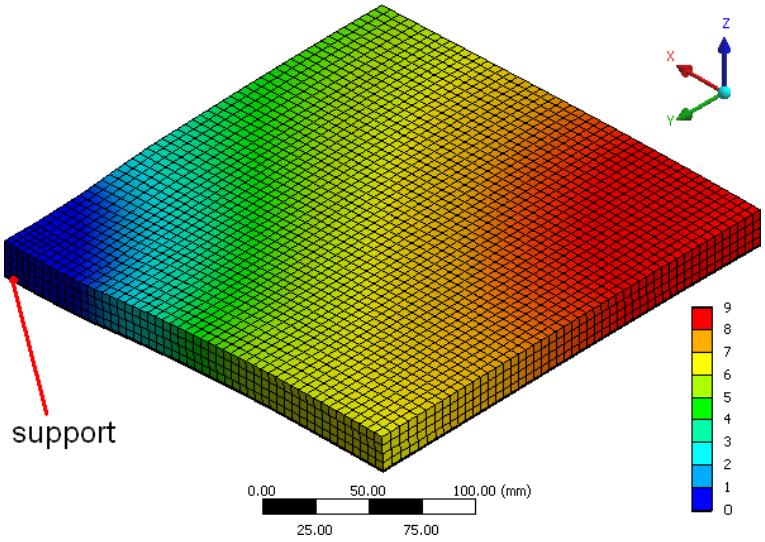

Figure 6-5 - Deformed shape of first mode (typical). Scale shows normalised deformation.

6.5 Results: First Mode of Vibration

6.5.1 No cells – Conventional Panel

The calculated natural frequency of the "mono-functional" panel with no integrated cells was 175.48 Hz. All other results will be given relative to this result.

6.5.2 1 Cell Block

Due to the symmetry of the square panel, the 1-0 and 0-1 configurations give identical results – that is, placing a single cell on the X edge is the same as placing a single cell on the Y edge. Hence, although there are two possible configurations for the panel, they give identical results and so only one dataset is presented. The change in the frequency of the first mode of vibration is shown in Figure 6-6.

6.5.3 2 Cell Blocks

In this case, there are two unique configurations: 2-0 and 1-1. In the case of the 1-1 panel, there are two variables (i.e., the location of the single block of cells on the X

and Y edge) and so the results are presented as a carpet plot. The results are shown in Figure 6-7 and Figure 6-8.

6.5.4 3 Cell Blocks

In this case, there are also two possible configurations, 3-0 and 2-1, the latter being presented as a carpet plot once more. These results are shown in Figure 6-9 and Figure 6-10.

6.5.5 4 Cell Blocks

There are three unique configurations of four cell blocks per panel: 4-0, 3-1 and 2-2. Note that, given that 4 cell blocks occupy all of the available "slots" on the panel edge, there is only one permutation in the 4-0 case, which results in a change in the 1st mode of **+2.10%**. The remaining results are shown in Figure 6-11 and Figure 6-12.

6.5.6 5 Cell Blocks

There are two unique configurations in this case, 4-1 and 3-2. In the 4-1 configuration, it is not possible to move the four cell blocks on the y edge, and so only the variation of x position is shown. The 3-2 configuration is presented as a carpet plot. These results are shown in Figure 6-13 and Figure 6-14.

6.5.7 Carpet Plots

The carpet plots referred to in the preceding sections are effectively surface plots, as they show the variation of the natural frequency with respect to two independent variables. For readers unfamiliar with this type of graph, it should be noted that a carpet plot has no horizontal axis; the interaction of the two datasets provides this information. Taking Figure 6-8 as an example, if one wishes to know the change in frequency for a panel with cells located at X = 75 and Y = 150, the result is the

intersection of the "x-75" and "y=150" lines: 2.25%. This means of presenting the data was chosen in preference to tables, as it allows the sensitivity of the frequency to placement of the cells to be made evident. In addition, the large number of data points (148 separate results) would have been rather unwieldy in tabular form.

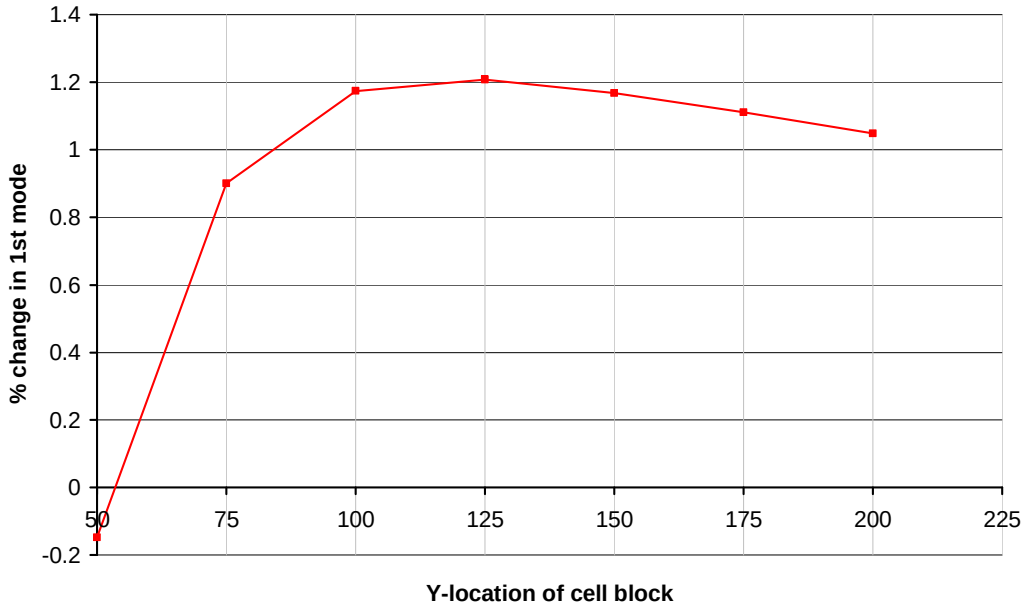

Figure 6-6 - 1st mode results for 1_1-0 panel

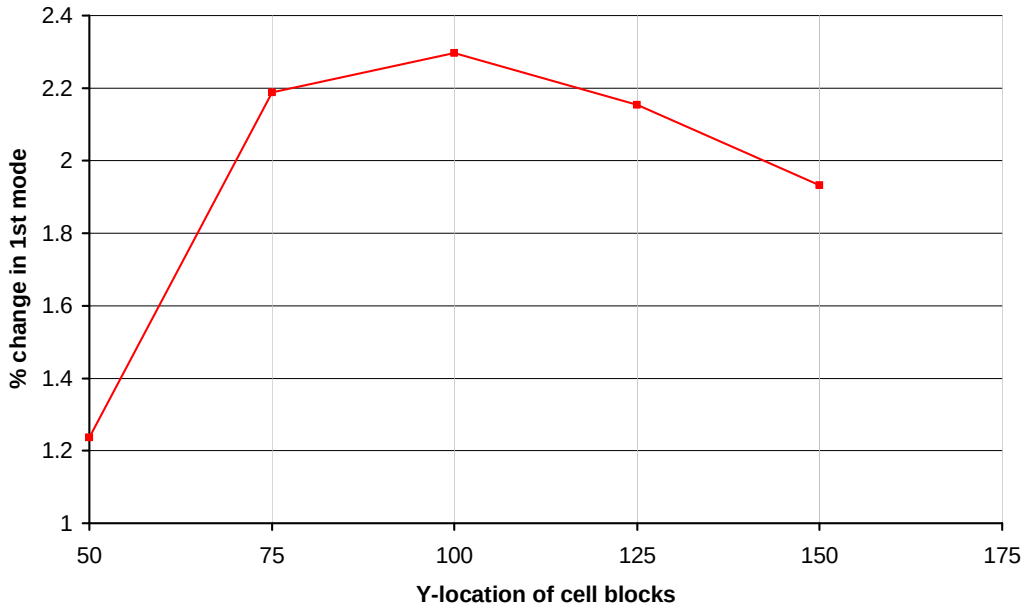

Figure 6-7 - 1st mode results for 2_2-0 panel

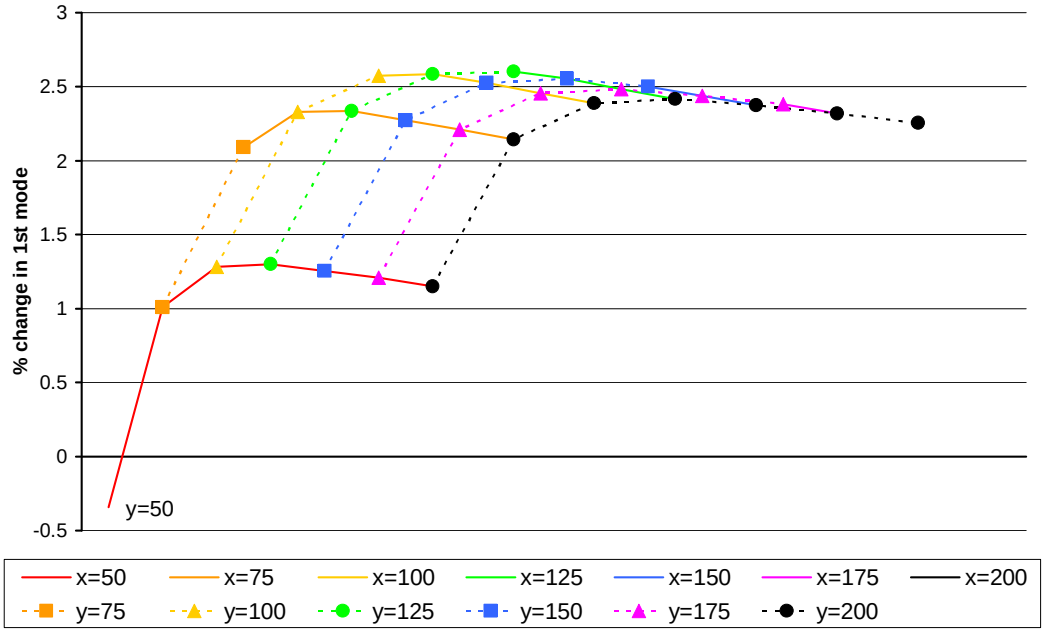

Figure 6-8 - 1st mode results for 2_1-1 panel

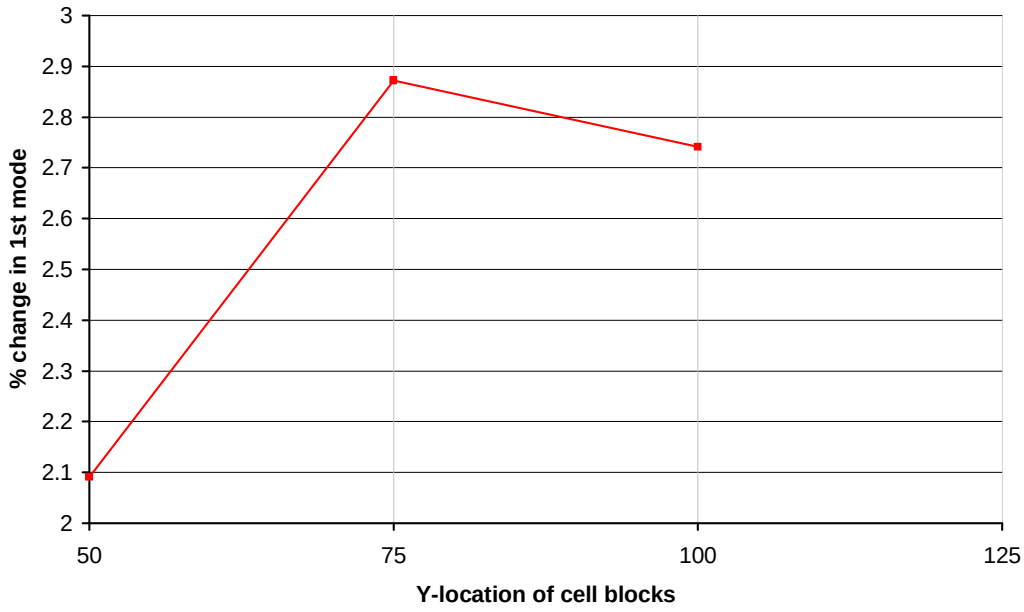

Figure 6-9 - 1st mode results for 3_3-0 panel

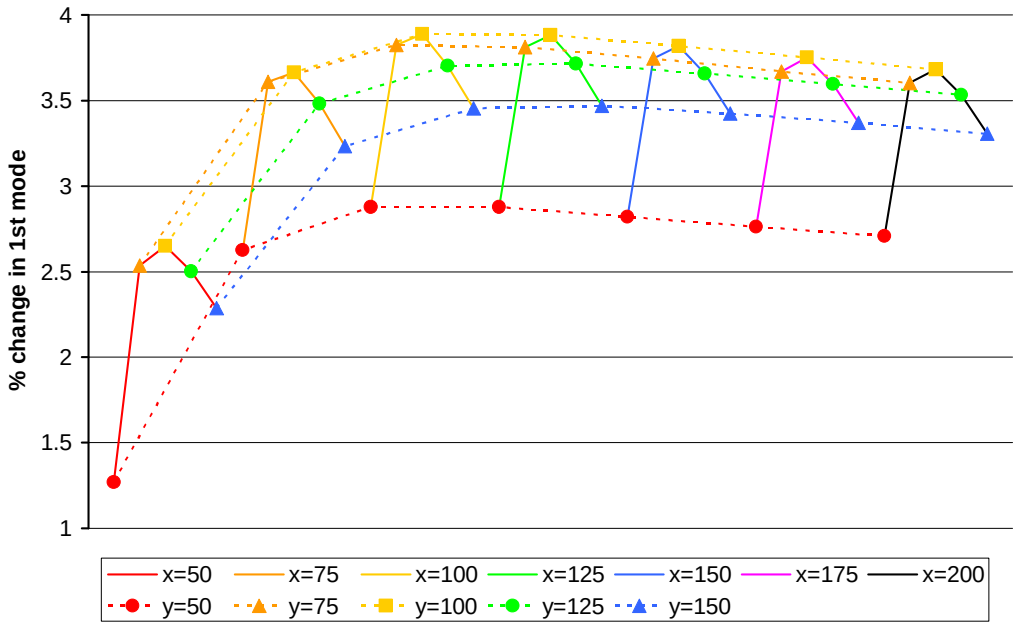

Figure 6-10 - 1st mode results for 3_2-1 panel

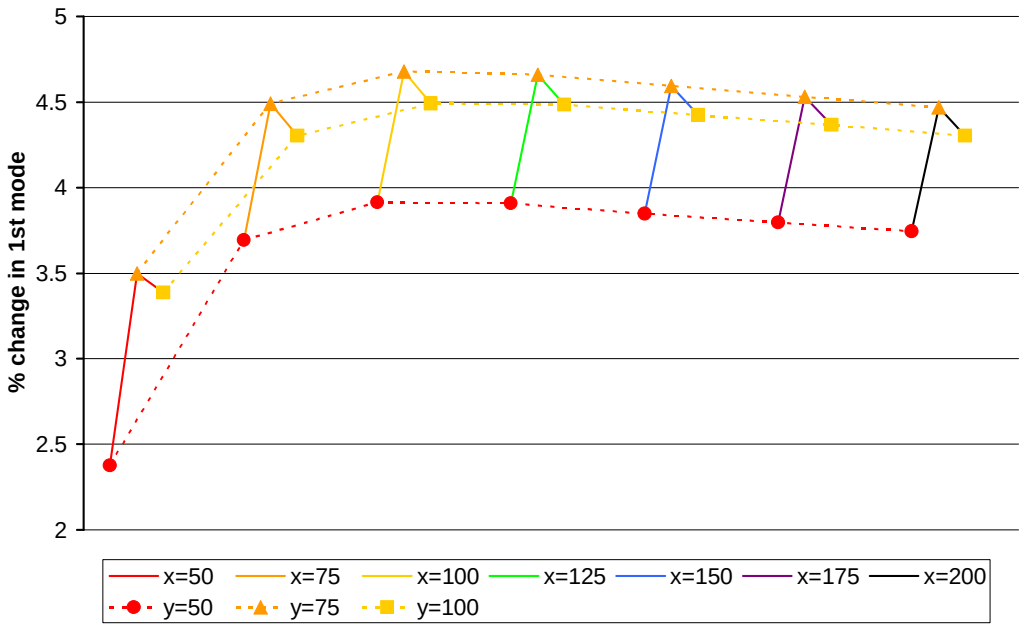

Figure 6-11 - 1st mode results for 4_3-1 panel

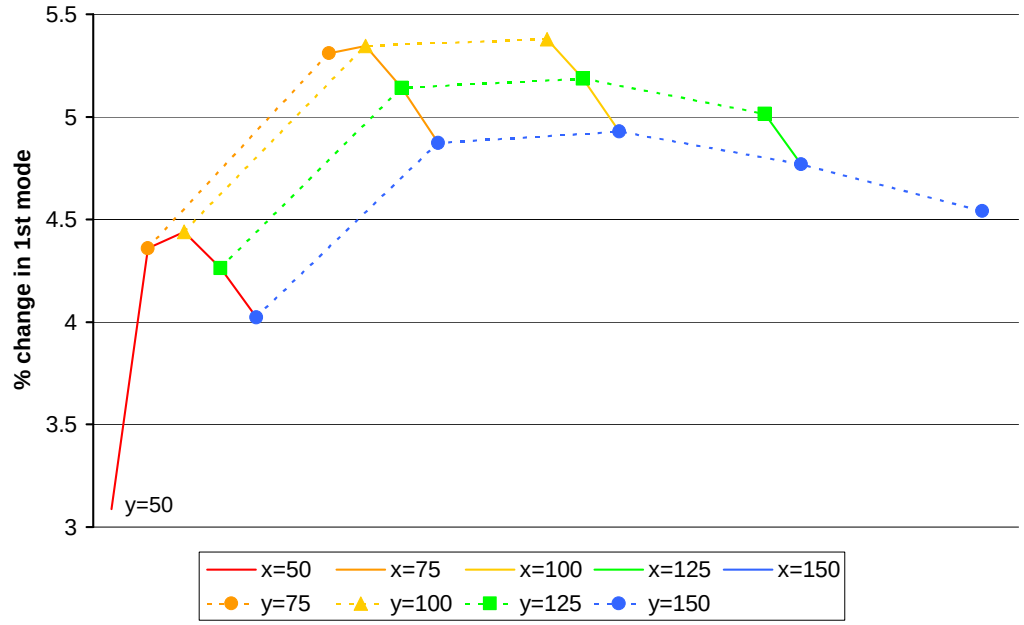

Figure 6-12 - 1st mode results for 4_2-2 panel

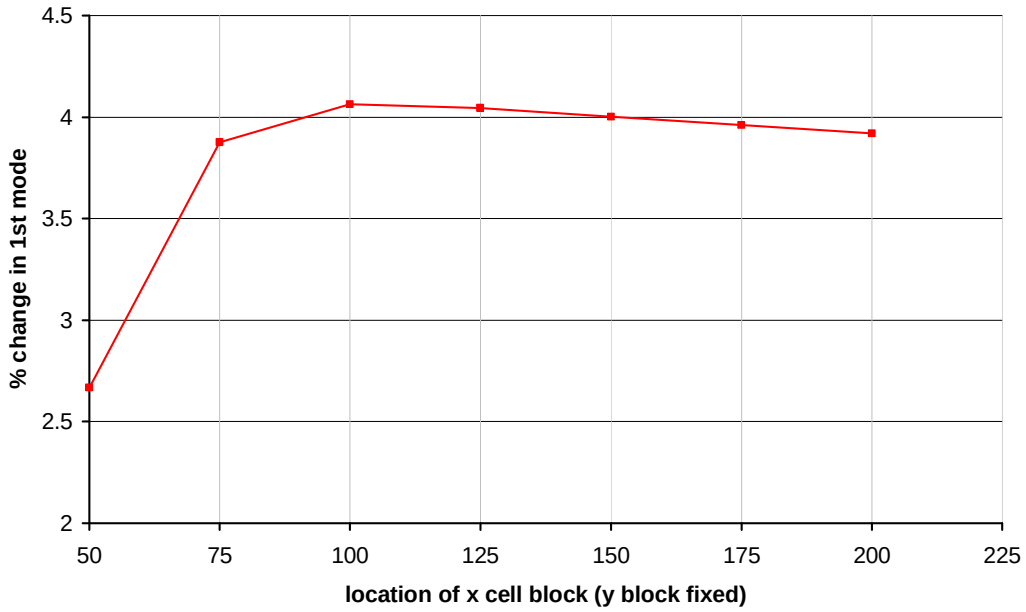

Figure 6-13 - 1st mode results for 5_4-1 panel

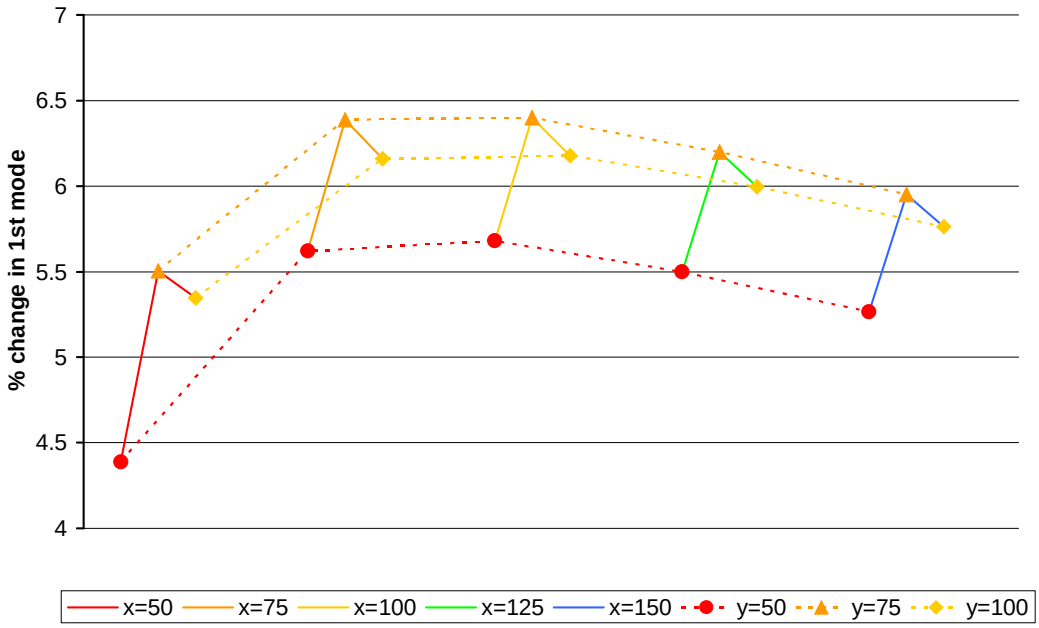

Figure 6-14 -1st mode results for 5_3-2 panel

6.5.8 Observations and Analysis: First Mode of Vibration

It is clear from the mode 1 results that changing from a conventional to a multifunctional structure results, in almost all cases, in an increase in the frequency of the first mode of vibration. The positive effect of redistributing the mass of the batteries and removing the parasitic mass exceeds the negative effect of replacing the honeycomb core with the less stiff batteries. In addition, the very worse performance occurs when the cells are near the corner of the panel, also suggesting that the effect on stiffness is more important than that on mass distribution in the range of locations investigated. The batteries near the insert will occupy a significantly larger proportion of the cross section of the core, and are in a location that carries more stress, thus the effects of their poorer structural attributes are more significant.

Overall, the first mode results are promising. Based on these results alone, there is no need for additional stiffening of the panel (e.g., using thicker facesheets or a denser core) in order to achieve similar structural capacity. Additional investigations are required, however, to demonstrate that this is equally true by all criteria.

The designs are grouped according to the number of cells in each panel, and each group is then sorted according to the mode 1 results. Any panels where the improvement in the first mode is within 5% of the best design are included in the next stage of this analysis. This resulted in 29 of the 147 panel designs, listed in Table 6-8, being carried forward to the next stage of the analysis.

No. of cells	Cells on Y edge	Cells on X edge	Cell positions, mm		1st mode frequency (Hz)	% change from non-MFS panel
			Y cells	X cells		
0	0	0	-	-	175.48	-
	1	0	125	-	177.60	1.21
1	1	0	100	-	177.54	1.17
	1	0	150	-	177.53	1.17
	1	1	125	125	180.05	2.60
	1	1	125	100	180.02	2.59
	1	1	100	100	180.00	2.58
2	1	1	150	125	179.96	2.55
	1	1	150	100	179.91	2.53
	1	1	150	150	179.87	2.50
	1	1	175	125	179.84	2.49
	2	1	100	100	182.30	3.89
	2	1	100	125	182.29	3.88
	2	1	75	100	182.19	3.82
	2	1	100	150	182.18	3.82
3	2	1	75	125	182.17	3.81
	2	1	100	175	182.06	3.75
	2	1	75	150	182.05	3.74
	2	1	125	125	182.00	3.72
	2	1	125	100	181.98	3.70
	2	2	100	100	184.92	5.38
	2	2	100	75	184.86	5.35
4	2	2	75	75	184.80	5.31
	2	2	125	100	184.58	5.19
	2	2	125	75	184.50	5.14
	3	2	75	100	186.71	6.40
	3	2	75	75	186.69	6.39
5	3	2	75	125	186.36	6.20
	3	2	100	100	186.32	6.18
	3	2	100	75	186.29	6.16

Table 6-8 - Panel designs selected for further optimisation

6.6 Background and Modelling: Random Vibrations

6.6.1 2nd Pass Performance Criteria

Having limited the selection of panel designs to the 29 most promising arrangements of the cells, the next stage in the investigation was to simulate the effect of adopting an MFS on the response of the panel to random vibration. The dynamic environment of a spacecraft launch is generally the most demanding mechanical condition to which the structure will be subjected, and random vibration forms the greater part of this. The random vibration loading applied was representative of a typical launcher.

Three criteria were used to assess the change in the panel's response compared to the conventional, monofunctional design: maximum stress in the core and facesheets (denoted by σ_{max} in the case of normal and von Mises stress, τ_{max} for shear stress), maximum acceleration (a_{max}) of the panel and maximum deformation (z_{max}) of the panel, all of these quantities being the calculated RMS values. The stress component measured in the facesheet was the von Mises equivalent stress; in the core, the out-of-plane compressive stress and both components of the in-plane shear stress were considered. The magnitude of the change was then used to assess how the structure would need to be modified in order to achieve the same structural performance as the original.

Maximum stress in the panel's structural components is perhaps the most fundamental of these criteria. Any structure must be capable of surviving the mechanical environment into which it is to be placed, irrespective of any other constraints that may be placed upon its design, without structural failure. If the adoption of a multifunctional structure increases stress in facesheets or core of the panel under the expected loading conditions, then these components would need to be reinforced to compensate. If, on the other hand, stress is reduced, the components may be reduced in mass.

Maximum acceleration would be a defining characteristic if a panel were to be used to mount sensitive or delicate equipment. In this case, it would be necessary to ensure that such items were not subjected to excessive acceleration. Hence, if adopting the multifunctional structure results in an increase in acceleration, an increase in structural mass would be required to compensate, and likewise a reduction in acceleration allows in a decrease in mass.

The importance of maximum deformation is also dependent on the use for which the panel is intended. A good example of a use that applies a deformation constraint is a solar array. If the solar cells and their cover glass are glued directly to a panel, excessive curvature could either crack the cells or glass, or cause the adhesive to fail. Whilst measuring local curvature is not straightforward, the peak displacement gives a good indication of the large-scale curvature of the panel. Once more, therefore, an increase in peak deformation will require additional structure, whilst a reduction will allow a decrease in structural mass.

The average stress in the batteries was also recorded. Reducing stress in the battery was not considered an objective, since altering this quantity would be less likely to result in an overall mass reduction. However, it was necessary to ensure that the correct shear modulus was used in the models, by comparing the measured shear stress with Figure 4-27.

The additional mass smeared over the panels (as described in Section 6.3.1) was retained for this testing.

6.6.2 Modelling

Due to the increased complexity of this model, a coarser (10 mm) mesh was used initially to reduce processing time. In all other respects, the design and layout of the complete panel was as for the first mode models. The loading applied to the panel was

the same 25 g_{rms} random vibration profile used to test the cells in Section 4.2.2, as shown in Figure 4-7 (p72). The first two symmetric modes were used in the analysis.

The panels were again modelled using the Ansys Workbench software and meshed using the elements shown in Table 6-9. Note that the information shown in this table is for the 1-1 (1 cell block per edge) configuration; models of a panel with more cells required slightly more contact elements (6408 in the case of a panel with 5 cells per quarter). The number of body elements was unchanged, however, as the mesh for the core and cells was identical. The support and symmetry constraints described in Section 6.4 were applied to this model also.

Component	Element type	Number
Facesheets	Shell181 – 4 Node Linear Quadrilateral Shell	1250
Honeycomb	Solid186 – 20 Node Quadratic Hexahedron	1172
Cells	Solid186 – 20 Node Quadratic Hexahedron	70
Insert	Solid186 – 20 Node Quadratic Hexahedron	8
Contact	Targe170, Conta173, Conta174	6362
Total	-	**8862**

Table 6-9 - Elements used in panel model (for 1-1 configuration)

6.7 Results: Random Vibration

The complete results of the random vibration models are shown in Table 6-10 and Table 6-11. Note that the configuration of the cells is not listed; all of the panel designs for a given number of cells used the same configuration, as follows:

- 1 cell per quarter panel: 1 cell on Y edge, no cells on X edge
- 2 cells per quarter panel: 1 cell on Y edge, 1 cell on X edge
- 3 cells per quarter panel: 2 cells on Y edge, 1 cell on X edge
- 4 cells per quarter panel: 2 cells on Y edge, 2 cells on X edge

- 5 cells per quarter panel: 3 cells on Y edge, 2 cells on X edge

An example stress response to random vibration is shown in Figure 6-15 (shear stress in core) and Figure 6-16 (equivalent stress in facesheet). Figure 6-17 shows a typical acceleration response, whilst Figure 6-18 shows the deformation.

Using the axes defined in any of the figures in this section, the directions of the quantities given in the tables are as follows:

- Acceleration: Z axis. The acceleration at the centre of the panel was used in all cases. For some models, this was not the highest acceleration in the panel, due to localised effects near the batteries. The justification for this is expanded on in Section 6.8.3.
- Deformation: Z axis. In all cases, the maximum deformation occurred at the centre of the panel.
- Von Mises stress in facesheet: Maximum that occurred in any orientation.
- Direct stress in core: Z direction.
- Shear stress in core: Maximum stress in either XZ or XY orientation.
- Shear stress in battery: Average of stress in both XZ and XY orientation.

No. of cells	Cell position		a_{max}	z_{max}	$\sigma_{face,max}$	$\sigma_{core,max}$	$\tau_{core,max}$	$\tau_{batt,ave}$
	Y, mm	X, mm	g	mm	MPa	MPa	MPa	kPa
0	-	-	127	0.999	87.0	3.09	1.47	-
	100	-	128	0.983	86.5	3.07	1.47	33.8
1	125	-	128	0.983	86.6	3.07	1.50	28.4
	150	-	128	0.984	86.4	3.08	1.49	24.3
	100	100	130	0.966	86.0	3.05	1.42	36.5
	125	100	130	0.967	86.1	3.05	1.44	38.6
	125	125	130	0.967	86.1	3.04	1.46	40.1
2	150	100	130	0.967	86.0	3.06	1.44	34.6
	150	125	130	0.968	86.0	3.05	1.44	36.1
	150	150	130	0.968	85.9	3.06	1.43	31.9
	175	125	129	0.968	86.1	3.04	1.46	35.7
	75	100	131	0.950	85.6	3.03	1.45	43.5
	75	125	131	0.951	85.6	3.02	1.47	45.1
	75	150	131	0.951	85.6	3.03	1.45	41.4
	100	100	131	0.949	85.4	3.03	1.42	36.9
3	100	125	131	0.950	85.4	3.03	1.44	38.5
	100	150	131	0.951	85.3	3.04	1.42	34.7
	100	175	130	0.952	85.5	3.04	1.42	34.5
	125	100	130	0.950	85.5	3.03	1.49	40.2
	125	125	130	0.950	85.5	3.02	1.48	41.7
	75	75	132	0.933	85.1	3.00	1.46	47.1
	100	75	132	0.933	85.0	3.01	1.44	40.4
4	100	100	132	0.933	84.7	3.02	1.42	38.1
	125	75	132	0.934	85.1	3.01	1.49	43.6
	125	100	132	0.934	84.8	3.02	1.44	41.3
	75	75	132	0.914	84.4	2.98	1.48	47.6
	75	100	132	0.915	84.2	3.00	1.46	45.0
5	75	125	132	0.916	84.3	2.99	1.45	45.2
	100	75	131	0.912	84.2	2.99	1.47	41.4
	100	100	131	0.913	83.9	3.00	1.42	39.1

Table 6-10 - Results of random vibration (absolute values)

No. of cells	Y pos	X pos	a_{max}	z_{max}	$\sigma_{face,max}$	$\sigma_{core,max}$	$\tau_{core,max}$
	mm	mm	% change from conventional panel				
0	-	-	0.00	0.00	0.00	0.00	0.00
	100	-	0.84	-1.60	-0.59	-0.50	-0.58
1	125	-	0.92	-1.54	-0.54	-0.74	1.53
	150	-	0.83	-1.53	-0.70	-0.44	0.81
	100	100	2.09	-3.25	-1.14	-1.26	-1.68
	125	100	2.12	-3.19	-1.06	-1.41	-0.87
	125	125	2.16	-3.17	-1.08	-1.67	0.81
2	150	100	2.02	-3.16	-1.16	-1.06	-1.99
	150	125	2.08	-3.10	-1.12	-1.37	0.77
	150	150	2.01	-3.06	-1.24	-1.05	-0.36
	175	125	1.97	-3.06	-1.07	-1.55	0.25
	75	100	2.87	-4.90	-1.67	-1.93	-0.34
	75	125	2.89	-4.84	-1.61	-2.19	2.67
	75	150	2.80	-4.76	-1.67	-1.83	1.28
	100	100	2.86	-4.97	-1.87	-1.79	-2.22
3	100	125	2.88	-4.90	-1.84	-1.85	0.82
	100	150	2.81	-4.83	-1.95	-1.56	-0.59
	100	175	2.71	-4.74	-1.80	-1.71	-0.18
	125	100	2.52	-4.92	-1.74	-1.86	0.87
	125	125	2.58	-4.86	-1.76	-2.23	0.45
	75	75	4.09	-6.58	-2.21	-2.96	2.19
	100	75	4.08	-6.60	-2.33	-2.45	0.86
4	100	100	4.06	-6.63	-2.69	-2.15	-0.77
	125	75	3.73	-6.52	-2.24	-2.63	1.06
	125	100	3.75	-6.51	-2.56	-2.29	-1.71
	75	75	4.09	-8.49	-3.00	-3.64	0.39
	75	100	4.10	-8.45	-3.22	-2.96	-0.76
5	75	125	3.85	-8.28	-3.14	-3.20	-0.81
	100	75	3.37	-8.68	-3.22	-3.28	-0.46
	100	100	3.41	-8.64	-3.55	-2.84	-3.41

Table 6-11 - Results of random vibration (relative to monofunctional panel)

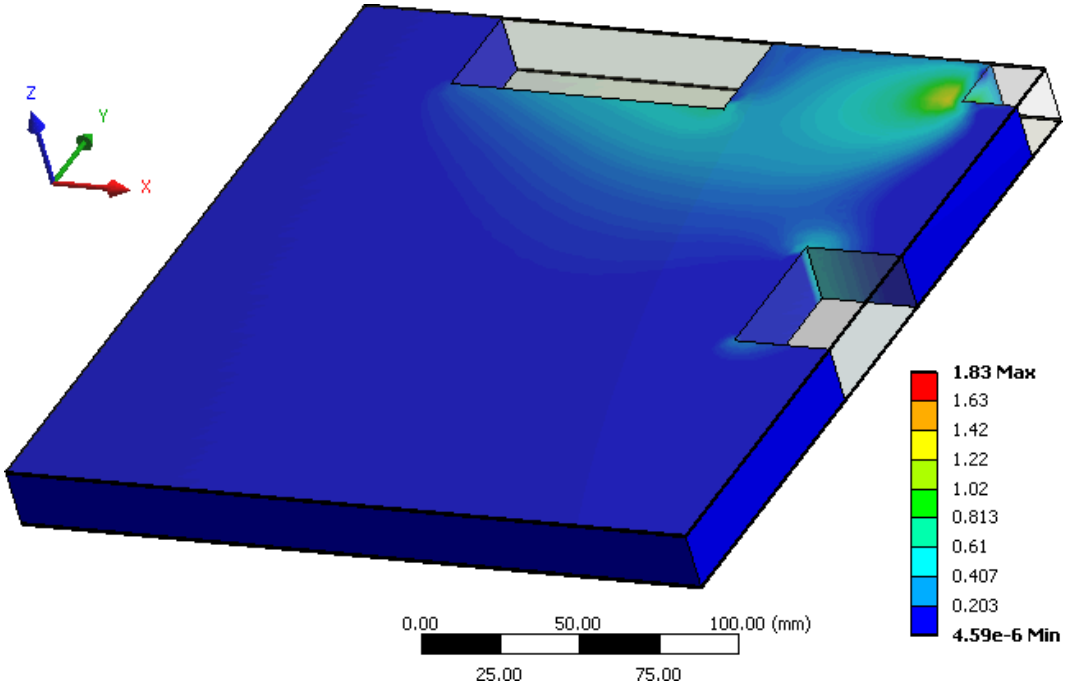

Figure 6-15 - Shear stress (XZ direction) in core (scale in MPa)

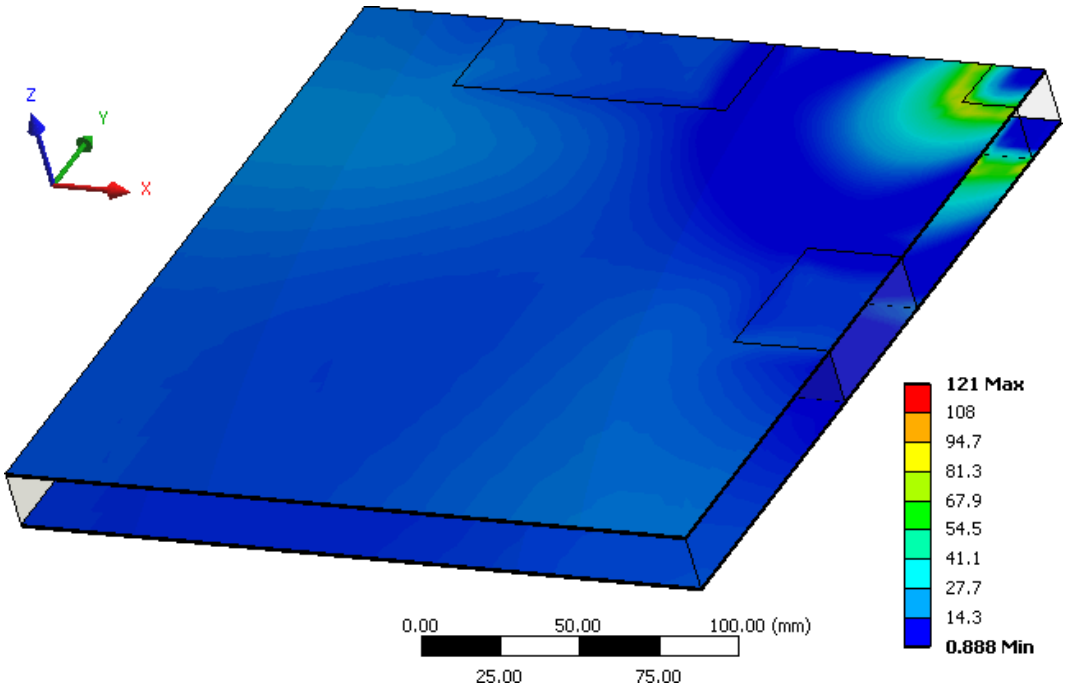

Figure 6-16 - Von Mises equivalent stress in facesheet (scale in MPa)

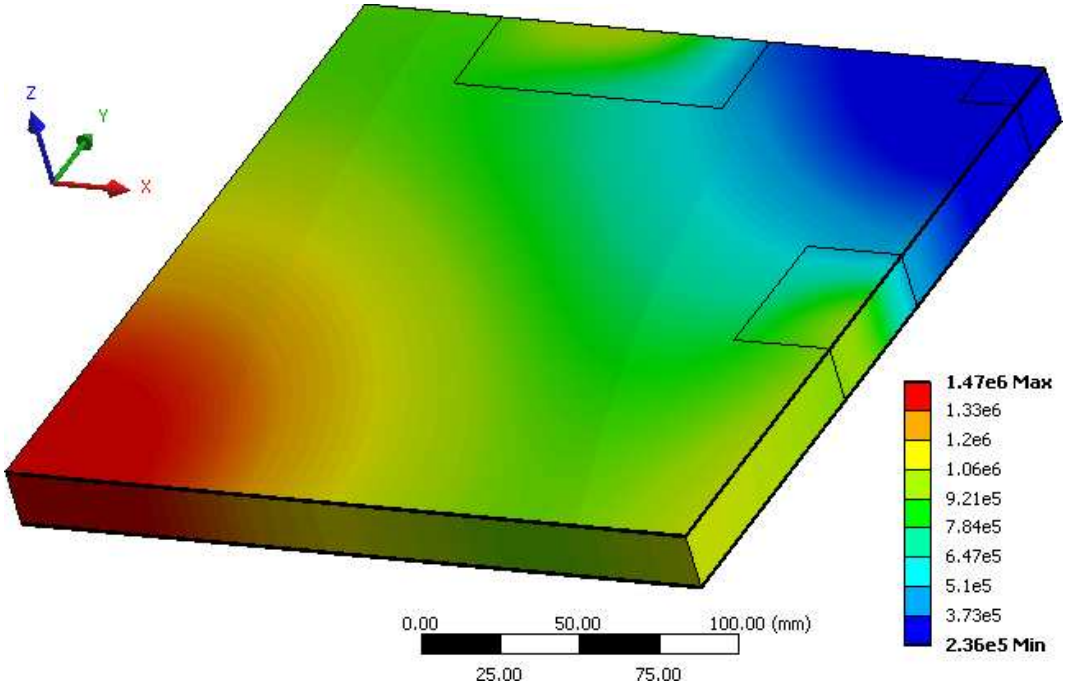

Figure 6-17 - RMS acceleration response of panel (Z-direction, scale in mms^{-2})

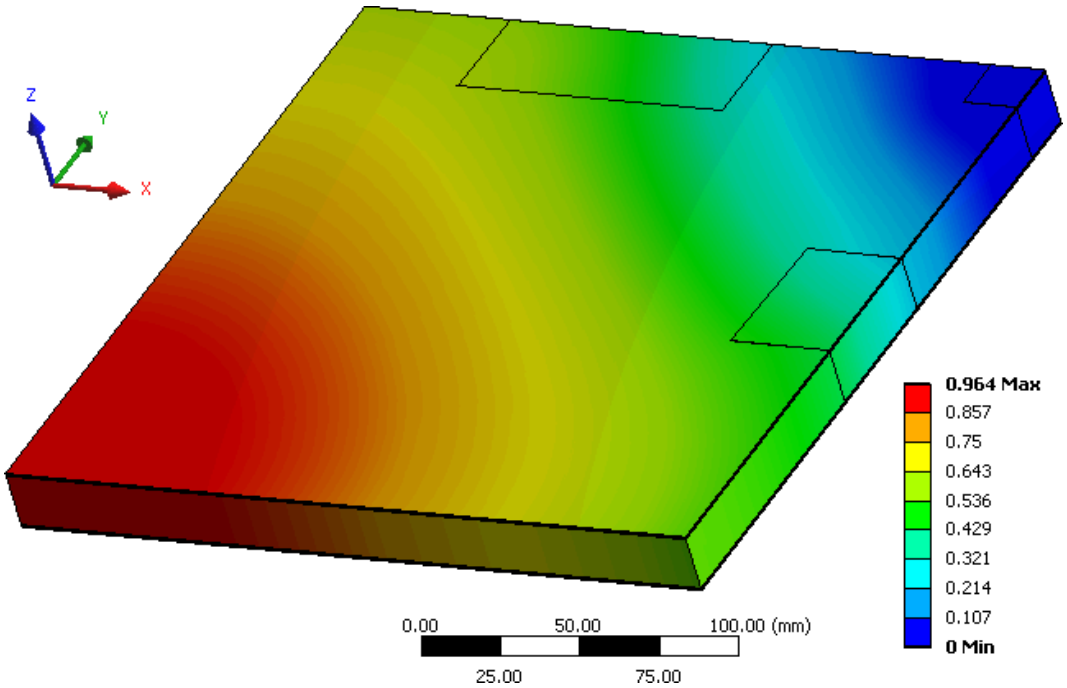

Figure 6-18 - RMS deformation response of panel (Z direction, scale in mm)

6.8 Analysis: Random Vibration

6.8.1 Approach

The three criteria (stress, acceleration and deformation) were considered separately. That is to say, it was assumed that the panel was required to satisfy just one of these criteria, and the most appropriate design selected. This led to 15 designs being selected, one optimised for stress, one for acceleration and one for deformation, for each of the 5 values of the number of cells per panel (in fact, there were 10 unique designs as some configurations showed the best performance in more than one criterion).

In the case of acceleration and deformation, the selection was simple, as there was only one variable. The optimal design according to either of these criteria is simply that which results in the largest decrease (or smallest increase) in the given parameter. In the case of stress, however, consideration must be given to both the core and facesheet.

The assumption was made that, for the small variations considered herein, changes in the panel would be approximately linear. Hence, a reduction in stress in the facesheet would allow a proportionate reduction in its thickness; equally, a lower stress in the core would allow a less dense honeycomb to be used, assuming its mechanical properties varied linearly with its density. Then, the relative importance of the change in stress in these two components (from the point of view of mass savings) was taken into consideration, through the relative masses of the core and facesheets in the given panel design. This allows a "combined stress change" (Σ_{comb}) parameter to be calculated for each panel as in equation (6-5), the minimum value of which corresponds to the optimal design.

$$\Sigma_{comb} = \max(\Delta\sigma_{z,core}, \Delta\tau_{xz,core}, \Delta\tau_{yz,core})\left(\frac{M_{core}}{M_{core} + M_{faces}}\right) + \max(\Delta\sigma_{equiv,faces})\left(\frac{M_{faces}}{M_{core} + M_{faces}}\right) \quad (6\text{-}5)$$

6.8.2 Optimal Designs

Based on the criteria outlined previously, the optimal panel designs were selected. The values calculated for Σ_{comb} are shown in Table 6-13 (the chosen designs are indicated by bold text and grey highlight). The designs selected by acceleration and deformation are shown in Table 6-12.

No. of cells	Y pos	X pos	a_{max}
	mm	mm	% change
1	100	-	+0.83
2	125	125	+1.97
3	125	100	+2.52
4	125	75	+3.73
5	100	75	+3.37

No. of cells	Y pos	X pos	z_{max}
	mm	mm	% change
1	100	-	-1.60
2	100	100	-3.25
3	100	100	-4.97
4	100	100	-6.63
5	100	75	-8.68

Table 6-12 - Optimal designs for acceleration (left) and deformation (right)

The measured shear stress in the batteries must also be assessed to ensure that an accurate (or conservative) value of their shear stiffness was used in the models. The average shear stress in the batteries, as shown in Table 6-10, varied from roughly 30 to 40 MPa for the chosen designs. Comparing this to Figure 4-27 (p95) suggested that a value somewhat less than the 25 MPa that was employed in the models would be appropriate. Using the second run of tests (i.e., the lower values) leads to a shear modulus of around 10 MPa; however, using a lower value for G also reduces the stress on the cells, as more of the loading will be carried by the surrounding honeycomb, so the models were re-run with G set to 15 MPa.

This modification led to slight changes in most of the results, though for the most part these changes were not significant. More importantly, the predicted shear stress in the cells with this value of the shear modulus ranged from 20 to 25 kPa, leading in turn to a shear modulus of over 15 MPa. Hence, while the precise value has not been used, the correct modulus lies between those tested, and thus the two sets of results bound the correct values.

The results of the combined stress calculations are summarised in Table 6-14; Table 6-15 and Table 6-16 show the contribution of the individual stress components. Adding batteries to the structure reduced the peak stress in the panel, with the optimal designs showing a fairly linear decrease in stress as the number of batteries increased. The influence of varying the shear modulus on the shear stress results was small.

The change in deformation shows the most positive result, as seen in Table 6-17. The peak deformation decreases notably as more power storage is placed in the core of the panel, the reduction exceeding 8% for the panel including 5 cell blocks. The deformation results show the most linear relationship with power storage, and also the smallest effect from varying the batteries' shear modulus, with practically no difference between the 15 and 25 MPa lines.

The acceleration results, shown in Table 6-18 gave a negative result (i.e., an increase in acceleration) throughout, with the change increasing as more cells were added to the panel. The relationship between the number of cells and the change in peak acceleration was less linear than for stress, and these results also showed the greatest sensitivity to changes in the shear modulus. A difference of 25-30% occurred between the two sets of results for the 5 cell block panel.

No. of cells	Y pos	X pos	M_{core}	M_{faces}	$\sigma_{face,max}$	$\sigma_{core,max}$	$\tau_{core,max}$	Σ_{comb}
	mm	mm	Mass in kg		% change from conventional panel			
	100	-			-0.59	-0.50	0.00	**-0.56**
1	125	-	**0.483**	**0.8**	-0.54	-0.74	-0.58	0.24
	150	-			-0.70	-0.44	1.53	-0.13
	100	**100**			-1.14	-1.26	0.81	**-1.18**
	125	100			-1.06	-1.41	-1.68	-0.99
	125	125			-1.08	-1.67	-0.87	-0.38
2	150	100	**0.469**	**0.8**	-1.16	-1.06	0.81	-1.12
	150	125			-1.12	-1.37	-1.99	-0.42
	150	150			-1.24	-1.05	0.77	-0.91
	175	125			-1.07	-1.55	-0.36	-0.58
	75	100			-1.67	-1.93	0.25	-1.19
	75	125			-1.61	-2.19	-0.34	-0.06
	75	150			-1.67	-1.83	2.67	-0.60
	100	**100**			-1.87	-1.79	1.28	**-1.84**
3	100	125	**0.455**	**0.8**	-1.84	-1.85	-2.22	-0.88
	100	150			-1.95	-1.56	0.82	-1.46
	100	175			-1.80	-1.71	-0.59	-1.21
	125	100			-1.74	-1.86	-0.18	-0.80
	125	125			-1.76	-2.23	0.87	-0.96
	75	75			-2.21	-2.96	0.45	-0.65
	100	75			-2.33	-2.45	2.19	-1.20
4	100	100	**0.441**	**0.8**	-2.69	-2.15	0.86	-2.01
	125	75			-2.24	-2.63	-0.77	-1.07
	125	**100**			-2.56	-2.29	1.06	**-2.26**
	75	75			-3.00	-3.64	-1.71	-1.82
	75	100			-3.22	-2.96	0.39	-2.37
5	75	125	**0.427**	**0.8**	-3.14	-3.20	-0.76	-2.33
	100	75			-3.22	-3.28	-0.81	-2.26
	100	**100**			-3.55	-2.84	-0.46	**-3.30**

Table 6-13 - Calculation of combined stress parameter - optimal designs in bold

No. of cells	Σ_{comb} (G = 15 MPa)	Σ_{comb} (G = 25 MPa)
1	-0.46%	-0.56%
2	-0.99%	-1.18%
3	-1.64%	-1.84%
4	-2.14%	-2.26%
5	-3.18%	-3.30%

Table 6-14 - Variation in combined stress term with number of cell blocks

No. of cells	$\Delta\sigma_{max}$ (G = 15 MPa)	$\Delta\sigma_{max}$ (G = 25 MPa)
1	-0.48%	-0.59%
2	-0.93%	-1.14%
3	-1.65%	-1.87%
4	-2.38%	-2.56%
5	-3.41%	-3.55%

Table 6-15 - Variation in facesheet stress component

No. of cells	$\Delta\sigma_{max}$ (G = 15 MPa)	$\Delta\sigma_{max}$ (G = 25 MPa)
1	-0.42%	-0.50%
2	-1.10%	-1.26%
3	-1.62%	-1.79%
4	-1.69%	-1.71%
5	-2.76%	-2.84%

Table 6-16 - Variation in core stress component

No. of cells	Δz_{max} (G = 15 MPa)	Δz_{max} (G = 25 MPa)
1	-1.54%	-1.60%
2	-3.14%	-3.25%
3	-4.87%	-4.97%
4	-6.53%	-6.63%
5	-8.67%	-8.68%

Table 6-17 - Variation in maximum deformation

No. of cells	Δa_{max} (G = 15 MPa)	Δa_{max} (G = 25 MPa)
1	+0.68%	+0.83%
2	+1.95%	+1.97%
3	+2.14%	+2.52%
4	+3.21%	+3.73%
5	+2.42%	+3.37%

Table 6-18 - Variation in maximum acceleration

6.8.3 Detailed Modelling

As the final tradeoff was conducted using a coarse model, it was considered appropriate to remodel the final chosen designs using a finer mesh and more modes to improve the accuracy of the results. For this, the 5 mm mesh was used once more (using the elements shown in Table 6-19) in place of the 10 mm mesh, and the first four symmetric modes were employed, rather than two. The sensitivity of the results to the change in the model's specifications varied according to the chosen criteria.

Component	Element type	Number
Facesheets	Shell181 – 4 Node Linear Quadrilateral Shell	5000
Honeycomb	Solid186 – 20 Node Quadratic Hexahedron	9376
Cells	Solid186 – 20 Node Quadratic Hexahedron	560
Insert	Solid186 – 20 Node Quadratic Hexahedron	64
Contact	Targe170, Conta173, Conta174	25448
Total	-	**40448**

Table 6-19 - Elements used in panel model (for 1-1 configuration)

The results for stress deviate slightly from the coarser model, but the trends of the results for combined stress and facesheet stress are unchanged, as shown in Table 6-20 and Table 6-21. The results for core stress, shown in Table 6-22, follow a similar pattern to the coarse model, but are more linear. Since the general trends, rather than the precise results, are of importance, these results are still adequately robust.

In the case of deformation (Table 6-23), the effect of adopting the MFS is virtually unchanged when the finer model is used. This is as expected, as deformation is, typically, due almost entirely to the first mode of vibration. The table shows these results have virtually no sensitivity to modes beyond the first.

The finer model gives results for acceleration markedly different to the coarse model. Table 6-24 shows that the peak acceleration change predicted by the fine model is, in most cases, negative rather than positive. The results are also less linear and even more dependent on the shear modulus of the battery than for the coarse model. The observation that an improvement in the panel's acceleration response is predicted is a positive one; however, it is clear that the higher modes of vibration included in this model have a significant effect on the acceleration response. Thus, the acceleration tests were rerun once more, this time using eight symmetric modes. The results of these models are shown in Table 6-25.

No. of cells	Σ_{comb} (G = 15 MPa)		Σ_{comb} (G = 25 MPa)	
	Coarse	Fine	Coarse	Fine
1	-0.46%	-0.39%	-0.56%	-0.48%
2	-0.99%	-0.94%	-1.18%	-1.10%
3	-1.64%	-1.54%	-1.84%	-1.70%
4	-2.14%	-2.24%	-2.26%	-2.37%
5	-3.18%	-3.05%	-3.30%	-3.12%

Table 6-20 - Variation in combined stress term with number of cell blocks

No. of cells	$\Delta\sigma_{max}$ (G = 15 MPa)		$\Delta\sigma_{max}$ (G = 25 MPa)	
	Coarse	Fine	Coarse	Fine
1	-0.48%	-0.40%	-0.59%	-0.52%
2	-0.93%	-0.95%	-1.14%	-1.15%
3	-1.65%	-1.69%	-1.87%	-1.90%
4	-2.38%	-2.50%	-2.56%	-2.67%
5	-3.41%	-3.38%	-3.55%	-3.49%

Table 6-21 - Variation in facesheet stress component

No. of cells	$\Delta\sigma_{max}$ (G = 15 MPa)		$\Delta\sigma_{max}$ (G = 25 MPa)	
	Coarse	Fine	Coarse	Fine
1	-0.42%	-0.38%	-0.50%	-0.43%
2	-1.10%	-0.91%	-1.26%	-1.00%
3	-1.62%	-1.29%	-1.79%	-1.36%
4	-1.69%	-1.77%	-1.71%	-1.83%
5	-2.76%	-2.43%	-2.84%	-2.41%

Table 6-22 - Variation in core stress component

No. of cells	Δz_{max} (G = 15 MPa)		Δz_{max} (G = 25 MPa)	
	Coarse	Fine	Coarse	Fine
1	-1.54%	-1.48%	-1.60%	-1.54%
2	-3.14%	-2.99%	-3.25%	-3.12%
3	-4.87%	-4.75%	-4.97%	-4.84%
4	-6.53%	-6.38%	-6.63%	-6.43%
5	-8.67%	-8.64%	-8.68%	-8.55%

Table 6-23 - Variation in maximum deformation

No. of cells	Δa_{max} (G = 15 MPa)		Δa_{max} (G = 25 MPa)	
	Coarse	Fine	Coarse	Fine
1	+0.68%	-1.31%	+0.83%	-0.53%
2	+1.95%	-1.04%	+1.97%	0.01%
3	+2.14%	-5.42%	+2.52%	-2.56%
4	+3.21%	-8.77%	+3.73%	-5.45%
5	+2.42%	-3.79%	+3.37%	-6.19%

Table 6-24 - Variation in maximum acceleration

No. of cells	Δa_{max} (G = 15 MPa)			Δa_{max} (G = 25 MPa)		
	Coarse	Fine	Fine (8 modes)	Coarse	Fine	Fine (8 modes)
1	+0.68%	-1.31%	0.40%	+0.83%	-0.53%	0.75%
2	+1.95%	-1.04%	-1.13%	+1.97%	0.01%	-1.09%
3	+2.14%	-5.42%	-5.62%	+2.52%	-2.56%	-3.25%
4	+3.21%	-8.77%	-5.85%	+3.73%	-5.45%	-2.68%
5	+2.42%	-3.79%	-8.83%	+3.37%	-6.19%	-5.56%

Table 6-25 - Variation of acceleration at panel centre for 2, 4 and 8 mode models

Table 6-25 indicates that, whilst the 8-mode results are still not particularly smooth, they follow a similar pattern to the 4-mode results. The shear stiffness of the cells continues to have a notable effect on the results, with the four cells per quarter values differing by a factor of two. Significantly, however, the results remain positive (i.e., the peak acceleration is reduced in almost all cases) and, as for previous models, it is the lower cell stiffness that gives a large reduction in acceleration. It would be necessary to obtain experimental results to give a truly accurate prediction of the acceleration that would occur on a real MFS panel, but these results are sufficient in that the more detailed models consistently show that the acceleration is reduced.

It should be noted that, for the 4- and 5-cell block models using 8 modes, the true peak acceleration occurs at the locality of the batteries themselves, rather than the centre of the panel as for other cases. However, the acceleration at the centre is still

used for the comparison. There are two reasons to neglect the higher acceleration in the vicinity of the batteries: firstly, the area over which this acceleration occurs is very small, as shown in Figure 6-19, and thus could easily be avoided when placing components on the panel. Secondly, and more importantly, the presence of the battery means that this part of the panel cannot contain an insert, greatly reducing the likelihood of any components (acceleration-sensitive or otherwise) being mounted upon it.

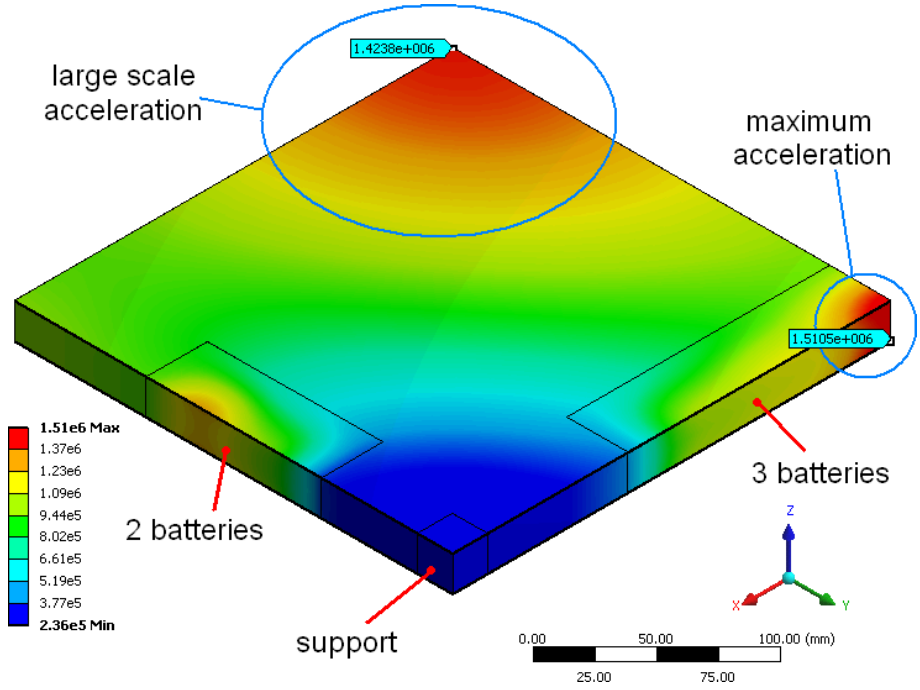

Figure 6-19 - Distribution of acceleration over panel area.

Maximum response occurs in small area over battery; area of interest is centre of panel. Scale shows RMS acceleration in mms^{-2}. This image shows a 3-2 configured panel.

6.9 Conclusions

FE modelling has shown that a multifunctional panel can have dynamic structural performance comparable to a conventional arrangement of a structure and separate battery pack. The positive impact of redistributing the battery cells to a location in the core of the panel and eliminating the parasitic mass of the battery enclosure

outweighs the negative effect of replacing the core with the less stiff battery cells. A simple design tradeoff can produce panels with reduced stress and peak deformation, and while the modelling of the peak acceleration response of the panel was less consistent, the predicted response of the majority of the panel was superior in most cases.

The models show that a structure designed to minimise stress, large-scale deformation and/or acceleration can achieve the mass reductions described in Chapter 3. In this study, the density of the PLI cells (1840 kgm^{-3}) that replace the honeycomb core (density of 100 kgm^{-3}) leads to a value for η_{para} of -0.054, showing that the minimum value for an MFS considered in the parametric study is achievable and, thus, that the mass savings calculated in Chapter 3 could be realised. Indeed, given that the performance of the MFS exceeds that of the conventional structure in some cases, it is probable that a design fully optimised for these attributes could save yet more mass.

This result for stress has the most positive implications, as this criterion is a requirement for any structure: the requirement to sustain loads without structural failure. In the absence of particular stipulations from the components mounted upon it, therefore, mass can be saved by adopting an MFS approach to structural design.

If solar cells are mounted directly to a panel, then excessive deformation may cause them to detach from it or crack. This particular case is notable, as integrating these two elements of the power subsystem provides other system-level benefits (such as shortening cable paths). The significant improvement in performance, and consequent decrease in mass, that may be achieved by adopting an MFS may go some way to offsetting the mass of the control system required prevent thermal damage to PLI cells in a solar array [88].

A panel used to mount delicate equipment appears, from the work presented here, to be a less suitable candidate for use as a multifunctional structure. The FE models predicted a reduction in acceleration for the MFS panel, but these results were the

least consistent of the three criteria studied; in addition, it was shown in Chapter 5 that the FE model's predictions of an MFS panel's performance were not entirely accurate. Thus, while it is reasonable to assume that there would be no increase in acceleration, it would not be conservative to expect reductions as large as those that the model suggests could occur. Nevertheless, simply maintaining structural performance is sufficient to achieve the mass savings as calculated in Chapter 3.

7 Discussion

7.1 Issues and Costs of MFS Implementation

Whilst the main benefits of multifunctional structures have been described and, in the case of mass savings, quantified, these benefits would be offset by various penalties. This section shall describe the potential disadvantages that could be encountered when applying a powerstructure to a real spacecraft.

7.1.1 Space Qualification Issues

Any cells used in a powerstructure would need to undergo the same qualification tests as they would for use in a standard spacecraft battery (as described in Section 4.1) prior to use in an MFS. To confirm their reliability, it may also be desirable to use the same cells in a conventional spacecraft battery as a part of this.

To apply the cells to an MFS, it would be necessary to perform additional testing and design work, such as that described in this thesis. As well as having an associated cost in terms of the labour required to undertake this work and the time required to perform it, the requirement for testing specific to the MFS application also has the potential to limit the benefits that may be achieved by using it.

In order to be worthwhile, the MFS must allow mass to be saved compared to a conventional battery using the latest technology. If the process of qualifying an existing cell for use in an MFS is faster and cheaper than qualifying a new cell from scratch, the MFS approach provides a lower mass solution until a superior cell is available. On the other hand, it is possible that, in the time it takes to qualify a cell for use as a structural element, a cell with higher performance will become available for use in a conventional battery.

7.1.2 Design and Manufacture

Whilst mass and volume savings may be translated into a saving in a spacecraft mission's overall cost through reduction in launching costs, it is also likely that using a multifunctional structure will add some complexity, and hence cost, to its design and manufacture. The benefits of using a multifunctional structure would need to be weighed carefully against this cost.

One of the most obvious practical implications is the increase in cabling required to connect the cells together to form the battery. Optimal structural performance may require the cells to be distributed widely throughout the structure, requiring additional cabling. This would lead to a small amount of additional mass and, more significantly, an increase in complexity of the design and AIV (assembly, integration and verification) process. On the other hand, the ability to route power cables through the structure could simplify the arrangement of the harness, as other subsystems could use the same cable paths as the battery. The importance of this factor would be highly dependent on the internal configuration of the spacecraft.

Secondly, during design process, the structure may need to be modified to accommodate changes in the size or mass of other components. Likewise, the battery needs to be modified to account for changing power requirements. By marrying the functional elements of the battery and structure, these tasks are also combined, as a modification to the structure may mean rearranging the layout of the battery, and a modified power requirement would require a slight redesign of the structure. In either case, those responsible for the power and structural subsystems would be required to collaborate more closely than would be necessary for a conventional arrangement. Hence, every design iteration of a spacecraft using a multifunctional power structure would be longer than for a conventional spacecraft. This would, however, be offset by the fact that configuring the spacecraft would be simpler due to the elimination of the battery from the bus.

Finally, when the remainder of the design is frozen, the increased structural complexity of the MFS means that the final structural optimisation would take more time. In order to take full advantage of the mass savings the multifunctional structure affords, it would be necessary to optimise its mechanical performance. However, placement of the cells would, in a real situation, represent not only a structural challenge; the optimal location of the cells would have to take into account factors that could affect the performance of the battery, such as the cable paths, the location of inserts and brackets and the thermal environment. In a small and relatively simple spacecraft, these constraints could be dealt with simply but, for large spacecraft, this could represent a significant multi-objective problem.

In some cases, the practicality of adopting an MFS may be limited by the approach taken to manufacturing and designing individual components of the spacecraft. If the structure of the spacecraft is outsourced to an external contractor, then the difficulty of manufacturing the MFS may increase dramatically unless the cells are to be inserted using cold-bonding after delivery. Equally, if the prime contractor does not assemble batteries in-house, a multifunctional approach would place constraints on the battery suppliers to use cells suitable for the MFS, and supplying cells in a nonstandard form would probably lead to increased costs. Thus, spacecraft manufacturers that do not have the expertise to assemble their own structures and batteries could encounter some difficulty in making use of an MFS.

7.2 Mission Profile and MFS Applicability

Mass savings are an important design driver, but other factors may affect the usefulness of an MFS to a particular spacecraft. These factors are not easily quantified in most cases, but their influence is discussed here.

Given that the ultimate aim of saving mass in the spacecraft is to save money by reducing launch cost, the proportion of the total mission cost that this comprises must be taken into account. Two principal factors deciding this are the orbit the spacecraft

is to enter, and the duration of its mission. A higher orbit necessarily increases launch cost, as do other factors such as orbital inclination. Conversely, a longer mission means that more of the financial outlay over the lifetime of the spacecraft is made up by ground station costs, reducing the importance of launch costs.

If the launch makes up a smaller proportion of the cost of the mission, thus, it may be more desirable to adopt a "tried and tested" approach that minimises risk and ensures the spacecraft performs properly throughout its projected lifetime. In particular, the use of standard bus designs reduces cost by eliminating much of the need to design a new structure and power system and increasing reliability, advantages that would have to be sacrificed to save mass using a custom-designed multifunctional structure. Conversely, a short-duration mission in a higher delta-V orbit would place less importance on reliability, as the cost of launch would make up much of the total mission cost. In this case, a multifunctional structure would be more likely to provide advantages at the mission level.

7.3 Parametric Study

In order to consider a wide variety of spacecraft designs in the parametric study described in Chapter 3 and the design process in Section 6.2, various assumptions were made to translate the attributes of real spacecraft into simple performance parameters. This section will assess the validity of these assumptions.

7.3.1 Mass Reduction Calculations

The typical values for parasitic mass fraction were based on limited historical data. The precise composition of a spacecraft battery pack is not something that is regularly published. The design of such batteries does not vary greatly, and, given that this technology is relatively mature, it seems likely that significant improvements are not possible. Nevertheless, it is possible that a redesigned battery could eliminate some

parasitic mass without the costs associated with an MFS. In this case, there would not be a significant reduction in volume.

In addition, battery enclosures currently in use are, naturally, for use with current battery technology, which in most cases still means cylindrical cells. Cells of this type are relatively delicate and do not pack easily, whilst it is to be expected that robust, prismatic PLI cells would be much easier to pack; in [61], for example, it is suggested that PLI cells could be mounted directly to the structure using adhesive tape. Whilst this would not be practical on a large scale, it does illustrate that PLI cells need not be mounted in a traditional way. Thus, whilst the baseline value for η_{para} was a reasonable one, it should be noted that a conventional battery using PLI cells could have a lower proportion of parasitic mass. On the other hand, FE models predict superior structural performance from the MFS compared to conventional panels in the majority of cases, meaning that more parasitic mass could be eliminated than was considered in the study. As the change in the parameter is of principal interest, the absolute values of the boundaries do not significantly affect the results, provided they are realistic.

The terms used to determine the mass savings due to volume reduction, δ_{vol} and η_{pack}, were based on historical data and conservative estimation respectively. In truth, the change in volume would not occur in a linear fashion, and the calculations pertaining to this aspect should be seen more as average predictions. The actual volume change resulting from an MFS approach would be entirely dependent on the configuration of the spacecraft; the removal of one box may have little effect on overall size if the remaining components cannot be rearranged into a smaller volume. On the other hand, if the configuration is an "untidy" one with a large amount of wasted space, it may be that the space utilisation becomes far more efficient if a multifunctional battery is used. A simple spacecraft, containing a smaller number of discreet boxes, would be more likely to fall into the latter category.

7.3.2 Independence of Parameters

An assumption implicit in the study is that all of the parameters considered are independent of one another. This section shall discuss how true this is likely to be in reality and the impact any discrepancies would have.

Parasitic Mass Fraction

Since the proportion of parasitic mass would be affected by the type of cells used, this parameter would show some correlation with the SEC parameter, as described above.

Specific Energy Capacity

SEC is a fundamental property of the cells used, and so ostensibly it should be fully independent; however, it does seem probable that a spacecraft with a large energy storage requirement would have a greater need to use a cell with higher performance. Hence, in practice one would expect to see a positive correlation between SEC and SER.

This has positive implications for the usefulness of an MFS: if a spacecraft design already uses a high-performance cell, there is less potential to save mass by using a different one. As such, an alternative approach (such as MFS) would have to be taken if more mass needs to be trimmed from the design.

Specific Energy Requirement

The SER is determined by the mass and power requirements of all of the spacecraft's subsystems. The only other parameter to affect this is the structural mass fraction: a higher value for α_{stru} means there is more mass that does not require power (structure, as opposed to active components of the spacecraft), thus reducing SER. However, since both parameters are measured attribute of the spacecraft, this correlation does not affect the results.

Structural Mass Density

α_{stru} affects the structural mass density, as a higher structural mass without an increase in volume would increase the parameter. Without knowing the precise reason for the higher structural mass fraction, it is difficult to establish how this would affect the results. If the added mass were due to additional sandwich panels, however, this would increase the likelihood of finding suitable locations for MFS within the structure, which would be of particular benefit where δ_{vol} was high. Hence, the correlation between these two parameters is has positive implications, as it increases the practicality of an MFS where the potential benefits are highest.

Packing Efficiency

A larger parasitic mass fraction would lead to a larger "parasitic volume" and hence a lower packing efficiency; this effect would, however, be relatively small, as the majority of the additional volume of the battery is determined by the cells' ability to tessellate without wasted space. This factor may be of greater importance; in the examples used to set the limits of the study, the lower bound corresponded to a cylindrical cell, and the upper to a prismatic cell. The cell configuration, therefore, does affect this parameter. However, there is nothing to suggest that cell configuration has a major correlation with SEC, as state-of-the-art PLI and cylindrical lithium cells have comparable performance.

Structural Mass Fraction

An inverse relationship would be expected to occur between structural mass fraction and SER. A spacecraft with a high power requirement would require larger solar arrays, meaning that less of the spacecraft was within the primary bus structure, and thus the structure was a smaller proportion of the total mass. This is in contrast to the correlation between δ_{vol} and α_{stru}; a higher SER implies a greater potential for mass reduction, but less structure leads to less possibility to adopt an MFS battery.

Specific Multifunctional Energy Capacity

How much energy storage one can practically incorporate within a panel is necessarily affected by how much energy the cells can store. Due to this, the optimisation results from Chapter 6 are only applicable to an MFS using a cell with performance comparable to the PoLiFlex cell employed in the FE models.

Multifunctional Potential

There appears to be no dependence on other parameters.

7.4 Experimental Results

The experimental testing on the battery cells and panel should be seen as a feasibility study, or proof of concept. Additional work would be required to qualify the MFS for use in a real application.

Firstly, no substantial consideration was given to selecting the most appropriate cell model for use in an MFS, as this would be dependent on the particular application and the cells available at the time. It was more convenient to use cells that displayed good electrical characteristics, were readily available and convenient for the testing in question. Taken in addition to the work described in [61], the tests on these cells indicate that cells of the PLI type are acceptable for use in a spacecraft MFS. However, for implementation it would be necessary to undertake a more detailed tradeoff on the cell selection and to repeat tests on the precise make and model of cell that was to be used.

Given the nature of PLI cells, there is no reason to suppose that other models, or cells from another manufacturer, would be less mechanically robust than would those tested in this work. If some cells were found to be more susceptible to damage from vibration, then, given the large range of cells available, an alternative could easily be found. The other test results – on the shear stiffness of the cells and the minor damage

caused by composite curing – are less of an issue. Given that the stiffness of the cells was so poor, there are few negative implications of an alternative cell having different performance. A higher stiffness would improve performance, whilst a lower stiffness would make little difference due to the PoLiFlex cells' negligible load-carrying capability. Likewise, if another cell suffered greater performance degradation due to the curing environment, the fact is that, in most cases, a cold-bonding method would have been preferable anyway.

Testing on the cells' ability to survive vibration gave positive results, though the tests were not comprehensive. The tests with the cells restrained in the clamp, in Section 4.2 did not show any performance effect from applied vibration. Although there was considerable scatter in the results, a performance loss within the error of the experimental data would not have a significant impact on performance. However, whilst the cells continued to function without evidence of performance loss when subjected to significant shear loading and used as a component in a loaded panel (Sections 4.3 and 5.4 respectively), the cells were not fully characterised. It would be necessary to establish whether a particular level of deformation had an effect on the electrical performance of a cell before designing a real MFS, as this would determine where in a panel the cells could be placed.

7.5 FEA Modelling

The main issue to address in this regard is the correlation between the FEA models described in Chapter 6 and a real panel. Section 5.4 shows that an FEA model can predict the deformation of an MFS panel reliably, which in turn suggests that the stress levels should be accurate. The fact that the best results for stress and deformation have a smooth, linear relationship with the number of battery cells in the panel supports the assumption that the calculated improvement in performance is not simply due to random errors in the FEA modelling procedure, as does the robustness of the results when modelling the panel using a different mesh and higher modes.

The poorer results for acceleration mean that assertions regarding the level of acceleration in the panel cannot be relied upon to the same extent. The less smooth relationship between predicted acceleration and the number of cells in the panel, as well as the extreme sensitivity of the results to the attributes of the model, confirm this. However, the 4- and 8-mode models agreed reasonably well, and predicted an improvement in the response. Even allowing for possible errors in the results, the acceleration results do not suggest that the structural performance of the MFS would be inadequate to its task.

7.6 Summary

In spite of quantitative benefits, qualitative factors suggest that spacecraft missions with long projected lifetimes, many internal components and standardised subsystems stand to gain less, in terms of mission costs, from using a multifunctional powerstructure than small, simple and novel craft.

Referring to Chapter 3, small spacecraft generally have higher structural mass densities, and thus stand to lose more mass from volume reduction. Hence, small spacecraft, with large power requirements and comparatively few internal components stand to save the most mass through using an MFS. Spacecraft with comparatively short service lives, for which a standard structure and/or battery is unavailable, and whose manufacturer is able to integrate the battery and manufacture the structure in-house, stand to make the greatest savings in cost.

The positive results of experimental tests on PLI cells in this and other work show the feasibility of the MFS concept. Additional negative results may add constraints to the design of an MFS, but the fact that an MFS can achieve acceptable structural performance using cells with negligible structural performance, and that the cells themselves can sustain substantial vibration acceleration without performance loss, means that benefits can still be realised.

8 Conclusions

A multifunctional power structure saves mass from a spacecraft incorporating the secondary power subsystem (the electrical battery) into the primary structure. By using the structural properties of a non-structural element, or at least by eliminating the mechanical housing of the power subsystem, inert materials may be eliminated, and the requirement to allot internal volume to the battery is removed.

In this thesis, it has been seen that adopting a PLI cell-based multifunctional powerstructure could reduce the mass of a spacecraft by as much as 2-3% when compared to a baseline of lithium-ion cells currently in use, and by 0.5-1% compared to a using the same PLI cells in a conventional structure. The system-level impact of using an MFS has not previously been addressed in this manner, and the parametric study used to make these assessments can equally be applied to other MFS concepts where sufficient data is available [89].

It was also shown that, in spite of the benefits of multifunctional powerstructures, existing proposals to take advantage of these benefits would be financially costly. All of the MFS technologies in the literature require the use of custom-built electrical cells. Whilst it has been shown that significant reductions in mass can be realised through this technology, the range of applications for which an MFS is advantageous is limited. Thus, the small production quantities of any MFS using custom-built cells would result in high manufacturing costs. Using commercially available PLI cells as part of a sandwich panel core presents an alternative that would allow some of these benefits to be realised at a lower financial outlay.

An MFS has two functions, structural and electrical, and must be superior or equal to a conventional arrangement in both aspects, and at a lower mass, in order to be worthwhile. Regarding the electrical performance of an MFS of this type, commercial PLI cells have demonstrated the ability to survive the vibration environment of a

simulated spacecraft launch without degradation in their electrical performance. The practicality of manufacturing an MFS panel using an elevated temperature cure has also been investigated. A functioning powerstructure was produced to demonstrate that such an approach is feasible; it was found that the performance of the cells was reduced somewhat, suggesting that fixing the cells with an adhesive that cures at room temperature, and after assembling the remainder of the panel, would be preferable.

Mechanical testing measured the structural properties of the cells relevant to the application of a sandwich panel core; their structural performance was found to be lower than a conventional honeycomb material, though, once more, they showed no signs of electrical degradation when subjected to shear strain. The completed MFS panel was also subjected to dynamic testing that showed no damage to the cells in the core, and demonstrated the ability of FE models to predict its behaviour.

FE models were then used to demonstrate that, in spite of the cells' poor mechanical properties, careful placement of the cells allows dynamic mechanical performance to improve in terms of stress and deformation. The limitations of the FE method when predicting high frequency vibrations meant that results pertaining to the peak acceleration were less conclusive, though the prediction was still positive. The FE model of the experimental tests on the real MFS panel showed that the accuracy of acceleration predictions was less good than for stress and deformation. It was thus demonstrated that an MFS using commercial PLI cells could be expected to perform both the electrical and structural functions of its conventional counterpart.

The impact of these results in the wider context of spacecraft design was discussed, the conclusion being that the circumstances of a spacecraft's design, manufacture and operation could have a notable effect on the achievable benefits at the mission level. Specifically, small spacecraft with high power demands and comparatively simple internal arrangements stand to make the most substantial cost savings if their

subsystems are to be manufactured substantially by a single contractor. The accuracy and importance of the results was also considered.

This thesis has shown that substantial mass savings may be made in small spacecraft with high power demands through combining the primary structure and electrical battery to form a multifunctional powerstructure. By using commercially available cells to form the multifunctional battery, this mass saving can be translated into a financial saving, by the resultant reduction in launching cost. Whilst the cost of implementing an MFS could be prohibitive for some spacecraft types, a substantial benefit could be realised for short missions whose platform is manufactured by a single contractor.

Further Work

System Engineering

Whilst this thesis has presented an investigation of the more important system-level implications of adopting an MFS, a more thorough treatment of this subject would be highly beneficial to the field. Extending the study in Chapter 3 to a wider and more detailed investigation of space missions would be the first stage in this, allowing more precise numbers to be placed on the cost savings available from an MFS, both due to mass reduction and directly to volume saving.

The other aspect of such a study would be an assessment of the possible disadvantages and negative implications that an MFS could have. This has been given some consideration in the discussion of this thesis, but a more extensive treatment of the subject, together with estimations of cost and suggestions for mitigation, would be a logical continuation of the work.

Electrical Performance

The selection of an appropriate type of cell for this application would require a great number of factors to be considered. For this initial study, the cell model was chosen largely based on availability, but a comprehensive assessment of a variety of cells would be necessary to produce a reliable MFS, and beneficial to its performance.

An investigation into the structural performance of various PLI cells would be of potential interest. The Varta cells tested in the course of this work exhibited poor mechanical properties, but there is no reason to assume that similar cells produced by other manufacturers (such as Sanyo, IBT, Kokam, Danionics, &c.) would not be superior in this regard.

The more important consideration, however, would be a rigorous campaign to assess all of the potential impact the MFS could have on the cells, and make a selection on that basis. Factors such as the effect of the thermal environment or mechanical loading could have a notable effect on electrical performance, but to measure this would require extensive testing (particularly in the latter case). However, without knowing, for example, if a certain level of shear stress might cause long-term degradation in capacity, it would be impossible to accurately predict the in-service electrical performance of the MFS.

Structural Design

It has been shown, through FE models, that the panel configuration considered in Chapter 6 is able to maintain adequate structural performance, when converted to a multifunctional arrangement. However, the subject would benefit greatly from a more detailed investigation of two additional aspects of the structural performance.

Firstly, it would be important to consider a wide variety of panel configurations, and conduct a more thorough optimisation of their layouts. This would identify which types of panel show the most positive performance change when converted to an MFS, in turn allowing an assessment to be made of how frequently such panels are encountered in spacecraft. Ultimately, this would lead to a quantification of the expected change in structural performance that an MFS approach could achieve. Such an investigation could be conducted through a Monte Carlo analysis or by case studies of existing spacecraft.

Secondly, constructing optimised MFS demonstration panels for experimental tests would allow a more thorough validation of the FE models used to assess their structural performance.

List of References

1. Chmielewski, A.B., Das, A., Cassapakis, C., Allen, D., Schafer, W.J., Sercel, J., Deligiannis, F., Piszczor, M., Jones, P.A., Barnett, D.M., Rawal, S.P. and Reddy, T., 1996. *New Millennium Program Power Technology*. Proceedings of the Intersociety Energy Conversion Engineering Conference, 11-16 August 1996, Washington, DC, United States.

2. Futron Corporation, 2002. *Space Transportation Costs: Trends in Price per Pound to Orbit 1990-2000*. Futron Corporation, Bethesda, MD, United States.

3. Aglietti, G.S., Schwingshackl, C.W. and Roberts, S.C., 2007. *Multifunctional Structure Technologies for Satellite Applications*. The Shock and Vibration Digest, v39(5): pp381-391.

4. Clark, C., Summers, J. and Armstrong, J., 2000. *Innovative Flexible Lightweight Thin-Film Power Generation and Storage for Space Applications*. Proceedings of the Intersociety Energy Conversion Engineering Conference, 24-28 July 2000, Las Vegas, NV, United States.

5. Rawal, S.P., Barnett, D.M. and Martin, D.E., 1999. *Thermal Management for MFS*. IEEE Transactions on Advanced Packaging, v22(3): pp379-383.

6. Barnett, D.M. and Rawal, S.P., 1997. *MFS Technology Experiment on Deep Space 1 Mission*. IEEE Aerospace and Electronic Systems Magazine, v14(1): pp13-18.

7. Seepersad, C.C., Dempsey, B.M., Allen, J.K., Mistree, F. and McDowell, D.L., 2004. *Design of Multifunctional Honeycomb Materials*. AIAA Journal, v42(5): pp1025-1033.

8. Wirtz, R., Zhao, T. and Jiang, Y., 2004. *Thermal and Mechanical Characteristics of a Multifunctional Thermal Energy Storage Structure*. The Ninth Intersociety

Conference on Thermal and Thermomechanical Phenomena in Electronic Systems (ITHERM '04), 1-4 June 2004, Las Vegas, NV, United States.

9. Elzey, D.M., Sofia, A.Y.N. and Wadley, H.N.G., 2004. *A Shape Memory-Based Multifunctional Structural Actuator Panel*. International Journal of Solids and Structures, v42(7): pp1943-1955.

10. Miller, M.B., Clarke, R., Furrow, P., Bell, C. and Hyer, M., 2000. *Multifunctional Composite Structures for Space Applications*. Proceedings of SPIE - The International Society for Optical Engineering, v3991: pp152-163.

11. Pei, Q., Rosenthal, M., Pelrine, R., Stanford, S. and Kornbluh, R., 2003. *Multifunctional Electroelastomer Roll Actuators and Their Application for Biomimetic Walking Robots*. Proceedings of SPIE - The International Society for Optical Engineering, v 5051 pp. 281-290.

12. Watkins, A.N., Ingram, J.L., Jordan, J.D., Wincheski, R.A., Smits, J.M. and Williams, P.A., 2004. *Single Wall Carbon Nanotube-Based Structural Health Sensing Materials*. 2004 Nanotechnology Conference and Trade Show - Nanotech 2004, March 7-11 2004, Boston, Massachusetts.

13. Wood, K.H., Brown, T.L., Wu, M.C. and Gause, C.B., 2001. *Fibre Optic Sensors for Cure/Health Monitoring of Composite Materials*. 3rd International Workshop on Structural Health Monitoring, September 11-14 2001, Stanford, California, United States.

14. Zuckermandel, J.W., Enger, S., Gupta, N. and Summers, J., 2007. *Modular, Thin Film Solar Arrays for Operationally Responsive Spacecraft*. 2007 IEEE Aerospace Conference, March 3-10 2007, Big Sky, MT, United States.

15. Anon, 2004. *Multifunctional Batteries Build Vehicle Structures*. Advanced Materials and Processes, v162(3): pp15-16.

16. Lyman, P.C. and Feaver, T.L., 1998. *Powercore™: Combining Structure and Batteries for Increased Energy to Weight Ratio*. IEEE Aerospace and Electronic Systems Magazine, v13(9): pp39-42.

17. Marcelli, D., Summers, J. and Neudecker, B., 2002. *Libacore II: Power Storage in Primary Structure*. Collection of Technical Papers - AIAA/ASME/ASCE/AHS/ASC Structures, Structural Dynamics and Materials Conference, April 22-25 2002, Denver, CO, United States.

18. Metzger, W., Westfall, R., Hermann, A. and Lyman, P., 1998. *Nickel Foam Substrate for Nickel Metal Hydride Electrodes and Lightweight Honeycomb Structures*. International Journal of Hydrogen Energy, v23(11): pp1025-1029.

19. Neudecker, B.J., Benson, M.H. and Emerson, B.K., 2003. *Power Fibres: Thin-Film Batteries on Fibre Substrates*. 14th International Conference on Composite Materials (ICCM 14), July 14-18 2003, San Diego, CA, United States.

20. Wong, E.L., Baechle, D.M., Xu, K., Carter, R.H., Snyder, J.F. and Wetzel, E.D., 2007. *Design and processing of structural composite batteries*. SAMPE '07: M and P - From Coast to Coast and Around the World, June 3-7 2007, Baltimore, MD, United States.

21. Qidwai, M.A., Thomas, J.P. and Matic, P., 2002. *Design and Performance of Composite Multifunctional Structure-Battery Materials*. Proceedings of the American Society for Composites, Seventeenth Technical Conference, 21-28 October 2002, West Lafayette, IN, United States.

22. Qidwai, M.A., Thomas, J.P. and Matic, P., 2002. *Structure-Battery Multifunctional composite Design*. Proceedings of SPIE - The International Society for Optical Engineering, v4698: pp180-191.

23. Thomas, J.P., Keennon, M.T., DuPasquier, A., Qidwai, M.A. and Matic, P., 2003. *Multifunctional Structure-Battery Materials for Enhanced Performance in Small UAVs*. ASME International Mechanical Engineering Congress, November 15-21 2003, Washington, DC., United States.

24. Thomas, J.P. and Qidwai, M.A., 2005. *The design and application of multifunctional structure-battery materials systems*. Journal of Materials, v57(3): pp18-24.

25. Queheillalt, D.T., Katsumi, Y. and Wadley, H.N.G., 2001. *Electron Beam - Directed Vapour Deposition of Multifunctional Structures*. Materials Research Society Symposium, v372. Materials Research Society.

26. Olson, J.B., Feaver, T.L. and Lyman, P.C., 2003. *Structural Lithium-ion Batteries Using Dual-functional Carbon Fabric Composite Anodes*. Proceedings of the 14th International Conference on Composite Materials, July 2003, San Diego, CA, United States.

27. Olson, J.B., Shaw, Z., Jennings, J., Lyman, V., Feaver, T. and Lyman, P., 2003. *Structural High-Power Energy Storage Panels Using Dual Functional Carbon Fabric Composite Electrodes*. Space Power Workshop, April 2003, Redondo Beach, CA, United States.

28. Sarafin T.P. (Editor), 1995. *Spacecraft Structures and Mechanisms: From Concept to Launch (Space Technology Library).* Berlin: Springer.

29. Vincent, C. and Scrosati, B., 1997. *Modern Batteries: An Introduction to Electrochemical Power Sources.* 2nd edition. Oxford: Butterworth-Heinemann.

30. Cole, J.H., Eskra, M. and Klein, M., 2000. *Bipolar Nickel-Metal Hydride Batteries for Aerospace Applications*. IEEE Aerospace and Electronic Systems Magazine, v15(1): pp39-45.

31. De Luca, A. and Blancquaert, T., 2005. *Battery Tests and Simulations for the Huygens Mission*. Seventh European Space Power Conference, May 9-13 2005, Stresa, Italy.

32. Hill, C.A., 1998. *Satellite Battery Technology - A Tutorial and Overview*. Proceedings of the 1998 IEEE Aerospace Conference, March 21-28 1998, Snowmass at Aspen, CO, United States.

33. Varta Microbattery Datasheet: PoLiFlex Lithium-Polymer Battery PLF 263441. http://www.varta-microbattery.com/en/mb_data/documents/data_sheets/DS66520.pdf

34. Varta Microbattery Datasheet: PoLiFlex Lithium-Polymer Battery PLF 523450. http://www.varta-microbattery.com/en/mb_data/documents/data_sheets/DS66281.pdf

35. Sanyo Datasheet: Cadnica Nickel-Cadmium Secondary Cell KR-7000F. http://batteries.sanyo-component.com/fileadmin/EDITORS/BATTERIES/industrial/datasheets/nicd/KR-7000F.pdf

36. ABSL Datasheet: Lithium-ion secondary cell 18650HC.

37. Fortescue, P., Stark, J. and Swinerd, G. (Editors), 2003. *Spacecraft Systems Engineering*. 3rd edition. Chichester: John Wiley and Sons. 678 pp.

38. Teofilo, V.L., Isaacson, M.J., Higgins, R.L. and Cuellar, E.A., 1999. *Advanced Lithium Ion Solid Polymer Electrolyte Battery Development*. IEEE Aerospace and Electronic Systems Magazine, v14(11): pp43-47.

39. Teofilo, V.L. and Nadell, J.N., 1998. *Aerospace Lithium Solid Polymer Batteries*. IEEE Aerospace and Electronic Systems Magazine, v13(5): pp33-36.

40. Grinter, K., 1997. *STS-87 Space Shuttle Mission*. NASA, http://science.ksc.nasa.gov/shuttle/missions/sts-87/mission-sts-87.html

41. Broussely, M., 1999. *Recent Developments on Lithium Ion Batteries at SAFT*. Journal of Power Sources, v81: pp140-143.

42. Ratnakumar, B.V., Smart, M.C., Whitcanack, L.D., Davies, E.D., Chin, K.B., Deligiannis, F. and Surampudi, S., 2004. *Behavior of Li-Ion Cells in High-Intensity Radiation Environments*. Journal of the Electrochemical Society, v151(4): ppA652-A659.

43. Choquette, Y., Lessard-Déziel, D., Houdayer, A., Khanna, S., Varga, L., Estan, D., Giray, M. and Brassard, G., 2002. *Proton and Electron Radiation Effects on Dry*

Lithium Metal Polymer Batteries. IEEE Nuclear and Space Radiation Effects Conference, 15-19 July 2002, Phoenix, AZ, United States.

44. Oman, H., 2002. *Technical Article: Mars Exploration Powered with Lithium Batteries*. Advanced Battery Technology, December 2002.

45. McKissock, B.I., Manzo, M.A., Miller, T.B., Reid, C.M., Bennett, W.R. and Gemeiner, R., 2005. *Preliminary Results of NASA Lithium-Ion Cell Verification Testing for Aerospace Applications*. Collection of Technical Papers - 3rd International Energy Conversion Engineering Conference, August 15-18 2005, San Francisco, CA, United States.

46. Garner, J.C., Morgan, C. and Forgione, Z., 2005. *Investigations on the Use of Lithium-Ion Batteries for Spacecraft at the U.S. Naval Research Laboratory*. Proceedings of the Seventh European Space Power Conference, May 9-13 2005, Stresa, Italy.

47. Wang, X., Sone, Y., Naito, H., Yamada, C., Segami, G. and Kibe, K., 2006. *Cycle-Life Testing of 100-Ah Class Lithium-Ion Battery in a Simulated Geosynchronous-Earth-Orbit Satellite Operation*. Journal of Power Sources, v160(1): pp602-608.

48. Sone, Y., Ooto, H., Eguro, T., Yoshida, T., Kubota, M., Yoshida, H., Yamamoto, M., Sakai, S., Ogawa, K., Takeda, Y., Uno, M., Hirose, K., Tajima, M. and Kawaguchi, J., 2007. *Charge and Discharge Performance of Over-Discharged Lithium-Ion Secondary Battery - Lessons Learned from the Operation of the Interplanetary Spacecraft HAYABUSA*. Electrochemistry, v75(12): pp950-957.

49. Dudley, G. and Verniolle, J., 1997. *Secondary Lithium Batteries for Spacecraft*. ESA Bulletin #90, Noordwijk, The Netherlands.

50. ESA/COMDEV, 2004. *Satellite Platform Elements (Li-Ion Battery)*. ESA Telecommunications Satellite Platform Line.

51. Martin, C.T., Kelly, C.O., Friend, H.D., Keen, C. and Wilson, S.L., 1999. *Lithium-Ion Battery Development at Eagle-Picher*. The Fourteenth Annual Battery Conference on Applications and Advances, 12-15 January 1999, Long Beach, CA, USA.

52. Bruce, G.C. and Marcoux, L., 2001. *Large Lithium Ion Batteries for Aerospace and Aircraft Applications*. IEEE Aerospace and Electronic Systems Magazine, v16(9): pp24-28.

53. Thwaite, C., Russel, N., Spurrett, R. and Bennetti, A., 2005. *The Comparison of Simulated Lithium-Ion Battery Performance with In-Orbit Telemetry*. Proceedings of the Seventh European Space Power Conference, May 9-13 2005, Stresa, Italy.

54. Hall, J.C., Lin, T., Brown, G., Biensan, P. and Bonhomme, F., 2006. *Decay Processes and Life Predictions for Lithium Ion Satellite Cells*. Collection of Technical Papers - 4th International Energy Conversion Engineering Conference, June 26-29 2006, San Diego, CA, United States.

55. Mattesco, P., Thakur, V. and Tricot, H., 2005. Overview and Preliminary In-Orbit Behaviour of the First Lithium-Ion Batteries used Onboard Eutelsat W3A GEO Telecommunications Satellite Mission. Proceedings of the Seventh European Space Power Conference, May 9-13 2005, Stresa, Italy.

56. Gerard, O. and Berger, G., 2006. *Eurostar E3000 In-Flight Experience*. Collection of Technical Papers - 24th AIAA International Communications Satellite Systems Conference, June 11-14 2006, San Diego, CA, United States.

57. Semerie, J.-P. and Dudley, G., 2005. *In Orbit Performance of the Smart-1 Li-Ion Battery*. Proceedings of the Seventh European Space Power Conference, May 9-13 2005, Stresa, Italy.

58. Macklin, W.J., Jarvis, C.R., Neat, R.J. and Thakur, V.V., 1997. *Development of a Lithium Ion Polymer Battery for Space Power Applications*. Power Sources, v65: pp280.

59. Rafaelle, R.P., Harris, J.D., Hehemann, D., Scheiman, D., Rybicki, G. and Hepp, A.F., 2000. *A Facile Route to Thin-Film Solid State Lithium Microelectronic Batteries*. Power Sources, v89: pp52-55.

60. Bates, J.B., Dudney, N.J., Neudecker, B., Ueda, A. and Evans, C.D., 2000. *Thin-Film Lithium and Lithium-Ion Batteries*. Solid State Ionics, v135: pp33-45.

61. Wang, X., Kato, M., Naito, H., Yamada, C., Segami, G., Kibe, K. and Kuwajima, S., 2006. *A Feasibility Study of Commercial Laminated Lithium-Ion Polymer Cells for Space Applications*. Journal of the Electrochemical Society, v153(1): ppA89-A95.

62. Buchmann, I., 2001. *Batteries in a Portable World: A Handbook on Rechargeable Batteries for Non-Engineers*. Cadex Electronics Inc, http://www.buchmann.ca/toc.asp (Accessed: 24/10/2008)

63. Schwingshackl, C.W., 2005. *Dynamic Behaviour of Inhomogeneous Multifunctional Structures*. PhD Thesis, University of Southampton, Southampton.

64. Schwingshackl, C.W., Aglietti, G.S. and Cunningham, P.R., 2007. *Experimental Determination of the Dynamic Behavior of a Multifunctional Power Structure*. AIAA Journal, v45(2): pp491-6.

65. Schwingshackl, C.W., Aglietti, G.S. and Cunningham, P.R., 2006. *Parameter Optimization of the Dynamic Behavior of Inhomogeneous Multifunctional Power Structures*. AIAA Journal, v44(10): pp2286-94.

66. Schwingshackl, C.W., Aglietti, G.S. and Cunningham, P.R., 2006. *The Dynamic Behaviour of Multifunctional Power Structures*. 57th International Astronautical Congress, IAC 2006, October 2-6 2006, Valencia, Spain.

67. Ashby, M.F., 2000. *Multi-Objective Optimization in Material Design and Selection*. Acta Materialia, v48(1): pp359-369.

68. Dornheim, M.A., 2003. *Small Drones Mature*. Aviation Week and Space Technology (New York), v159(11): pp63-64.Cowley, M., 2002.

69. Keennon, M., 2003. *First Fuel-Cell Flight*. Model Airplane News, September 2003.

70. Pickett, D.F., Jr., Hayden, J.W., Lucero, D. and Johnson, Z., 2000. *Comparison of Advanced Nickel-Cadmium Space Cell Technology with Other Technologies in Consideration for Low Earth Orbit, Geosynchronous Equatorial Orbit and Planetary Missions.* Proceedings of the Intersociety Energy Conversion Engineering Conference, 24-28 July 2000, Las Vegas, NV, United States.

71. Abu-Sharkh, S. and Doerffel, D., 2004. *Rapid Test and Non-Linear Model Characterisation of Solid-State Lithium-Ion Batteries*. Journal of Power Sources, v130(1-2): pp266-274.

72. Johnson, P.J., Donley, S.W. and Verrier, D.C., 1998. *Orbital Simulation Life Tests of Nickel Hydrogen Batteries with Additional Non-Eclipse Cycles*. Journal of Power Sources, v76(2): pp210-214.

73. Gao, L., Liu, S. and Dougal, R.A., 2002. *Dynamic Lithium-Ion Battery Model for System Simulation*. IEEE Transactions on Components and Packaging Technologies, v25(3): pp495-505.

74. Doerffel, D. and Abu-Sharkh, S., 2005. *Efficient Testing and Evaluation Methods for Faster Market Introduction of Large Lithium-Ion Batteries*. 5th International Advanced Automotive Battery and Ultracapacitor Conference (AABC-O5), 13-17 June 2005, Honolulu, Hawaii.

75. Dallas Semiconductor Datasheet: DS2740 High Precision Coulomb Counting Integrated Circuit.

76. Ilic, D., Birke, P., Holl, K., Wohrle, T., Haug, P. and Birke-Salam, F., 2004. *PoLiFlex™, the innovative lithium-polymer battery*. High Energy Density Electrochemical Power Sources Workshop, 17-20 September, Nice, France.

77. Schwingshackl, C.W., Aglietti, G.S. and Cunningham, P.R., 2006. *Determination of Honeycomb Material Properties: Existing Theories and an Alternative Dynamic Approach*. Journal of Aerospace Engineering, v19(3): pp177-183.

78. Aglietti, G.S., 2002. *A Lighter Enclosure for Electronics for Space Applications*. Proceedings of the Institution of Mechanical Engineers, Part G: Journal of Aerospace Engineering, v216(3): pp131-142.

79. Brander, T., Gantois, K., Katajisto, H. and Wallin, M., 2005. *CFRP Electronics Housing for a Satellite*. European Conference on Spacecraft Structures, Materials and Mechanical Testing, 10-12 May 2005, Noordwijk, The Netherlands.

80. Gaier, J.R., Hardebeck, W., Bunch, J.R.T., Davidson, M.L. and Beery, D.B., 1997. *Effect of Intercalation in Graphite Epoxy Composites on the Shielding of High Energy Radiation*. NASA Technical Memorandum #107413.

81. Gaier, J.R., Smith, J.M., Gahl, G.K., Stevens, E.C. and Gaier, E.M., 1998. *Fabrication and Resistivity of IBr Intercalated Vapor-Grown Carbon Fiber Composites*. NASA Technical Memorandum #208493.

82. SP Systems Datasheet: Low temperature epoxy prepreg system SE70T/SE70HS.

83. Amber Composites Datasheet: Low temperature curing resin film EF44.

84. Amber Composites Datasheet: Multipreg Prepreg E644.

85. *Structural Materials Handbook - Volume 1 (Polymer Composites).* 1994. Noordwijk, The Netherlands: European Space Agency.

86. Amber Composites Datasheet: Aluminium commercial honeycomb (AAC).

87. Megson, T.H.G., 1999. *Aircraft Structures for Engineering Students*. Butterworth-Heineman, Oxford, UK, p. 565.

88. Foster, J.A. and Aglietti, G.S., 2007. *Thermal Management Issues for Multifunctional Solar Arrays.* 1st CEAS European Air and Space Conference, 10-13 September 2007, Berlin, Germany.

89. Roberts, S.C. and Aglietti, G.S., 2007. *System-Level Mass Savings from a Multifunctional Powerstructure.* 1st CEAS European Air and Space Conference, 10-13 September 2007, Berlin, Germany.

Appendix I: Publications

Conference Papers

Roberts, S.C. and Aglietti, G.S., 2006. *Battery Performance Degradation under Vibration Loading*. 7th Conference on Dynamics and Control of Systems and Structures in Space (DCSSS07), 16-20 July 2006, Greenwich, London, UK.

Roberts, S.C. and Aglietti, G.S., 2006. *Multifunctional Power Structures for Spacecraft*. 57th International Astronautical Congress (IAC), 2nd-6th October 2006, Valencia, Spain.

Roberts, S.C. and Aglietti, G.S., 2007. *System-Level Mass Savings from a Multifunctional Powerstructure.* 1st CEAS European Air and Space Conference, 10-13 September 2007, Berlin, Germany.

Roberts, S.C. and Aglietti, G.S., 2008. *Design of a Multifunctional Spacecraft Structure using Plastic Lithium-Ion Batteries*. 12th AIAA/ISSMO Multidisciplinary Analysis and Optimization Conference, 10-12 September 2008, Victoria, BC, Canada.

Foster, J.A., Roberts, S.C. and Aglietti, G.S., 2008. *Multifunctional Power Structures and Related Thermal Issues*. ASME Conference on Smart Materials, Adaptive Structures and Intelligent Systems (SMASIS08), 28-30 October 2008, Ellicott City, MD, USA.

Journal Articles

Aglietti, G.S., Schwingshackl, C.W. and Roberts, S.C., 2007. *Multifunctional Structure Technologies for Satellite Applications*. The Shock and Vibration Digest, v39(5): pp381-391.

Roberts, S.C. and Aglietti, G.S., 2008. *Satellite Multi-Functional Power Structure: Feasibility and Mass Savings*. Proceedings of the Institution of Mechanical Engineers, Part G: Journal of Aerospace Engineering, v222(G1): pp41-51.

Appendix II: Composite Manufacturing

This section describes in detail the process of manufacturing the composite structures.

Facesheets

The preferred method to process prepreg composites is using a vacuum bag and autoclave. The high pressure of the autoclave results in minimal voiding and excellent resin consolidation. However, adequate results can be achieved using a vacuum bag and unpressurised oven if the resin flow is good [85]. By curing the facesheets with the highest temperature cycle, minimum resin viscosity will be achieved and the material will be well consolidated. Since the curing oven in the TSRL is subject to much less use than the autoclave, this method is preferable.

The manufacturing process may be summarised as follows:

- The prepreg is cut to size (using a Stanley knife or ceramic scissors) and laid up on an aluminium plate. The prepreg should be cut to a larger size than required as the edges will be rough and need trimming. The plate must be coated in FreeKote prior to use to ensure that the cured panel does not adhere to the plate. A gap must be left around the edge of the prepreg.

- The prepreg is covered in a layer of peel ply. Peel ply is a fabric that is permeable to resin but does not adhere to the cured material. The peel ply should cover the prepreg with a small margin.

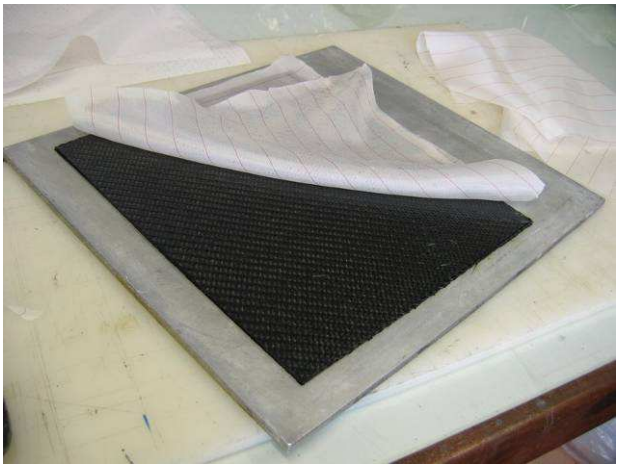

Appendix Figure A - Prepreg on aluminium plate, partially covered in peel ply

- The peel ply is followed by a layer of release film. This plastic film is pricked with small holes to control the flow of resin from the prepreg. Again, it should be slightly larger than the previous layer.

- Next is a layer of breather. This fleece-like material allows an air path to be maintained to the entire piece when a vacuum is applied. A "path" of breather should extend away from the prepreg to meet the breach valve (Appendix Figure C).

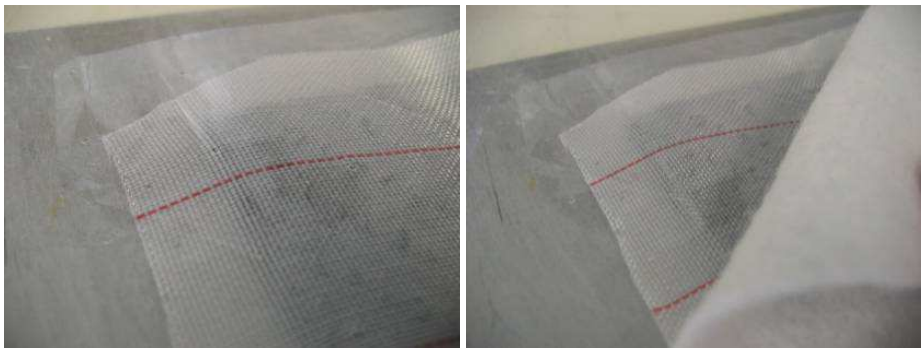

Appendix Figure B - Pricked release film (L) and breather (R)

- The entire assembly must then be vacuum bagged. Firstly, the breach valve is put in place, and then a border of adhesive tape ("tacky" tape) is placed around the

edge of the plate. A piece of vacuum bag is then cut to fit over the plate. The backing of the tape should be left in place until the vacuum bag is applied.

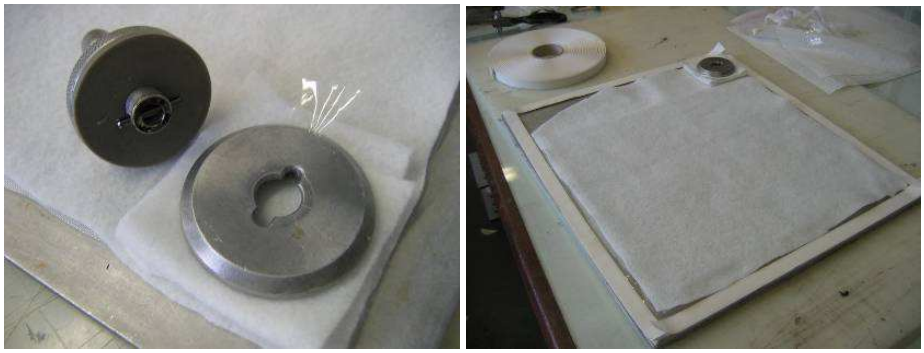

Appendix Figure C - Breach valve (L) and "tacky" tape (R)

- The vacuum bag is then placed over the entire plate. Care should be taken to ensure that the bag is taut, as any wrinkles may cause air leakage. It is likely that there will be some slack when the bag is stuck down, which must be filled with an "ear" of tape as shown in Appendix Figure D.

Appendix Figure D - Sealed bag (L) including "ear" (R)

- An incision is now made in the bagging to allow the breach valve to be connected.

The seal of the vacuum bag is tested by connecting it to the vacuum pump; the bag should be able to maintain a vacuum of 1 bar for a few minutes. If the seal is adequate, the pump is restarted and the oven programmed with the appropriate curing cycle:

* Increase temperature to the required value at a rate of 0.5°C/min.

* Dwell for the appropriate period, as shown in Appendix Table A.

Temperature, °C	Dwell period, hours
80	1.25
70	3.5
60	8
50	18

Appendix Table A – Curing cycles

* At the end of the curing cycle, the temperature is ramped down. The recommended rate is 2.5°C/min, although, in practice, simply switching off the oven and opening the door will produce an appropriate cooling rate at the low curing temperature of this material.

Appendix Figure E - The plate in the curing oven under vacuum

- When the cycle is complete, the pump is disconnected and the panel removed. The consumables should easily peel from the panel, and the panel should not adhere to the plate.

Sandwich Panel Assembly

The complete sandwich panel consisted of the following components: two CFRP facesheets, two pieces of resin adhesive film, eight aluminium inserts for fixing points, eight batteries plus wires and a sheet of aluminium honeycomb. The assembly of these components into a sandwich panel is described in this section.

- The first task was to cut the two facesheets to the correct size. This was done using a diamond edged circular saw. A purpose built composite cutting facility should be used to saw CFRP, as the dust produced from machining it is hazardous.

- Next, the honeycomb and adhesive were cut to fit the facesheets. Both can be cut with a knife or with normal scissors. A cardboard template was used to cut gaps in the honeycomb for the batteries and inserts.

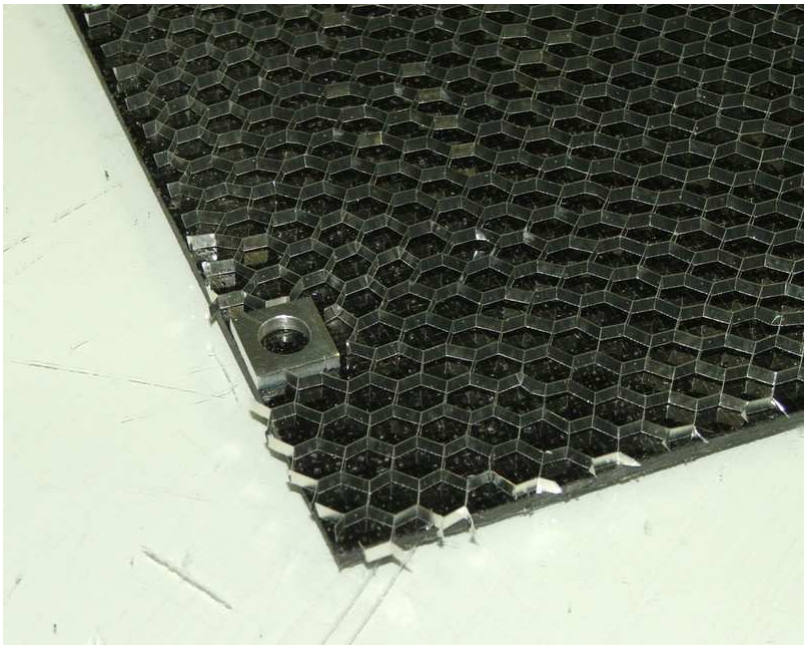

Appendix Figure F - Insert and honeycomb

- The panel was then assembled. One of the facesheets was placed with the peel ply (rough) side facing upwards, and a sheet of adhesive was placed on it (the rough side adheres better than the smooth side). The Batteries and inserts were then

placed onto the adhesive (located using the cardboard template). To prevent electrical shorts, any bare metal on the batteries should be covered in insulating tape.

- The honeycomb was then placed onto the adhesive. Thin strips of resin were used to bond the edges of the cells and inserts to the honeycomb. Then, the second layer of resin and the top facesheet were placed on top of the panel.

- Strips of peel ply were attached to the perimeter of the panel, and the entire panel was wrapped in breather. Finally, the panel was vacuum bagged and placed in the oven. The thermal profile used was the 50°C profile as indicated in Appendix Table A.

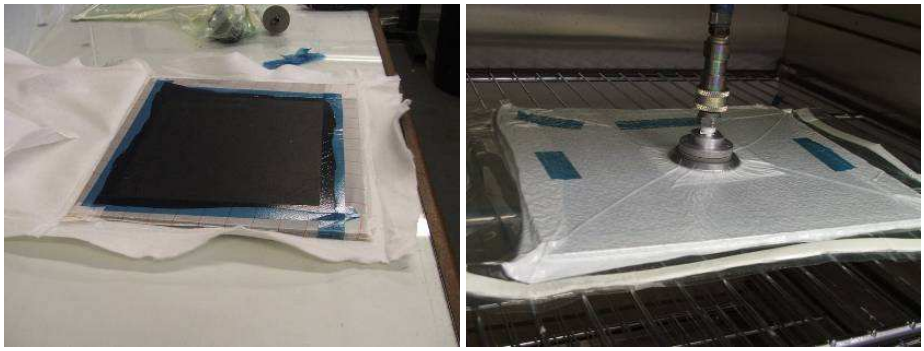

Appendix Figure G - Panel with peel play (L) and vacuum bagged in the oven (R)

- At the completion of the cycle, the bag is removed from the oven and the panel is removed. The completed panel is shown in Figure 5-6.

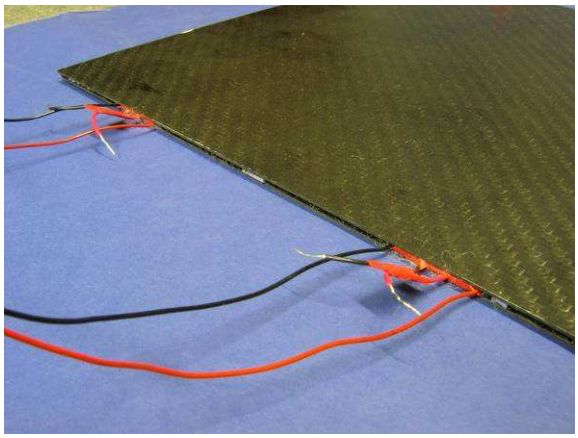

Appendix Figure H - The multifunctional panel